



TECHNISCHE
UNIVERSITÄT
DRESDEN



Molecular assemblies observed by atomic force microscopy

Dissertation

zur Erlangung des akademischen Grades
Doctor rerum naturalium
(Dr. rer. nat.)
vorgelegt von

David Alejandro Cisneros Armas

geboren am 12. August 1978 in Mexiko Stadt (Mexiko)

Gutachter:

Prof. Dr. Anthony Hyman

Prof. Dr. Daniel J. Müller

Prof. Dr. Jeremy H. Lakey

To my family:

Mireya Armas, Jorge Cisneros Armas and Jorge Cisneros González[†]

Summary

Atomic force microscopy (AFM) is a powerful technique that enables for observing and manipulating biological samples at different scales. While its resolution compares to other microscopy techniques, it has the additional advantage of observing specimens in an aqueous solution without fixation or staining. In the present work, AFM was used to characterize diverse biomolecular assemblies.

Firstly, we use time-lapse AFM to visualize collagen fibrils self-assembly. A solution of acid-solubilized collagen was injected into the AFM fluid cell and fibril formation was observed *in vitro*. Single fibrils continuously grew and fused with each other until the supporting surface was completely covered by a nanoscopically well-defined collagen matrix. Laterally, the fibrils grew in steps of ~4 nm suggesting a two-step mechanism. In a first step, collagen molecules associated together. In the second step, these molecules rearranged into a structure called a microfibril. High-resolution AFM topographs revealed substructural details of the D-band architecture. These substructures correlated well with those revealed from positively stained collagen fibers imaged by transmission electron microscopy.

Secondly, a covalent assembly approach to prepare membrane protein for AFM imaging that avoids crystallization was proposed. High-resolution AFM topographs can reveal structural details of single membrane proteins but, as a prerequisite, the proteins must be adsorbed to atomically flat mica and densely packed in a membrane to restrict their lateral mobility. Atomically flat gold, engineered proteins, and chemically modified lipids were combined to rapidly assemble immobile and fully oriented samples. The resulting AFM topographs of single membrane proteins were used to create averaged structures with a resolution approaching that of 2D crystals.

Finally, the contribution of specific amino acid residues to the stability of membrane proteins was studied. Two structurally similar proteins sharing only 30% sequence identity were compared. Single-molecule atomic force microscopy and spectroscopy was used to detect molecular interactions stabilizing halorhodopsin (HR) and bacteriorhodopsin (BR). Their unfolding pathways and polypeptide regions that established stable segments were compared. Both proteins unfolded exactly via the same intermediates. This

observation implies that these stabilizing regions result from comprehensive contacts of all amino acids within them and that different amino acid compositions can establish structurally indistinguishable energetic barriers. However, one additional unfolding barrier located in a short segment of helix E was detected for HR. This barrier correlated with a Pi-bulk interaction, which locally disrupts helix E and divides into two stable segments.

Table of contents

1.0. Introduction	7
1.1. Introduction to atomic force microscopy	7
1.1.1. Scanning probe microscopy	7
1.1.2. AFM: Basic Concept	7
1.2. Imaging mode of AFM	8
1.2.1. Contact mode AFM	9
1.2.2. Tapping mode AFM	9
1.2.3. Imaging mode in biology	9
1.2.4. Observing single proteins	10
1.2.5. Resolution constraints in AFM imaging	11
1.2.6. Tip-sample interactions affect resolution in AFM	12
1.3. Force mode of AFM	14
1.3.1. Force mode in biology	15
1.3.2. Single molecule force spectroscopy	15
1.3.3. Proteins as polymers	16
1.3.4. The freely jointed chain	17
1.3.5. Persistence length and the wormlike chain model	17
1.3.6. Physical interpretation of SMFS unfolding experiments	18
2. Collagen self-assembly observed by time-lapse AFM	21
2.1. Introduction	21
2.1.1. Fibrillar collagens and their assembly	21
2.1.2. Collagen structure observed by AFM	22
2.1.3. Biofunctionalization of surfaces	23
2.2. Materials and methods	24
2.2.1. Sample preparation	24
2.2.2. AFM	24
2.2.3. Image analysis	25
2.3. Results	25
2.3.1. Observing collagen self-assembly	25
2.3.2. Observing tips of collagen fibrils fusing	28
2.3.3. Lateral vs. longitudinal growth kinetics	28
2.3.4. Revealing growth steps of single collagen fibrils	30
2.3.5. Substructural details beyond the D-band periodicity	30
2.4. Discussion	31
2.4.1. Collagen assembly observed by tapping-mode AFM	31
2.4.2. Minimum unit of fibril growth	33
2.4.4. Fibril fusion	34
2.4.5. Collagen self-healing	36
2.4.6. Collagen matrices possess structural characteristics of tendon	37
2.4.7. Orientation of collagen molecules within the matrix	38
2.5. Conclusions	39
3.0. A new method to prepare membrane proteins for single molecule imaging	40
3.1. Introduction	40
3.1.1. Structure determination of membrane proteins	40
3.1.2. Structure and function of OmpF	41
3.2. Material and methods	42

3.2.1. OmpF-E183C production and purification.....	42
3.2.2. Preparation of gold supports.....	42
3.2.3. Assembly of OmpF-E183C on template-stripped gold.....	42
3.2.4. AFM and image analysis.....	42
3.3. Results.....	43
3.3.1. Assembly strategy.....	43
3.3.2. OmpF-E183C assembled on evaporated gold.....	43
3.3.3. Template-stripped gold yields a flat surface.....	45
3.3.4. Thiolipid assembly removes debris from TS-gold.....	45
3.3.5. OmpF-E183C assembles on TS-gold.....	47
3.3.6 High-resolution OmpF-E183C.....	50
3.4. Discussion.....	50
3.4.1. TS-Gold and thiolipids make a suitable support for AFM imaging.....	50
3.4.2. Imaging of membrane proteins embedded in thiolipids.....	51
3.4.3. High resolution imaging of OmpF-E183C.....	52
3.5. Conclusions.....	53
4.0. Collective interactions determine the stability of archaeal rhodopsins.....	54
4.1. Introduction.....	54
4.1.1. Structure and function of archaeal rhodopsins.....	54
4.1.2. Membrane protein folding in vivo.....	55
4.1.3. Unfolding single membrane proteins.....	56
4.1.4. Membrane proteins follow various unfolding pathways.....	56
4.1.5. Biological significance of mechanical membrane protein unfolding.....	56
4.2. Material and methods.....	57
4.2.1. Protein purification.....	57
4.2.2. AFM imaging.....	58
4.2.3. Single-molecule unfolding.....	58
4.2.4. Data analysis.....	59
4.3. Results.....	60
4.3.1. High-resolution imaging of halorhodopsin.....	60
4.3.2. Halorhodopsin unfolding.....	62
4.3.3. Unfolding pathways of HR.....	65
4.4. Discussion.....	66
4.4.1. Halorhodopsin imaging.....	66
4.4.2. Unfolding pathways of HR resemble those of BR.....	66
4.4.3. Collective interactions of aa establish stable structural segments.....	68
4.4.4. Unfolding of Helix E.....	70
4.4.5. Hierarchical unfolding within the “three stage” model.....	71
4.5. Conclusions.....	72
4.6. Future Perspectives.....	73
4.6.1. SRII unfolding resembles that of BR and HR.....	73
5.0 General Conclusions.....	74
5.1. Structural complexity of living organisms and self-organization.....	74
Abbreviations and symbols.....	77
Acknowledgments.....	80
List of publications.....	81
Bibliography.....	82

1.0. Introduction

1.1. Introduction to atomic force microscopy

AFM was invented twenty years ago (Binnig et al., 1986). The name derives from its ability to resolve single atoms and the use of a force sensor to create images. AFM is a surface technique and is broadly used in material sciences. True atomic resolution was achieved for the first time for calcite (Ohnesorge and Binnig, 1993). This was possible due to the flatness and rigidity of this sample. On the contrary, biological samples are structurally complex and labile. Still, AFM has remarkably developed into a tool with a broad range of biological applications. The major advantage of AFM is the ability to observe samples at high resolution in liquid without fixation or staining. Therefore, biological samples can be observed in their native environments.

1.1.1. Scanning probe microscopy

AFM belongs to a class of techniques referred to as scanning probe microcopies (SPMs), where a probe is raster-scanned over a surface and the interactions between the probe and the sample are measured at every point (Binnig and Rohrer, 1999). These techniques evolved from scanning tunneling microscopy (STM) (Binnig and Rohrer, 1983), which makes use of a tunneling current from the foremost atom of a mechanically positioned tip (probe) to image conductive surfaces. The invention of AFM arose from the idea of substituting the conducting probe with a sharp tip mounted on a spring (Binnig et al., 1986). The probe is just like the finger of a person reading a document in Braille.

1.1.2. AFM: Basic Concept

AFM is an electro-mechanical device: The spring (denominated cantilever) deflects while a tip mounted on it touches the sample's surface. The deflection of the cantilever is monitored by the deflection of a laser focused on it, which is reflected to a photodiode. The photodiode is at the same time divided mainly in two areas. When any topographical feature on the surface

deflects the cantilever beyond or below the setpoint, the laser beam on the photodiode is deflected toward one of the two areas (Fig. 1.1). During the scan, the interaction force between the sample and the tip is kept constant, which results in a topographic map created by an electronic feedback mechanism. This is called the imaging mode of AFM. In another application, which is called force mode, the spring can be used to measure the interaction force with the sample.

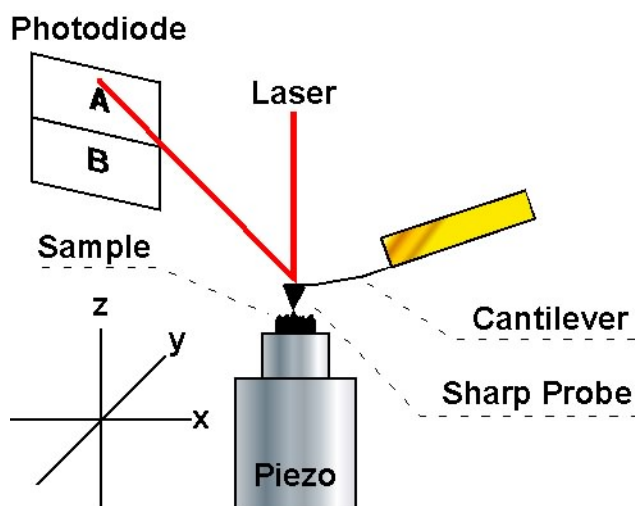


Figure 1.1. AFM setup. A sharp tip mounted on a flexible cantilever interacts with the surface. The cantilever deflects upon topographical features deviating a laser beam. The laser's deflection is detected by a photodiode. The signal is then transmitted to a feedback mechanism that maintains the interaction force between the tip and the sample constant.

1.2. Imaging mode of AFM

The forces involved in imaging can be steric, electrostatic, magnetic, van der Waals (all of electrostatic origin), or lateral (friction) forces (Binnig and Rohrer, 1999). These forces depend on the nature of the sample and the tip. The sample is mounted on a piezo-electrical element able to move in three coordinates (x , y , z). While the scan is made by the piezo (x - y movement), it extends or retracts vertically (z movement) in order to keep the interaction between the tip and the sample constant. In the original design of AFM the probe is in contact with the surface during the scan (contact mode AFM). This leads of course to lateral interaction between the sample and the tip. To minimize them, another type of AFM operation, called tapping mode (TM-AFM), was invented. TM-AFM makes use of an oscillating cantilever to probe the surface (Zhong et al., 1993).

1.2.1. Contact mode AFM

To visualize the topography of a sample with AFM in contact mode (CM-AFM) the interaction forces between the sample and the probe have to be kept constant at a user-defined deflection setpoint. When the tip encounters a topographical feature, the cantilever deflects beyond the setpoint. The feedback mechanism takes the deviation of the deflection of the cantilever from the setpoint and moves the piezo vertically to bring back the cantilever to the setpoint. The distance it moves is the height of the sample at that point.

1.2.2. Tapping mode AFM

In the tapping mode, the cantilever oscillates driven by an acoustic wave. That generates intermittent contact between the tip and the sample. Several parameters are sensitive to interaction between the tip and the sample. These are: amplitude, frequency, phase shift, and cantilever deflection. The amplitude, the resonance frequency and the phase shift of the oscillation link the dynamics of the vibrating tip to the tip-surface interactions. Any of them could be used as a feedback parameter to track the topography of the surface (Garcia and Perez, 2002). Amplitude-modulated TM-AFM is the technique that is most frequently used in biology. In this mode, the tip is excited at or near its resonance frequency and the root mean square (RMS) amplitude of the oscillation is detected by the photodiode. When the tip is in contact with the surface, the amplitude is reduced due to damping of the oscillation. The feedback loop maintains the amplitude of the oscillation constant at a user-defined setpoint by displacing the piezo vertically (Meyer et al., 2004). The topographic image is then generated, as in CM-AFM, by the movements of the piezo that keep the amplitude constant. Since the tip touches the surface only intermittently, the lateral forces are reduced (Fig. 1.2).

1.2.3. Imaging mode in biology

AFM is currently used to visualize samples at many different scales. For example, structures on the surface of cells are readily visualized with this technique. In one application, Poole *et al.* were able to observe structures on the surface of epithelial cells in different functional states depending on cholesterol depletion (Poole et al., 2004). In the case of melanoma cells,

surface structures were found, which correlated with surface receptors involved in migration, invasion and metastasis (Poole and Muller, 2005). At the intracellular level, molecular details are similarly examined. For example, Franz *et al.* dissected cells and analyzed the structure of actin bundles originated in cellular focal adhesions (Franz and Muller, 2005). Extracellular assemblies of proteins, like the one of collagen, were also examined by AFM, as it will be described in section 2.0. Observing single proteins at subnanometer resolution is also possible with AFM as discussed in the next section.

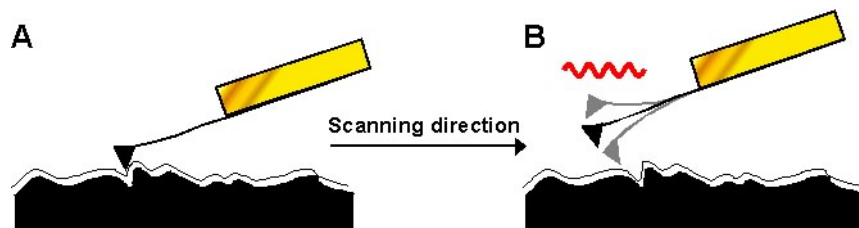


Figure 1.2 Contact mode vs. tapping mode. A) In CM-AFM the probe is kept in contact with the sample during the scan. Lateral forces between the tip and the sample cannot be avoided. B) In TM-AFM, a cantilever oscillating with certain amplitude is raster scanned, contacting the surface intermittently. Hence, lateral interactions are minimized.

1.2.4. Observing single proteins

Hoh *et al.* (Hoh *et al.*, 1993) performed the first observation of native single proteins with AFM. In their work, the extracellular surface of connexins was observed by dissecting with the AFM tip the upper hemi-channel layer of gap junctions. Hansma *et al.*, introduced the use of TM-AFM to study biological samples by imaging DNA in liquid (Hansma *et al.*, 1992). Since then, the list of proteins imaged with AFM has increased enormously (for a review see Muller *et al.*, 2002b). Furthermore, the capability of AFM to detect conformational changes at the single molecule level can be illustrated by the following examples. Firstly, Müller *et al.* (Muller *et al.*, 2002a) used the AFM tip to induce a conformational change in bacteriorhodopsin by scanning at higher forces (~ 300 pN). By doing this, flexible loops are pushed away by the tip, resolving then the underlying helical structures. In the second example, the single molecule Ca^{2+} - and pH- induced gating of connexin channels from gap junctions was observed by CM-AFM (Muller *et al.*, 2002a; Yu *et al.*, 2007). The use of chemically modified tips has led also to the development of recognition-AFM

(Stroh et al., 2004). In this technique, proteins are covalently attached to an AFM tip. This results in recognition of their ligands or receptors while performing TM-AFM imaging. The development of high speed AFMs (Ando et al., 2001) has lead to observe the power stroke of single myosin molecules (Ando et al., 2003). In summary, the field has achieved the possibility of observing many aspects of biological phenomena. With commercial equipments the resolution has been pushed to sub-nanometer resolution in contact (Muller et al., 1999b) or in tapping mode (Moller et al., 1999). To date most of the results are produced in a few specialized labs in the world, mainly because the technique requires expertise to avoid deceiving artifacts.

1.2.5. Resolution constraints in AFM imaging

In AFM, many factors affect resolution like the geometry and sharpness of the tip. The radius of curvature of the tip is an important parameter, especially because the acquired image is a convolution between the probing tip shape and the sample features. Topographic features which have a larger aspect ratio compared to the tip are not resolved (Fig 1.3). Therefore, a blunt tip will broaden topographic features and reduce the apparent corrugation (Meyer et al., 2004). Commercially available tips have a radius of $\sim 15\text{-}20$ nm. Other factors affecting resolution have to do with sampling effects and interactions between the tip and the sample. As the height of the topograph is recorded as an image, its measurement is constrained to the pixel size and bit size of the image (Heymann et al., 2002). Sample preparation represents another obstacle in resolving accurately biological samples. The highest resolution has been achieved with densely packed samples like membrane protein 2D crystals (Muller et al., 2002b). The advantage of these samples is that the packing reduces lateral displacements of the proteins by the AFM stylus.

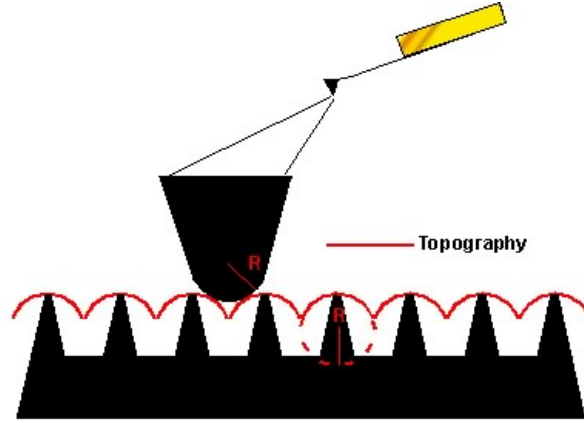


Figure 1.3. Tip convolution. The radius of the tip, which convolutes with the sample, reduces the observed corrugation on the topography. So basically, the features on the sample image the tip.

1.2.6. Tip-sample interactions affect resolution in AFM

Biological molecules exhibit a net surface charge. The magnitude of the charge depends on the pH of the buffer solution. The net charge is compensated by counterions from the bulk solution. The Debye length λ_D characterizes the exponential decrease of the potential resulting from screening the surface charges. It depends only on a constant that it's determined by the valency (c) and concentration of the electrolyte (e_c); these parameters are related as follows: $\lambda_D = c / \sqrt{e_c}$. The interaction (described as force) between surfaces can be modeled with the DLVO theory (Derjaguin, Landau, Verwey, Overbeek), in this case being the surface of the tip and the sample (Muller and Engel, 1997). In these models, the interplay of electrostatic forces (F_{el}) and van der Waals (F_{vdW}) are taken into account as follows:

$$F_{DLVO} = F_{el}(z) + F_{vdW}(z) = \frac{4\pi\sigma_s\sigma_t R\lambda_D}{\varepsilon_e\varepsilon_0} \exp\left(-\frac{z}{\lambda_D}\right) - \frac{H_a R}{6z^2} \quad \text{Eq. 1.1,}$$

where σ_s and σ_t are the surface charge densities of the sample and the tip respectively, ε_0 is the permittivity of the free space, ε_e is the dielectric constant, H_a is the Hamaker constant, R is the tip radius and z is the distance between them. It was noted first, that the height of molecules depended on the electrolyte concentration in the buffer solution in which they were imaged (Muller and Engel, 1997). In particular the height of purple membrane patches was overestimated at low electrolyte concentration. As calculated with eq. 1.1

by Müller *et al.*, (Muller and Engel, 1997) at sufficiently high electrolyte concentrations and a separation smaller than ~ 2 nm the van der Waals attraction becomes predominant. When the height of purple membranes was measured at different applied forces, it was shown that there was only dependence at low salt concentrations, when there is electrostatic repulsion between surfaces. All these effects come from the different dependence on the distance of the two contributing forces (exponential vs. quadratic, Eq 1.1). In summary, height-measuring artifacts can appear when the sample imaged in liquid presents a repulsive interaction with the tip (Muller and Engel, 1997).

Topographical features on the surface of membrane proteins have been imaged at sub-nanometer resolution (Muller *et al.*, 2002b). Because of tip convolution, it would be impossible to obtain high-resolution topographs with commercial tips that have a radius ranging from 10-20 nm. Therefore, it has been hypothesized that a local smaller tip actually contours the protein surface. This small tip is called the “local” tip mounted on the larger “global” tip. In this case a sample interacts in a similar way as described in eq 1.1 (Muller *et al.*, 1999a) with both the global and the local tip. Calculations made for a local tip with a radius of ~ 2 nm show that at low electrolyte concentrations, the electrostatic repulsion, $F_{el}(z)$, of the global tip would not let the local tip to enter into contact with the sample. Forces larger than 2 nN would be necessary, which could disrupt the sample. Conversely, at very high salt concentrations, when the electrostatic repulsion is overcome by screening ions, the global tip would be pulled onto the sample deforming the sample. In conclusion, stable imaging on biomolecules requires the global tip to be supported by electrostatic repulsion but in such a way that permits the local tip to interact with the sample through van der Waals (F_{vdW}) interactions. This has been called electrostatically balanced AFM imaging (Muller *et al.*, 1999a).

1.3. Force mode of AFM

The cantilever described in the previous sections can be used to measure forces at the pN scale. In this case the cantilever is treated as a spring following Hooke's law: $F = -k\Delta z_{cant}$, where F is the force, k is the spring constant of the cantilever and Δz_{cant} is the deflection of the cantilever. The setup is shown in figure 1.4 with an example of a force vs. distance trace. In extension-retraction cycles of the piezo, the tip is brought into contact to the sample. At the beginning of the cycle, the tip is far from the piezo (Fig 1.4A). As the tip reaches the sample it jumps into contact, showing a positive force called “snap-in” (blue peak Fig 1.4B). As the piezo keeps extending the cantilever bends in the other direction and now there is a force exerted by the cantilever (Fig 1.4C). At that point the retraction cycle begins. If there is an interaction force between the cantilever and the sample, then the cantilever will resist detachment from the surface, showing a positive force called adhesion force (Fig 1.4D). At the end of the cycle the tip finally detaches from the surface and the force equals zero again (fig 1.4E).

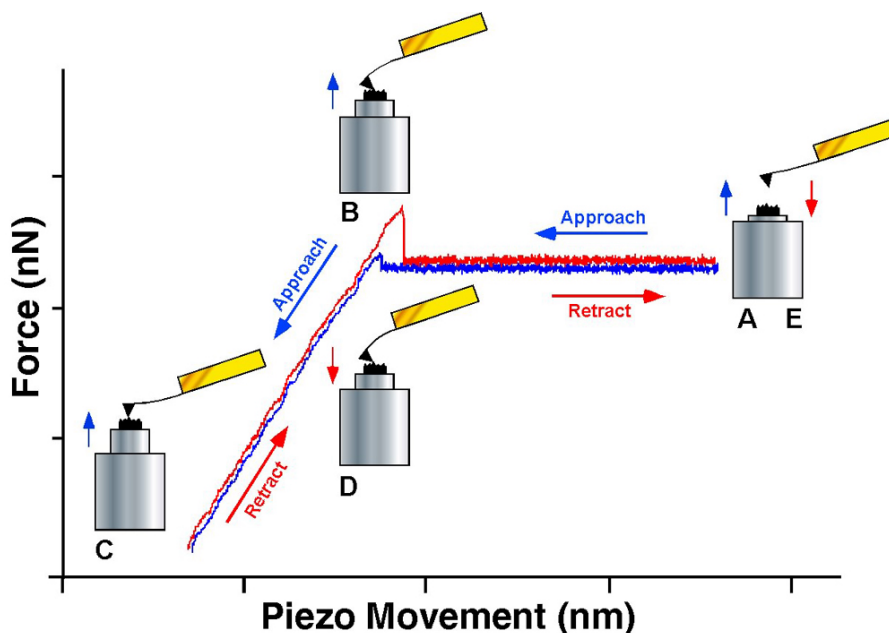


Figure 1.4. Force mode of AFM. In extension cycles (A to D), the piezo brings the sample in contact with the tip. Interaction forces are measured as peaks detected in the force versus distance trace (See text for details).

1.3.1. Force mode in biology

Force is a parameter controlling many biological processes, from covalent bonds (Grandbois et al., 1999) to receptor-ligand interactions (Hinterdorfer and Dufrene, 2006). In the case of single proteins in solution the relevant scale is the pN (Evans, 2001). Molecules immersed in liquid are subjected to thermal collisions equal to $\sim 1 k_b T$, where k_b is the Boltzmann constant. This correspond in force to ~ 4 pN (Evans, 2001), which is the just the range that is appreciable by AFM.

1.3.2. Single molecule force spectroscopy

In single molecule force spectroscopy (SMFS) a single molecule is clamped to the cantilever's tip and pulled from the surface. For example, it can be used to measure the force needed to rupture a ligand-receptor bond (Hinterdorfer and Dufrene, 2006). The rupturing of a bond formed between the molecule clamped on the cantilever and another molecule on the surface will be observed as a positive peak in the force vs. distance trace (Fig. 1.4). SMFS can also be used to study the folding and unfolding of proteins (Carrion-Vazquez et al., 2000). The first experiments done by Rief *et al.*, were performed with the giant muscle protein titin (Rief et al., 1997). Titin is a protein that consists of immunoglobulin (Ig) repeats and type III fibronectin repeats. When the cantilever was brought to the surface in an extension-retraction cycle of the piezo, it bound to a single molecule and pulled it away from the surface. When each one of these domains unfolded, a peak appeared in the force trace. The overall appearance of the force trace has a saw-tooth pattern (Fig 1.5). The force is transmitted from the cantilever to each domain through the rest of the protein, or through previously unfolded domains. The increase in force of each of these peaks represents only the stretching of the unfolded polypeptide. Domains finally unfold at the end of the peak, represented by the sudden drop in force. The difference between the maximum of the peak and the baseline represent the unfolding force, which is the force at which a single domain unfolds. In this sense, the extension of a previously unfolded domains serves as the linker that exerts a non-linear force ramp over each of the folded domains.

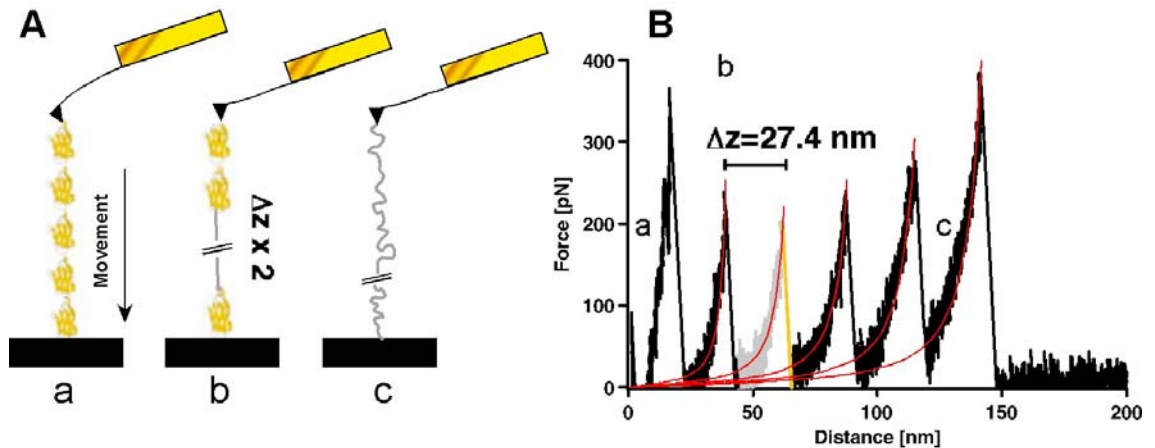


Figure 1.5. Unfolding of titin. A) Scheme of unfolding experiment in titin Ig27₅ recombinant polyprotein. A molecule consisting of five Ig27 molecules is clamped to the tip and the surface (a), as the piezo moves downward, a force is exerted on the protein. At the end of the retraction cycle, all the domains were unfolded (c). B) Force versus distance trace of single molecule titin unfolding showing a saw-toothed pattern. Unfolded domains stretch (e.g. in the gray part of curve), and the cantilever is bent. When the force exceeds the stability of one domain, it unfolds relaxing the cantilever and bringing the force back to zero (yellow part of the curve). Force peaks are fitted to the worm like chain (WLC) model (red curves), from which the length of the stretched polymer can be obtained. The difference in contour length between two segments defines Δz . The length (Δz) equals the length of the unfolded polymer. Six peaks are observed, the first five are the unfolding of the Ig27 repeats, and the last one is just the stretching of all 5 unfolded domains where the force represents detachment from the surface.

1.3.3. Proteins as polymers

Polymers in solution are subjected to thermal forces. These forces induce fluctuations in length and in shape. Shape fluctuations are important because they determine how these polymers maintain a certain structure over time. If a polymer is very flexible, thermal forces lead to such large shape fluctuations that it is said that the polymer is unstructured (Howard, 2001). Under the influence of force, unfolded proteins can be treated as entropic springs. Entropic springs resist acquiring a straight conformation due to its tendency to return to its more disordered configuration. The force they exert to keep themselves as a random coil is called the restoring force. Very large displacements of the polymer would deform bonds due to their stretching in the direction of the applied force. At that point the polymer exerts an enthalpic restoring force. We consider here only the entropic contribution.

During a SMFS experiment a protein remains tethered to the surface and to the cantilever. During this time force is applied and unfolded domains stretch

along one direction. The restoring force of the entropic spring is then transmitted to the folded domains as explained above.

1.3.4. The freely jointed chain

The freely jointed chain (FJC) models the stretching of a polymer with a contour length L , formed by n subunits of length b (Fig 1.6A). The extension z of the polymer held by the two ends can be expressed as a function of the pulling force (Eq. 1.2).

$$z(F) = nb \left[\coth \left(\frac{Fb}{k_b T} \right) - \frac{k_b T}{Fb} \right] = nb \mathbf{L} \left(\frac{Fb}{k_b T} \right), \quad \text{Eq. 1.2,}$$

where \mathbf{L} is the langevin function $\mathbf{L}(u) = \coth(u) - 1/u$ and the product nb defines the contour length (L , not to be confused with \mathbf{L}). The langevin function increases from zero to one as u increases. Consequently, if $u = Fb/k_b T$, the FJC average extension increases from zero to nb , the length of the fully extended polymer. The freely joint chain describes well the stretching behavior of polysaccharides (Janshoff et al., 2000).

1.3.5. Persistence length and the wormlike chain model

Freely jointed chains with many segments behave qualitatively as slender rods. That is, rods whose lengths are greater than their diameters (Howard, 2001). The most important parameter, describing slender rods resistance to thermal forces is the persistence length (l_p). The intuitive meaning of l_p is the length of the rod over which bending produced by thermal forces becomes appreciable. Very rigid rods, like microtubules, have persistence lengths considerably larger than their lengths (Howard, 2001). Flexible polymers, like unfolded proteins, have persistence lengths many times smaller than their contour lengths. Such a rod is called a wormlike chain (Fig 1.6B). The relationship of the entropic restoring force to the extension is as follows:

$$F(z) = \frac{k_b T}{l_p} \left[\frac{1}{4} \left(1 - \frac{z}{L} \right)^{-2} + \frac{z}{L} - \frac{1}{4} \right] \quad \text{Eq. 1.3}$$

The chain direction is preserved on the length scale of the persistence length, and below the persistence length the polymer can be considered to be linear (Janshoff et al., 2000). The WLC is suitable to model the stretching of DNA (Bustamante et al., 1994) and of unfolded polypeptides (Rief et al., 1997). In a SMFS as the one shown in figure 1.5, the increase in distance of Δz is related to the length L of the unfolded polypeptide. Treated as a wormlike chain, a persistence length of 0.4 nm describes well the behavior of the force distance curve. The same value of persistence length was used to fit the stretching of unfolded membrane proteins (Oesterhelt et al., 2000). Under this assumption the length of the unfolded polypeptide L can be calculated (Figure 1.5, red curves). One of the main advantages of the FJC and WLC models is that in spite that fluctuations in the polymer occur in three dimensions, its extension behavior is described in a single distance coordinate (z) (Fig. 1.6).

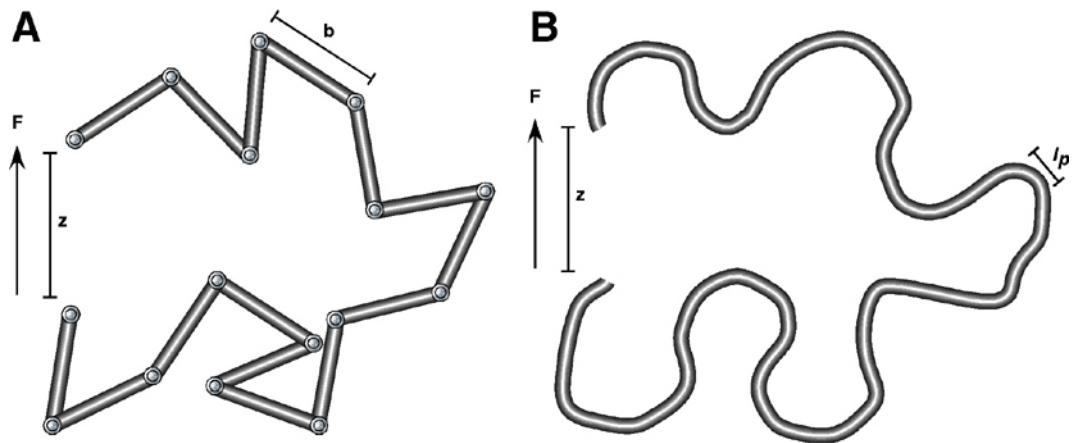


Figure 1.6. Comparison of FJC and WLC models. Two polymers with similar overall shape as modeled by the FJC and WLC. When extended, a restoring force F is measured along the pulling direction z . A) The length of the subunit b characterizes a FJC; its behavior is defined by the langevin function (Eq 1.2). B) The persistence length defines the behavior of a WLC as describe by equation 1.3.

1.3.6. Physical interpretation of SMFS unfolding experiments

As we saw in the previous section, each peak in the force vs. distance trace represents the cooperative unfolding of a protein domain. The unfolding process can be viewed as a two-state transition of a molecule going from the native (N) to the unfolded state (U) crossing a single energetic barrier (Fig. 1.7). In this 1-D abstraction, the coordinate z is assumed to map the transition pathway over a barrier defined by the activation energy (E_{ts}) relative to the

deepest minimum. Applying a persistent-external force contributes a mechanical unfolding potential that deforms the chemical energy landscape (Evans and Williams, 2002; Rief et al., 1998). The reaction coordinate under the experimental conditions is projected to the pulling direction z . Unfolding occurs when there is a switch in the location of one of the energy minima (compare dashed vs. pointed energy landscape in Fig. 1.7).

Force reduces a barrier along the reaction coordinate in proportion to a thermally-averaged projection (z_b) related to the position of the transition state as follows: $z_b = \langle z_{ts} \cos \theta_b \rangle$. Here, z_{ts} represents the distance between the native state and the transition state and θ is an angle that compensates for instantaneous deviations from the pulling direction (Evans and Williams, 2002). Then the activation energy (E_{ts}) is influenced (lowered) linearly by the applied force as (Evans and Williams, 2002; Rief et al., 1998): $E_{ts}(f) = E_{ts} - f \cdot z_b$. Further, in such a two state transition the off rate (k_o) of the reaction is determined by $k_o = \alpha \cdot \exp(-E_{ts}/k_b T)$ (Rief et al., 1998), where α is the pre-exponential factor related by Kramer's theory to the reciprocal of the diffusion time (see Evans and Williams, 2002). Therefore, the off rate of the unfolding reaction, is affected by an external force as follows (Rief et al., 1998):

$$k_U = k_o \exp[-(E_{ts} - fz_b)/k_b T] \quad \text{Eq. 1.4}$$

The calculations above determine the characteristic force scale (f^*) for the reaction, which is determined by thermal collisions: $f^* = k_b T/z_b$. We said $k_b T$ is in the order of ~ 4 pN, and z_b has been found to be in the order of 0.1-1 nm (Evans and Williams, 2002; Janovjak et al., 2004; Rief et al., 1998). Therefore, exerting an external force a few times over f^* on a protein will cause it to unfold a hundred or thousands times faster than it spontaneously would (Evans and Williams, 2002). In an SMFS experiment, as the one presented in figure 1.5, a force gradient is exerted on the protein until it reaches the necessary force to overcome the energy barrier.

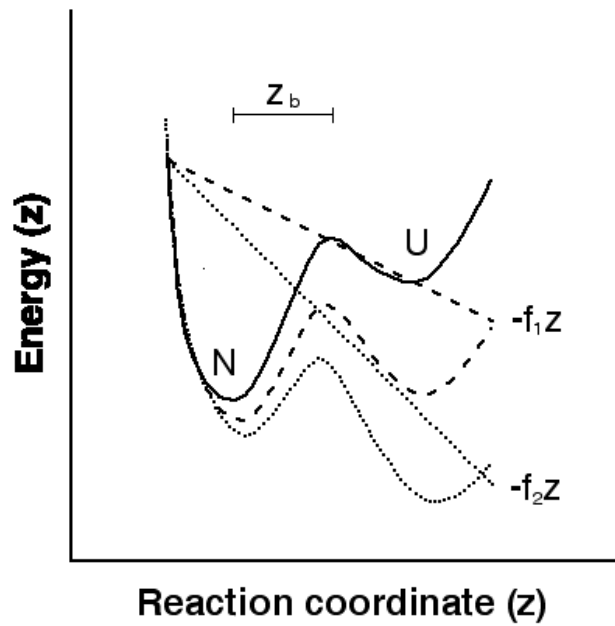


Figure 1.7. Conceptual energy landscape for a two-state transition. Coupled to the projected reaction coordinate z , a persistent-external force f adds a mechanical potential $-fz$ that tilts the energy landscape (continuous line) and lowers the energy barrier towards unfolding. Two different forces are shown to exemplify, f_1 (dashed line) and f_2 (pointed line) where f_2 is larger and switches the energy landscape to unfolding. z_b represents the distance from the folded state to the transition state along the projected reaction coordinate.

In summary force modifies an energy landscape in a way similar as other denaturants like urea, guanidinium hydrochloride and temperature induce unfolding of proteins. The equivalent action of force and denaturants was experimentally proved at least for titin (Carrion-Vazquez et al., 1999). It was shown that the unfolding rates and position of the transition state are similar when obtained from force or denaturant unfolding experiments (Carrion-Vazquez et al., 1999). The advantages of single molecule experiments are that no secondary reactions are coupled and that single molecules can be observed instead of ensembles of molecules. Also, one can observe low frequency reaction intermediates that otherwise would be lost in the bulk. Single molecules often behave differently among each other and that is the beauty of SMFS.

2. Collagen self-assembly observed by time-lapse AFM

2.1. Introduction

Cells in multicellular organisms interact with an extracellular matrix composed of fibrous proteins, linker proteins, and complex polysaccharides. In human connective tissues, collagen fibers comprise the major component. Besides shaping and organizing the extracellular matrix (ECM), collagen provides a scaffold, which is then functionalized by other proteins (Hohenester and Engel, 2002). Connective tissue morphogenesis and homeostasis, as well as its rearrangement during wound repair depend on interactions between cells and the ECM (Grinnell, 2003). Collagens receive considerable interest because of their involvement in various human diseases (Kadler, 1993; Kunicki, 2002; Myllyharju and Kivirikko, 2001; Myllyharju and Kivirikko, 2004; Ortiz-Urda et al., 2005; Prockop, 1998; Prockop, 1999; Yuspa and Epstein, 2005).

2.1.1. Fibrillar collagens and their assembly

Collagen fibrils are rod-shaped molecules of ~ 300 nm in length. From these, collagen type I is the most studied. Structurally, collagen type I consists of three polypeptides that wind around one another into a triple helix (Fig. 1, top). Each of these polypeptides comprises a repeating Gly-X-Y triplet, in which X and Y are usually represented by proline and hydroxyproline. The dimensions of the rod are $\sim 1.5 \times 300 \text{ nm}^2$ (Orgel et al., 2001) and follow a hierarchical assembly into a fibrillar form. Collagen fibrils assemble in many tissues in a quasi-crystalline structure, which was recently determined by X-ray diffraction (Orgel et al., 2006). In this structure five collagen molecules form the unit cell, called a microfibril. The dimensions of the unit cell are $\sim 3.9 \times \sim 2.7 \times \sim 67 \text{ nm}^3$. Contrary to the early vision of collagen assembly (Petruska and Hodge, 1964), these microfibrils assemble non-linearly by interdigitation (Fig. 2.1). When inspected by electron microscopy (Chapman et al., 1990) or AFM (Cisneros et al., 2006; Raspanti et al., 1997), the quasi-crystalline structure of collagen fibrils present a repeating pattern of ~ 67 nm (D-band periodicity) perpendicular to their axis (Fig. 2.1).

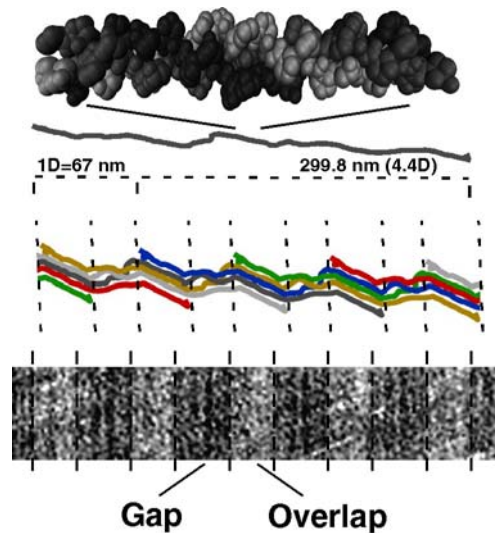


Figure 2.1. Model of the hierarchical assembly of collagen type I molecules into fibrils. Top, in the axial direction, collagen molecule assembles from three collagen monomers forming a 299.8 nm long triple helix. Middle, five collagen molecules (each one shown in different color) stagger and interdigitate laterally shaping one microfibril, which has a cross section of $3.9 \times 2.7 \text{ nm}^2$. Oriented microfibrils assemble into collagen fibrils producing the D-band periodicity of $\approx 65\text{-}67 \text{ nm}$ such as observed by transmission electron microscopy and AFM. The bottom panel represents a high-resolution AFM topograph of a self-assembled collagen fibril.

Collagen is synthesized in the ER and secreted to the extracellular space as an immature form. Outside the cell, proteolytic enzymes cleave both N- and C- terminus, which initiates fibrillogenesis. Afterwards covalent crosslinking occurs through the action of the enzyme lysyl oxidase. Covalent bonds between the triple helices give mature collagen great tensile strength. Current models describe the formation of collagen fibrils as a self-assembly process, which results in the formation of corrugated sheets that stabilize native fibrils in tissues (Hulmes, 2002, Orgel, 2001 #8; Kadler et al., 1996).

2.1.2. Collagen structure observed by AFM

AFM has been used to study collagen assembly and network formation in different types of biological systems (Bigi et al., 1997; Gayatri et al., 2001; Jurvelin et al., 1996; Marshall et al., 2001; Meller et al., 1997; Raspanti et al., 2001; Thalhammer et al., 2001), dynamic processes associated with enzymatic collagen degradation (Annunen et al., 1999; Fantner et al., 2004; Sun et al., 2000), and the interaction of collagens with other molecules such as proteoglycans (Chen and Hansma, 2000; Fantner et al., 2004; Raspanti et al.,

1997; Raspanti et al., 2005) or the discoidin receptor (Agarwal et al., 2002). Several works have used AFM to image the structure of collagen polymerized *in vitro* (Chernoff and Chernoff, 1992), in rat tendon fiber (Gutsmann et al., 2003; Raspanti et al., 2002; Revenko et al., 1994), in dentin collagen fibrils (Habelitz et al., 2002; Ho et al., 2005; Yang et al., 2005), in bone (Hassenkam et al., 2004), and in bovine humeral particular cartilage (Jurvelin et al., 1996). Recently, a method to align collagen fibril on mica was developed (Jiang et al., 2004a). The effect of pH and electrolytes on the self-assembly of collagen and the exposure of the typical D-periodicity was then characterized (Jiang et al., 2004a). The AFM stylus could also be applied as a nano tweezer to remodel the collagen matrix on the nanometer scale. Structural details ranging from few nm to a few hundred μm in size could be written into the collagen matrix (Jiang et al., 2004b). These collagen matrices could be used to direct attachment, orientation and motility of fibroblasts (Poole et al., 2005).

2.1.3. Biofunctionalization of surfaces

Surface functionalization and patterning represents a major concern in biotechnology. Patterned surfaces can be used to direct cellular attachment, orientation and migration (Cavalcanti-Adam et al., 2006; Gallant et al., 2005). Various techniques have been developed to create nanopatterned materials. Some of them, e.g. polymer demixing or self-assembling compounds, take advantage their intrinsic properties, like charge or solubility (Norman and Desai, 2006). Other approaches induce topographical or chemical patterns by processes, like electron beam lithography or colloidal lithography (Norman and Desai, 2006). The size of the patterned features has been recently reduced to a few tens of nanometers by dip-pen nanolithography (Demers et al., 2002; Lee et al., 2002), which increases its applicability for even ambitious proteomic approaches. A fundamental part of biofunctionalization is the incorporation of a biocompatible entity. One approach comprises the introduction of small sequences into synthetic materials that mimic binding sites (Brandl et al., 2007). Another approach would be to use the self-assembly properties of biomolecules to create compatible matrices.

In this chapter, we present the direct observation of the self-assembly of collagen type I molecules into anisotropic higher ordered structures by time-

lapse AFM. Collagen molecules assembled laterally and fused into broad sheet-like fibrillar structures. We propose a model of how collagen molecules incorporate into other fibers in a two-step process. High-resolution AFM topographs showed detailed substructures of the self-assembled matrix. When compared with transmission electron microscopy (TEM) data, the images suggested that the observed collagen fibrils exhibited the same structural features, which were described in assembled *in vivo* collagen fibers from tendon (Chapman et al., 1990).

2.2. Materials and methods

2.2.1. Sample preparation

Part of this work was done in collaboration with Msc. Carlos Hung. Collagen type I was purchased from Invitrogen (Palo Alto, California, USA). A single batch of collagen molecules was used through out the experiments. The final composition of the sample is 97% collagen type I, and 3% collagen type III according to the producer. As a supporting surface, a mica disc of 6.5 mm in diameter was used. After being freshly cleaved, a drop of buffer solution ($\approx 30 \mu\text{l}$) was placed on to the mica surface, and 90 μl on the AFM fluid cell. The sample and buffer solution were placed into an AFM equipped with a fluid cell. After thermal relaxation, a small amount of buffer solution containing collagen at different concentrations was injected into the fluid cell while time-lapse AFM imaging was continuously performed. Collagen molecules aligned on the mica surface following most likely the crystalline mica lattice, as it has been proposed for α -synuclein fibrils (Heise et al., 2005).

2.2.2. AFM

The AFM (MultiMode, di-Veeco, CA) was operated in buffer solution using a fluid cell at 25 °C. The piezoelectric scanner had a scan range of $\sim 100 \times 100 \mu\text{m}^2$. Oxide sharpened Si_3N_4 cantilevers with a nominal force constant of 0.08 N/m (OMCL TR400PS) were used (Olympus Ltd, Tokyo). Imaging was performed in tapping mode (TM-AFM) with a drive frequency close to the resonance frequency of the cantilevers (8 – 9.5 kHz). The drive amplitude of the cantilever was set to a RMS value of 18 - 30 nm.

2.2.3. Image analysis

Image analysis and processing was carried out using the software Image SXM (Barret, 2004) and ImageJ (Abramoff et al., 2004). A mask was created with the threshold option of Image J to measure the area ratio of collagen to mica in $1\ \mu\text{m}^2$. Lateral and longitudinal growth was characterized by measuring the fibril width and length at different times on surface areas of $15 \times 15\ \mu\text{m}^2$, which were randomly selected on the supporting surface. In the case of the longitudinal growth measurement, the position of the fibril end was measured and the growth was derived from the distance to the fibril end at the following frame. The lateral fibril growth (measured in different areas) was derived from the increasing fibril width, which was determined using the “find edge” function of Image J from contour masks of the fibrils. Thermal drift of the topographs was compensated manually to allow determining fibril widths at the same reference points by measuring the movement of any imperfection on the mica.

Growth steps of individual collagen fibrils could be observed after increasing the temporal resolution by scanning only a few lines over the fibril with 4096 pixels. The width increase was determined from the full-width at half-maximum (FWHM) of the height profile along a cross section of 20 nm. Fibrils were considered exhibiting the same width between two different frames if their difference in width was less than 2 pixels.

To enhance ultrastructural details of collagen, 13 D-periods of a selected topographical area were averaged line by line transversally to the D-band. The averaged height profile was cross-correlated with the EM density profile (Fig. 8) using the correlation function of Igor Pro (Wavemetrics, Inc.).

2.3. Results

2.3.1. Observing collagen self-assembly

Jiang *et al.* (Jiang et al., 2004a) established conditions (pH and electrolyte) under which collagen molecules adsorb and align on a mica support. The collagen molecules assembled into fibrils that formed a 2D ultrathin ($\approx 3\ \text{nm}$) matrix. Collagen fibrils in these matrices established their characteristic D-band periodicity ($\approx 67\ \text{nm}$) exclusively in presence of K^+ ions. At a pH close to the *pI* of collagen (9.3) (Hattori et al., 1999) individual fibrils could

be clearly resolved (Jiang et al., 2004a). To observe the self-assembly of individual molecules into a fibrillar network we performed our experiments in an aqueous solution buffered at pH 9.2 in the presence of K^+ ions.

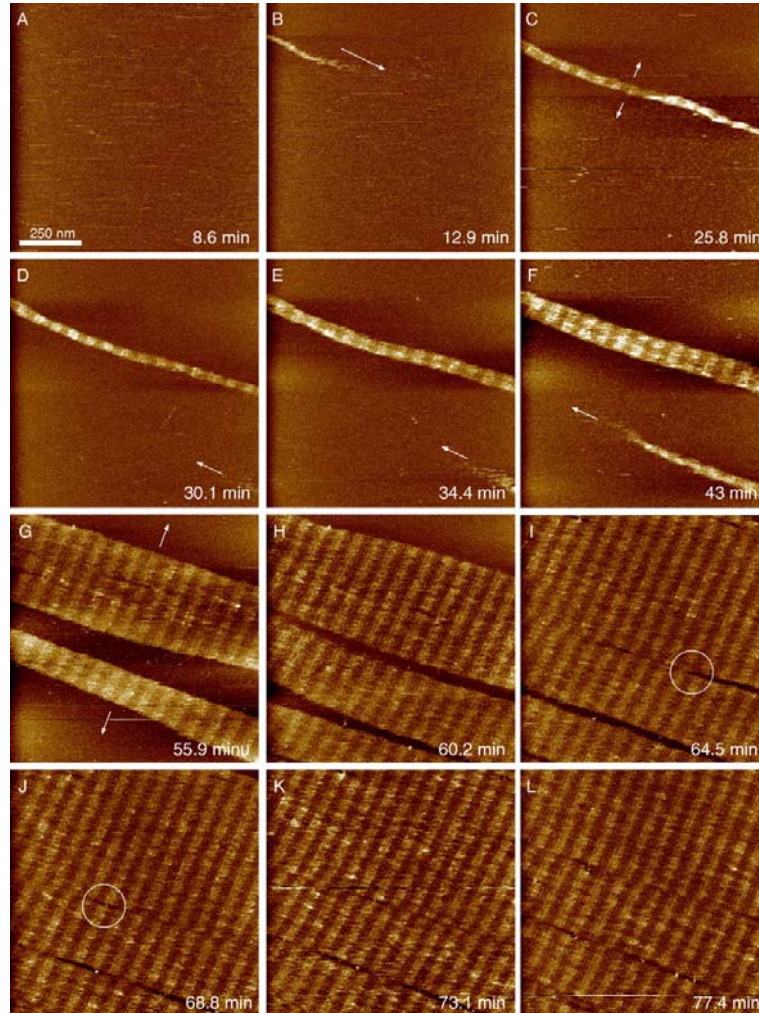


Figure 2.2. Observing collagen self-assembly by time-lapse TM-AFM. A-G) Topographs of laterally and longitudinally growing collagen fibrils (arrows). The D-band periodicity of single fibrils can be clearly resolved independently from the fibrillar width. D-F) A fibril growing longitudinally into the center of the topograph while the upper fibril grows laterally. G-I) The growing collagen fibrils assemble into a matrix that almost covers the entire supporting surface. Defects, such as formed by colliding interphases between two formerly separated fibrils (circle, panel I) disappear after a certain time (J-L). Eventually, the supporting surface is almost completely covered and almost all defects are annealed or minimized. Topographs were recorded in buffer solution (pH 9.2, 50 mM glycine, 200 mM KCl), at a collagen concentration of 12 $\mu\text{g/ml}$ at 27°C and exhibit a full gray level corresponding to a vertical scale of 5 nm.

Injection of a concentrated collagen solution into the assembly buffer (pH 9.2, 50 mM glycine, 200 mM KCl) initiated the growth of the fibrils on the mica surface as observed by time-lapse TM-AFM (Fig. 2.2). The first two topographs

revealed the adsorption of a single collagen fibril onto the mica surface (Fig. 2.2A-B). The fibril continuously grew laterally and longitudinally (Figs. 2.2B-C; arrows) while another fibril grew into the scanning frame (Figs. 2.2C-L). The longitudinal axes of both fibrils seemed antiparallel to each other as well as its growth directions (Figs. 2.2E-F). From these observations it can be concluded that single collagen fibrils simultaneously grew on both ends and sides.

After several minutes the width of both fibrils significantly increased until they came into contact (Figs. 2F-I). A third fibril was laterally approaching from the bottom of the topograph. Soon after, a third fibril joined the two previously fused fibrils. Apparently, the growing fibrils joined each other laterally (Figs. 2I-L) thereby forming a part of the 2D matrix that later on covered the entire supporting surface. The D-band periodicity established showed the same orientation throughout the collagen matrix.

The presence of the 67 nm periodicity (D-band) indicated that collagen molecules assembled into their native structure from the very first stage of their assembly. As directly revealed from the equally gray shaded structures of the topography, the collagen fibrils did not further increase their thickness after reaching their final height of 2.9 ± 0.3 nm ($n=34$ fibrils). Thus, we conclude that collagen microfibrils assembled into flat fibrils. These band-like structures, which finally established the ultraflat collagen matrix, were recently named microribbons (Jiang et al., 2004a).

In the early stage of fibril fusion it appeared that occasionally defects occurred in the 2D collagen matrix (Fig 2.2I-J; circle). After a certain time period some of the defects disappeared, suggesting that collagen molecules from the solution have filled the gaps in. Another interesting feature was the observation, that the D-periodicity of neighboring fibrils was slightly shifted against each other before fibril fusion. However, as two fibrils approached each other, their D-bands sometimes registered apparently, preventing a mismatch.

The smallest single fibrils observed (Fig 2.3A) exhibited a length of ~ 800 nm and a width of 21.4 ± 3.7 nm ($n=9$) measured at full-width at half-maximum (FWHM). The time-lapse AFM followed the growth of early fibrillar structures into larger fibrils as well (Fig 2.3A-C). Initially, these early collagen fibrils had a height of 1.4 ± 0.4 nm, and in subsequent assembly steps they increased their

height to ~ 3 nm (see above). Subsequently, the growing fibril laterally joined the thicker collagen fibril at the bottom of the topograph (Fig 2.3C).

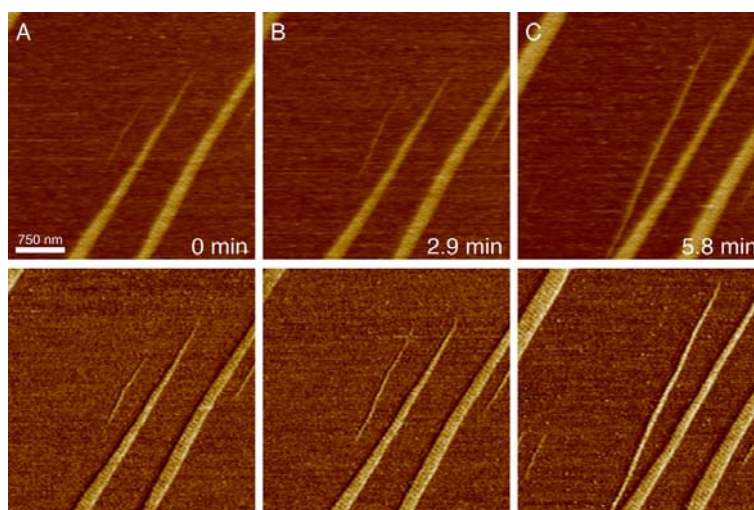


Figure 2.3. Lateral and longitudinal growth of fibrillar collagen structures at an early stage. TM-AFM topographs (top panel) and phase images (bottom panel) show single fibrils at different growth stages, each one exposing the typical D-band periodicity (≈ 65 nm) of collagen. The initial fibril continuously grew over the time. Images were recorded in buffer solution (pH 9.2, 50 mM glycine, 200 mM KCl), at a collagen concentration of $6 \mu\text{g/ml}$ and exhibited a full gray level corresponding to vertical scale of 5 nm for height and 15° for phase.

2.3.2. Observing tips of collagen fibrils fusing

Figure 2.4 describes the fusion of the tip of an early fibrillar structure with that of a larger collagen fibril. Initially (Fig 2.4A), the longitudinal axes of both fibrils were shifted in relation to each other and spatially separated (circle). In the next frame (Fig 2.4B) the gap was covered by a bent structure. As revealed from the vertical scale of the topography, the broad fibrillar structures protruded higher (≈ 3 nm) compared to the tips of the growing collagen fibrils 1.4 ± 0.4 nm ($n=16$).

2.3.3. Lateral vs. longitudinal growth kinetics

To obtain insights of the kinetics of the process, the fibril self-assembly was measured in dependence of the collagen concentration. The growth rates of the collagen matrix were determined for protein concentrations from 6 to $24 \mu\text{g/ml}$ (Fig 2.5). Recording one TM-AFM topograph required about 4 min. The growth of the matrix was determined as the surface coverage. As expected

(Kadler et al., 1996), growth curves vs. time showed a somehow sigmoid behavior and the process occurred faster at higher protein concentrations.

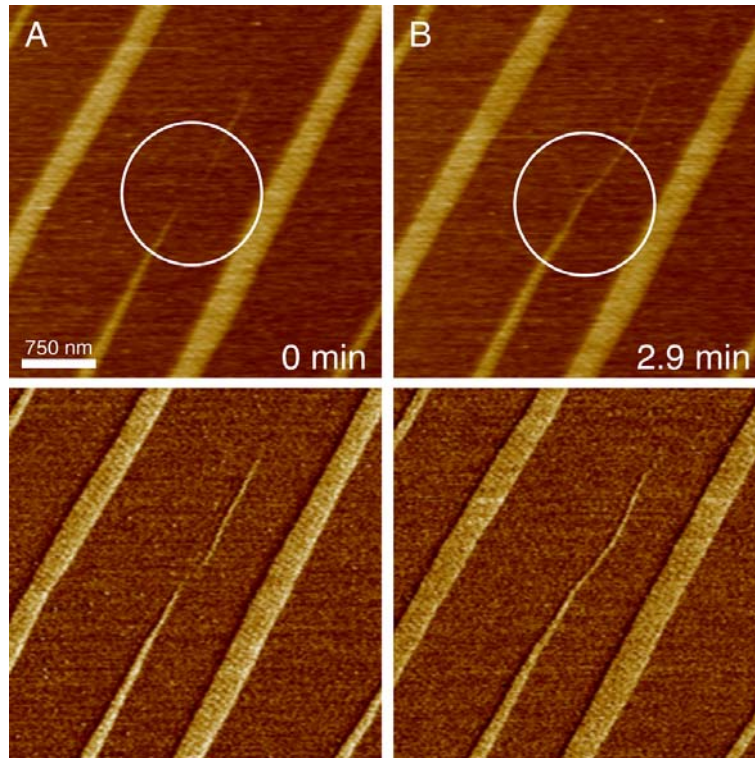


Figure 2.4. Fusion of two fibril ends. A) Collagen fibril prior to the fusion event. Top, topographs recorded using TM-AFM. Bottom, TM-AFM phase shift images of the same area. B) A collagen early fibrillar structure fusing with the thicker collagen fibril. Topographs were recorded in buffer solution (pH 9.2, 50 mM glycine, 200 mM KCl), a collagen concentration of 6 $\mu\text{g/ml}$ at 27°C and exhibit a full gray level corresponding to vertical scale of 5 nm for height and 15° for phase.

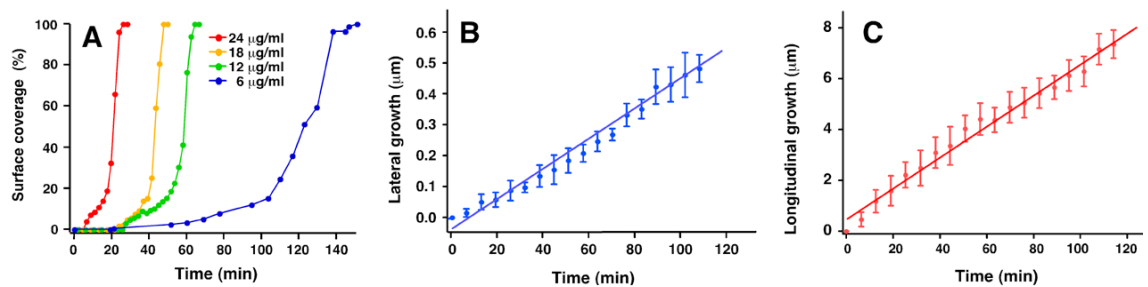


Figure 2.5. Concentration dependent self-assembly of collagen matrices and fibrils. A) Growth rate of collagen matrices covering the supporting mica surface were measured at different collagen concentrations. Lateral (B) and longitudinal (C) growth rate of single collagen fibrils at 6 $\mu\text{g/ml}$. All experiments were done in the same buffer solution (pH 9.2, 50 mM glycine, 200 mM KCl).

To measure kinetic properties of individual fibrils, we measured their relative longitudinal and lateral growth rates (Figs. 2.5B-C). The process was

slow enough only at 6 $\mu\text{g/ml}$, where we could track individual fibrils for a certain number of frames (Movie 1, supplementary material). The results are displayed as relative width or length vs. time plots. Linear fits allowed the estimation of the average lateral and longitudinal growth rates, which were 4.9 ± 0.005 nm/min and 60.6 ± 1.3 nm/min, respectively. Both grow rates were constant for a given collagen concentration until the supporting surface was fully covered. The lateral growth rates measured for early fibrillar structures (Fig 2.3) and for two fused fibrils (Fig 2.4) did not differ from the bulk ($\sim 4.8 \pm 0.4$ nm/min).

2.3.4. Revealing growth steps of single collagen fibrils

To enhance the temporal resolution of the TM-AFM, we scanned individual collagen fibrils by only a few height lines. The pixel size of the scanned profiles was smaller than 0.5 nm enabling a spatial resolution of 1 nm. To measure the relative width, a height profile of the fibril was made at every time point and its full width at half maximum was calculated (Fig. 2.6A). A width vs. time plot show that the width was kept constant for a few time points but it increased suddenly in discrete steps. The average growth step was 3.7 ± 1.3 nm ($n = 3$ movies), as presented in the histogram (Fig. 2.6C).

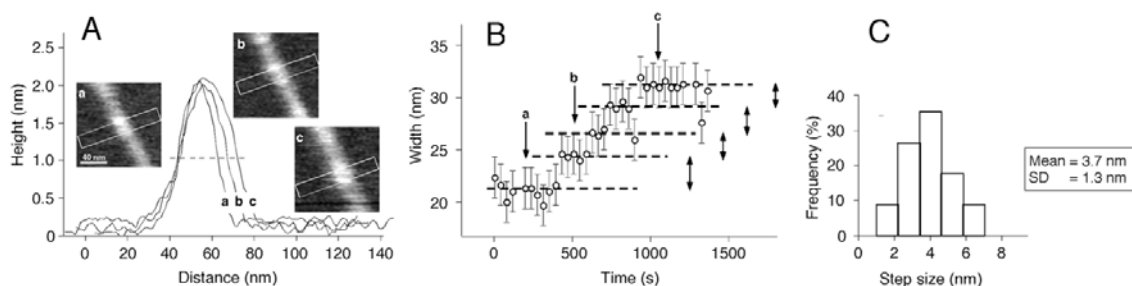


Figure 2.6. Observing growth steps of single collagen fibrils. A) Height profiles of a single collagen fibril (insets) recorded by TM-AFM. B) Width increment vs. time recorded for the fibril. C) Distribution of growth steps measured. The average step size of the fibrils was 3.7 ± 1.3 nm.

2.3.5. Substructural details beyond the D-band periodicity

To compare the structure of the matrix to previously describe ones we performed high-resolution imaging. The TM-AFM topographs revealed individual fibrils oriented at an angle of $\sim 15^\circ$ relative to the D-band axis (Fig. 2.7A). This observation was in excellent agreement with the 15° tilt observed for microfibrils forming corneal fibrils (Holmes et al., 2001), tendon fibers (Gutsmann et al.,

2005; Raspanti et al., 1989; Wess et al., 1998), and with recently published models of the collagen microfibril assembly (Engel and Prockop, 1998; Hulmes, 2002; Wess, 2005). AFM topographs recorded at higher resolution displayed distinct substructures within the D-periodicities (Fig. 2.7B). The corrugations resulted in banded patterns oriented in parallel to the D-bands. Averaging topographic segments (Fig. 2.7B; rectangle) enhanced the characteristic corrugations, which were repeated throughout the height profile of the D-bands. The averaged asymmetric height profile could be correlated the features of the unprocessed AFM topograph (Fig. 2.7B; lower panel).

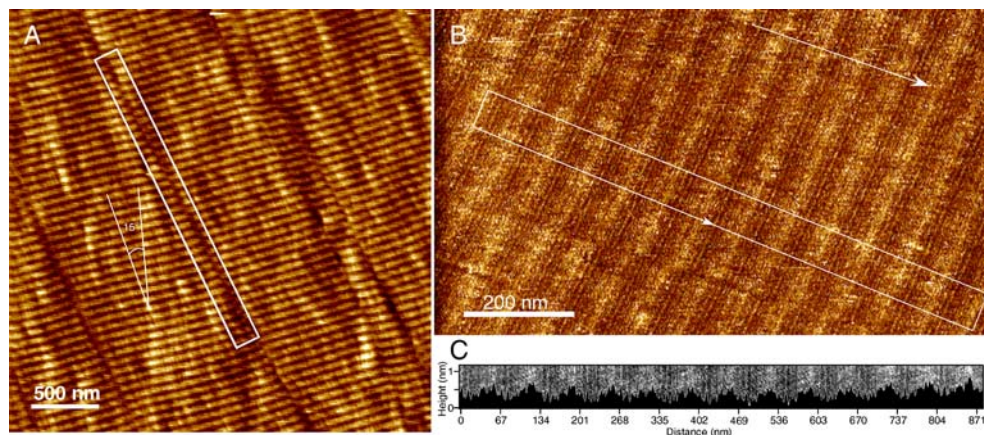


Figure 2.7. High-resolution TM-AFM topographs of self-assembled collagen matrices. A) Collagen fibrils are slightly tilted ($\sim 15^\circ$) in respect to the normal axis of the D-band periodicity. The D-bands exhibited height modulations of $\approx 0.4 \pm 0.1$ nm (compare Table 1). The rectangle outlines an interface of two overlapping collagen fibrils. B) Substructural details and height profile beyond the D-band periodic structure. The height profile of a selected area of 980 nm x 70 nm (rectangle in B) was averaged line by line transversally to the D-band. C) Merge of the averaged height profile and the unprocessed topograph (rectangle in B). Correlation of the height profile with the TEM data (Fig. 8) allowed determining the microfibril polarity establishing the matrix. The arrow points from the C- to the N-terminal end of the unipolar microfibrils. Topographs were recorded in buffer solution (pH 9.2, 50 mM glycine, 200 mM KCl) at 27°C and exhibit a full gray level corresponding to vertical scale of 5 nm (A) and 3 nm (B) in height.

2.4. Discussion

2.4.1. Collagen assembly observed by tapping-mode AFM

Collagen fibril formation is mainly an entropy driven self-assembly process (Engel and Prockop, 1998; Kadler et al., 1987; Kadler et al., 1996; McBride et al., 1992), which is generated by the loss of solvent molecules from

the protein surface. The formation of circular cross-sections between collagen molecules minimizes surface area and volume ratio of the final structure. Although many publications have contributed to the general understanding of the collagen fibril assembly (Christiansen et al., 2000; Holmes et al., 2001; Paige and Goh, 2001; Prockop and Fertala, 1998; Silver et al., 2003), the underlying self-assembly process was never been imaged directly.

Here we have developed an assay to characterize the self-assembly process of collagen into fibrils and highly ordered networks. Single fibrils showed constant growth rates depending on the collagen concentration in the buffer solution (Fig 2.5). Collagen molecules aligned on the mica surface following most likely the crystalline mica lattice, as it has been observed for α -synuclein fibrils (Heise et al., 2005). In all experiments performed in this work, the collagen fibrils did not grow in the direction vertical to the supporting surface. This suggests that the support formed an interface that guided the self-assembly of collagen into two dimensions. Thus, the growth kinetics was determined by the lateral and longitudinal growth rates of the fibrils. Time-lapse AFM movies showed that single fibrils grew independently from one another until they fused with adjacent fibrils (Fig 2.4B). At the end of the assembly the fibrils formed a continuous 2D matrix, which covered the entire supporting surface.

Assembled in certain buffer solutions, another collagen matrix can be grown on the first one (Jiang et al., 2004a). Instead of investigating the self-assembly of such almost three-dimensional collagen matrix, we have chosen a buffer solution in which the self-assembled fibrils were clearly distinguishable. This criterion allowed us to resolve steps of the lateral and longitudinal accumulation of collagen fibrils at high-resolution. We assume that the collagen fibrils self-assembled into their native structure, which is demonstrated by the D-periodicity and the substructural features observed at high-resolution (see below).

Under the experimental conditions studied here, we could not observe any self-regulation of the fibril width. After the assembly the collagen matrix covered the entire supporting surface, which could be several cm in diameter (Jiang et al., 2004a). The absence of self-regulation may be directly related to the absence of proteoglycans, which have been suggested to regulate the

lateral fusion of fibrils (Graham et al., 2000; Kadler et al., 2000; Kadler et al., 1996).

2.4.2. Minimum unit of fibril growth

In embryonic chicken, early fibrils have been described to have a length of $\sim 1\ \mu\text{m}$ (Kadler et al., 2000). These fibrils expose a particular axial mass distribution (AMD) in which the mass of the fibril increases from the fibril tip to a maximum point and then decreases without any plateau region, which indicate a non-uniform composition along them (Graham et al., 2000; Kadler et al., 2000). Other studies on the self-assembly of type I collagen suggest characteristic units that range in length from 4-D staggered dimers ($\approx 570\ \text{nm}$) (Kobayashi et al., 1985; Silver et al., 1979; Ward et al., 1986) to units that were about $700\ \text{nm}$ long (Bernengo et al., 1978). In both cases the unit lengths were between 2 and 3 collagen molecules in length, while the number of molecules that formed such a unit might range between 5 and 17. Estimates of the unit diameter range between 2 to $6\ \text{nm}$ (Gale et al., 1995). By TM-AFM the smallest isolated fibrillar units observed exhibited lengths of $\sim 800\ \text{nm}$, widths of $\sim 20\ \text{nm}$ and heights of $\sim 1.5\ \text{nm}$ (Fig 2.3). The height of the final collagen matrix was $\sim 3\ \text{nm}$. This suggests that the thickness of fibrillar collagen structures establishing the matrix changed from single layered molecules to that of microfibrils (Orgel et al., 2006).

However, the width of an object determined by TM-AFM is often subject to non-linear stylus-sample convolution artifacts and thus appears broader (Allen and Goldberg, 1992; Schwarz et al., 1994). It may be further assumed that isolated fibrils exhibit an enhanced mobility and flexibility on the supporting mica surface and thus appear wider when imaged. Therefore, considering this error, we suggest that early fibrillar structures (Fig 2.3) are not assembled yet into fibrils composed of microfibrils. This intermediate would represent a first step in the collagen self-assembly process. We assume that the final assembly of collagen molecules into microfibrils took place while forming the fibrillar structures of the higher order. A two-step mechanism may explain the collagen self-assembly into fibrils (see below).

2.4.3 Growth steps of collagen fibrils

In our experiments the smallest fibril units grew at the same rate as longer and wider fibrils. Recording profiles of individual fibrils at improved temporal resolution (Fig. 2.6) showed width increase in a stepwise manner. The spatial resolution of these experiments (≈ 1 nm) was about the width of one collagen molecule. However, in average the growth steps observed were ~ 3.7 nm, which corresponds well to the width of a single microfibril (Orgel et al., 2006). The constant lateral growth rates measured (Fig. 2.5B) could indicate that the proposed stepwise growth process did not change during the entire self-assembly process of the collagen matrix. This data support the idea that the smallest unit of fibril growth is a microfibril, suggesting that microfibrils could form the units or “building blocks” of the collagen matrix assembly. Apparently this interpretation is contradicted by the observation that the smallest isolated fibrillar structures show the height of 1.5 nm only. The two-step process of collagen assembly mentioned above assumes that collagen molecules bind with a certain rate constant to the growing fibril. In a second step, these molecules rearrange to form a microfibril. The observed step size of fibril growth (~ 3.7 nm) corresponds well to the average diameter (~ 3.3 nm) of a microfibril (Orgel et al., 2006). As mentioned, convolution effects occurring between the AFM stylus and the collagen fibril broaden the profile of the fibril width. In our experiments, structures protruding less than the fibril will not be imaged unless they laterally extend far enough to be detected by the AFM stylus (Allen and Goldberg, 1992; Schwarz et al., 1994). The AFM stylus cannot detect single collagen molecules laterally associating with a higher fibril until these molecules have increased their height by the formation of a microfibril. Thus, the observed growth steps could correspond to the collapse of several molecules into a microfibril when it incorporates into an already formed fibril.

2.4.4. Fibril fusion

TM-AFM topographs showed that adjacent collagen fibrils could either fuse laterally or by their ends. In about 50% of all cases, the regions of laterally fused fibrils showed no or only very little structural mismatch of their D-periodicity. However, in other cases a mismatch between the joining fibrils was observed as a shift in their D-band periodicities (Fig. 2.7A). It was previously

showed that fibrils assembled from acid-soluble collagen, such as used in this work (see materials and methods), are unipolar, D-periodic and have two smoothly tapered ends (Graham et al., 2000; Kadler et al., 1996). Such unipolar fibrils can fuse in a number of ways. Unipolar fibrils containing collagen molecules with oriented amino N- to carboxyl C-terminus could fuse in side-by-side register resulting in fibril thickening. Fibrils of the same orientation could also fuse in end-to-end register resulting in fibril lengthening. End-to-end fusion of two oppositely oriented unipolar fibrils is also possible, yielding a bipolar fibril. Such a fusion occurs exclusively between two fibrils interacting by their C-terminus. Side-by-side fusion of two oppositely directed unipolar fibrils is, however, not allowed according to current models describing the collagen fibril fusion (Kadler et al., 1996).

Analysis of our experimental data shows that two fibril ends that are connected by end-to-end fusion never exhibited a mismatch of their D-periodicity. This supports the above model that oppositely oriented unipolar collagen molecules can approach and fuse with each other. However, there must be a certain flexibility of the collagen molecules to establish the conditions to fuse. Fused fibrils showed no kinks, which would also suggest rearrangements on the fibrils after fusion. Since molecular interactions occurring between two fibril ends may be too low to physically move the entire fibrils immobilized to the surface, their termini must exhibit a certain flexibility which enables their rearrangement for coordinated fusion. Long-range interactions may also assist in aligning the fibril ends and staggering them in the right manner. Such flexibility was observed by the example shown in Figure 2.4. This observation agrees well with that of collagen matrices in which individual fibers could be mechanically rearranged only during the first hours of the assembly process (Jiang et al., 2004b).

Adjacent fibrils that grew towards each other were frequently observed to fuse laterally (side-by-side). In about 50% of all cases the periodic D-bands of fused fibrils showed no mismatch. Because two independently growing fibrils cannot align their D-bands before interacting with each other, we assume that long-range interactions may align approaching fibrils so they can stagger in the right manner to facilitate their fusion.

The molecular basis for the flexibility of type I collagen results from sequences lacking amino acids proline and hydroxyproline. Electron microscopy data (Hofmann et al., 1984), modeling studies (Paterlini et al., 1995) and stereochemical maps (Silver et al., 2002) suggest that regions lacking of proline and hydroxyproline exhibit an increased flexibility and thus can adopt more conformations than other regions of the triple helix. In contrast regions with the sequence Gly-Pro-Hyp are very rigid. Hence, the collagen triple-helix can be considered a composite of regions with varying degrees of stiffness (Silver et al., 2003). Furthermore, it has been recently postulated, that the type III collagen molecule is more flexible than the type I one and that mixing of both collagen types would increase the elastic modulus of the fibrils (Silver et al., 2002). Since we used a mixture of $\approx 97\%$ type I and of $\approx 3\%$ type III collagen in this work, we assume that both the molecular flexibilities contributed by the collagen molecule itself and by the mixture of both collagen types may facilitate the collagen self-assembly into the highly ordered fibrillar matrix.

In all other cases (50%) when collagen fibrils fused, we observed a mismatch between the D-bands of two fused collagen fibrils (Fig. 2.7). Apparently, these fusing collagen fibrils could not stagger at their interface. We do not know how the collagen molecules were rearranged at this interface. AFM topographs recorded at subnanometer resolution may in future reveal the precise arrangement of single collagen molecules at such interfaces. Side-by-side fusion of two unipolar fibrils may result in a perfect match of their D-bands. In contrast, side-by-side fusion of two antiparallel molecules would result in a mismatch such as observed here. High-resolution TM-AFM topographs clearly show a directionality of the D-band structure and may further support this hypothesis (see below).

2.4.5. Collagen self-healing

Time-lapse TM-AFM topographs showed that fusing collagen fibrils could leave structural gaps in the growing collagen matrix. However, in about 50% of all cases, the gaps disappeared after a certain time period (Fig 2.2). It was recently observed that after mechanical removal of collagen molecules from rat-tail tendon the molecules could bind back to the fibril (Gutsmann et al., 2005). It was suggested that this self-organization and self-healing significantly

contributes to toughness and strength of tendon fibrils. During wound healing myofibroblasts increase the synthesis of the ECM and decrease its degradation (Grinnell, 2000; Grinnell, 2003). Such self-organizing capabilities of collagen to heal out defects could contribute to a faster and more efficient tissue repair.

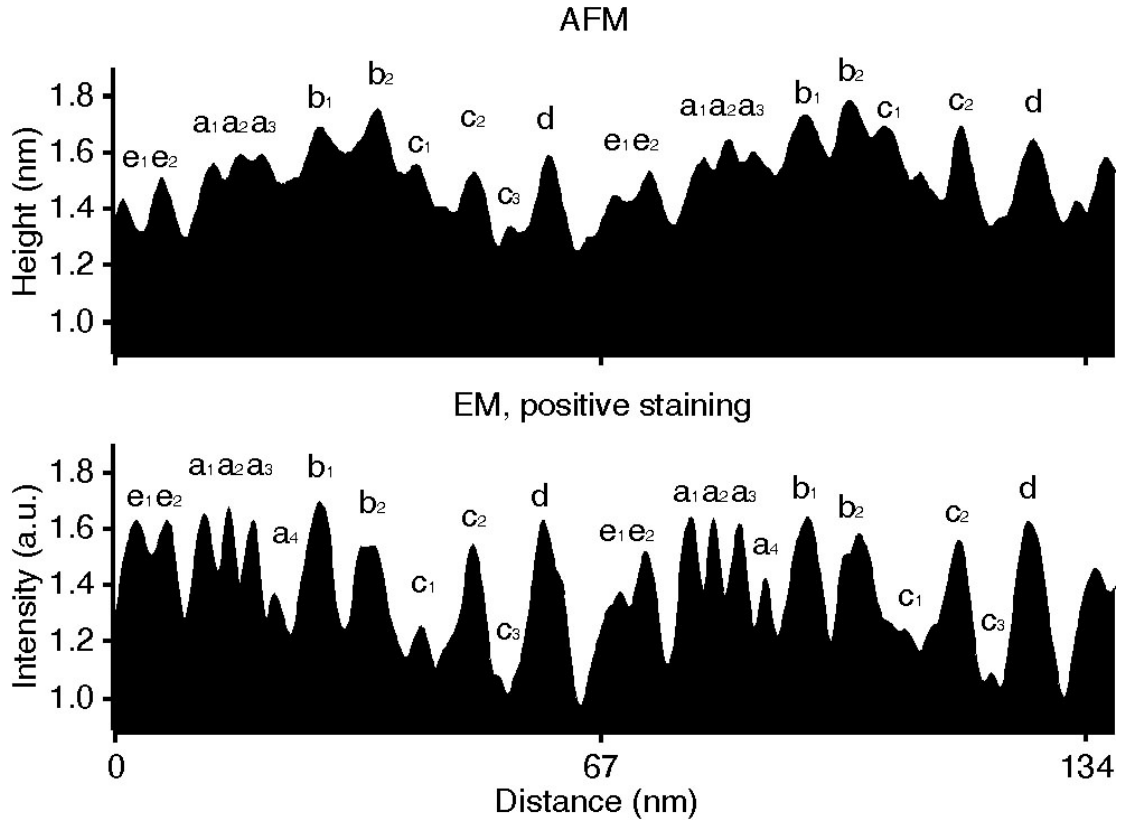


Figure 2.8. Comparing an averaged TM-AFM height profile of collagen with the TEM density profile. The top panel shows the averaged AFM height profile of Fig. 2.7. The lower panel shows the density pattern revealed from positively stained collagen fibrils by TEM (Chapman et al., 1990; Meek et al., 1979). Labeling of the pattern follows the conventional notation in which groups of closely spaced bands are denoted by a, b, c, d, and e. Individual bands within a group have numerical prefixes a_1 , a_2 , etc. TM-AFM height and TEM density profiles were aligned by correlation analysis. All height protrusions of the TM-AFM profile correlate well with the density of the bands obtained by positive stain TEM.

2.4.6. Collagen matrices possess structural characteristics of tendon

Collagen fibrils self-assembled under the conditions used here established the characteristic D-band periodicity of ~67 nm such as observed by EM or AFM of *in vivo* assembled collagen fibers. High-resolution TM-AFM topographs (Fig. 2.7) of hydrated fibrils clearly resolved a multibanded substructure of the D-periodic collagen. After aligning the height profile with the TEM density profile (Fig. 2.8B) by cross correlation, these structural details of

the D-band could be correlated to bands observed by TEM of positively stained collagen fibrils (Chapman et al., 1990; Meek et al., 1979). The height of each protrusion of the D-banded substructure is given in Table 2.1.

TEM images of collagen exhibited a more detailed substructural information if the collagen fibers were positively stained instead of the more frequently used negative staining (Chapman et al., 1990; Graham et al., 2000; Kadler et al., 2000; Meek et al., 1979). The structural information obtained from positively stained collagen fibrils showed an excellent agreement to AFM topographs revealed from native unstained collagen fibrils down to a lateral resolution of ≈ 2 nm (Chapman et al., 1990). So far, such excellent structural correlations were only obtained between negatively stained specimen observed by TEM and the AFM data revealed from native biological samples (Karrasch et al., 1994; Schabert et al., 1995). It is assumed, that positive staining contrasts the biological specimen in a different way than negative stain, which can be easily recognized by comparing TEM images of collagen fibrils stained by either one of both approaches (Chapman et al., 1990; Graham et al., 2000; Kadler et al., 2000; Meek et al., 1979). Positive stain contrasts mainly electrostatic information of a biological sample and the uptake of stain by collagen fibers is therefore assumed to be determined by the nature and abundance of charged side-chains on the collagen surface (Chapman et al., 1990). Hence, TEM data obtained from positively stained fibrils may be directly correlated with chemical information of the collagen. In contrast, AFM topographs normally contour protein surface structures (Müller et al., 2002). However, it was recently shown, that under certain circumstances AFM topographs could be a composite of structural and electrostatic information of the protein surface (Philippson et al., 2002). These electrostatic interactions, are suppressed at sufficiently high electrolyte concentrations such as used to record the high-resolution topographs shown here. Thus, we may assume that both topographical and chemical information of collagen fibrils are identical up to a resolution of ≈ 2 nm.

2.4.7. Orientation of collagen molecules within the matrix

From density profiles revealed by TEM the polarity (orientation) of collagen molecules within tendon can be determined (Chapman et al., 1990). The correlation between AFM height and TEM density profiles (Fig. 2.8) allowed

us to determine the orientation of collagen molecules assembled into the matrix (Fig. 2.7).

2.5. Conclusions

We have established an assay to observe the growth and fusion of individual collagen fibrils. The lateral and longitudinal fusion of single fibrils could be directly followed until they formed the final collagen matrix. The kinetic parameters of the collagen assembly suggest that both the longitudinal and lateral growth of the collagen fibrils at a low concentration were mainly determined by a two-step process describing the assembly of collagen molecules followed by the formation of microfibrils. The collagen fibrils within this matrix possessed the typical longitudinal 67 nm periodic structures such as observed in the case of the fibers assembled *in vivo*. Furthermore, the structure of these matrices corresponds to the one found *in vivo* and could therefore be used as scaffolds for the construction of biocompatible materials. AFM topographs of native fibrils within this collagen matrix revealed substructural details of the D-band such as observed by high-resolution TEM in *in vivo* assembled collagen.

Band	Average height (nm)	Standard deviation (nm)
C2	0.32	0.08
C3	0.12	0.05
D	0.31	0.07
E1	0.23	0.05
E2	0.25	0.05
A1	0.32	0.06
A2	0.35	0.07
A3	0.34	0.08
A4	N.D.	N.D.
B1	0.43	0.07
B2	0.48	0.06
C1	0.24	0.08

Table 2.1. Average height of collagen bands substructuring the D-periodicity. A topographic area of $\sim 68 \mu\text{m}^2$ (980 nm x 70 nm) of the collagen matrix was averaged line by line. The protrusions could be assigned to the collagen bands by comparing the TM-AFM profile to the TEM data (Chapman et al., 1990). N.D. means not determined.

3.0. A new method to prepare membrane proteins for single molecule imaging

3.1. Introduction

3.1.1. Structure determination of membrane proteins

Membrane proteins are underrepresented in the database of high-resolution structures from X-ray and nuclear magnetic resonance (NMR) (White, 2004). Furthermore they often form large and sometimes transient supramolecular complexes. Alternative approaches, such as cryo-electron microscopy (cryo-EM) and AFM, are essential tools able to provide complementary information on the structure-function of membrane proteins in more native environments. Two approaches increase the resolution of these methods, 2D-crystallisation and single particle reconstruction. For cryo-EM, crystals provide electron diffraction data which can increase resolution, while single particle averaging can be used for proteins >200 kDa. High-resolution AFM topographs can reveal structural details of single native membrane proteins but, as a prerequisite, the proteins must be adsorbed to atomically flat mica and densely packed in a membrane to restrict their lateral mobility (Müller et al., 2002). While averaging of single particles shows their common structures, selected examples can be used to characterize structural flexibility, variability and conformational changes (Engel and Müller, 2000; Scheuring et al., 2002).

Attempts have been made to prepare membrane proteins for AFM imaging avoiding crystalization (Milhiet et al., 2006). Milhiet *et al.* prepared lipid supportive bilayers on mica and reconstituted membrane proteins by solubilizing them with detergents. The samples observed in that study were most of them ironically crystalline (Milhiet et al., 2006). On the other hand, many examples of AFM analysis of self-assembled monolayers on gold supports have been published (Leggett, 2003; Love et al., 2005; Tinazli et al., 2005; Wagner et al., 1994; Wagner et al., 1996). Alternatively, thiolipids have been developed to create membrane mimetic surfaces on gold (Lang et al., 1994; Naumann et al., 2003; Stora et al., 1999; Tamada et al., 1997; Terrettaz et al., 1993; Terrettaz et al., 2002). However these have not yet been combined to prepare membrane proteins. In this chapter, a covalent assembly approach for membrane protein

imaging that avoids crystallization is demonstrated. For this purpose the well-characterized outer membrane protein OmpF from *Escherichia coli* was used. Single OmpF trimers were visualized by TM-AFM with similar resolution as previously reported for 2D crystals.

3.1.2. Structure and function of OmpF

Two lipid bilayer membranes surround Gram-negative bacteria such as *E. coli*. The space between these membranes, called the periplasm, contains the peptidoglycan layer. Both membranes contain proteins that are in charge of transporting solutes across. About 50% weight of the outer membrane consists of integral membrane proteins or lipoproteins anchored to the membrane (Koebnik et al., 2000). Some of these proteins form pores and were accordingly called porins. Porins translocate hydrophilic molecules to the periplasmic space with a molecular weight up to 600 Da. Structures determined for members of this family showed a β -barrel structure (Koebnik et al., 2000). Particularly, 16 strands connected by loops compose the structure of the general porin OmpF (Cowan et al., 1992b). One of this loops (extracellular loop 3) folds back into the barrel, determining some of the permeability properties (Fig 3.1A).

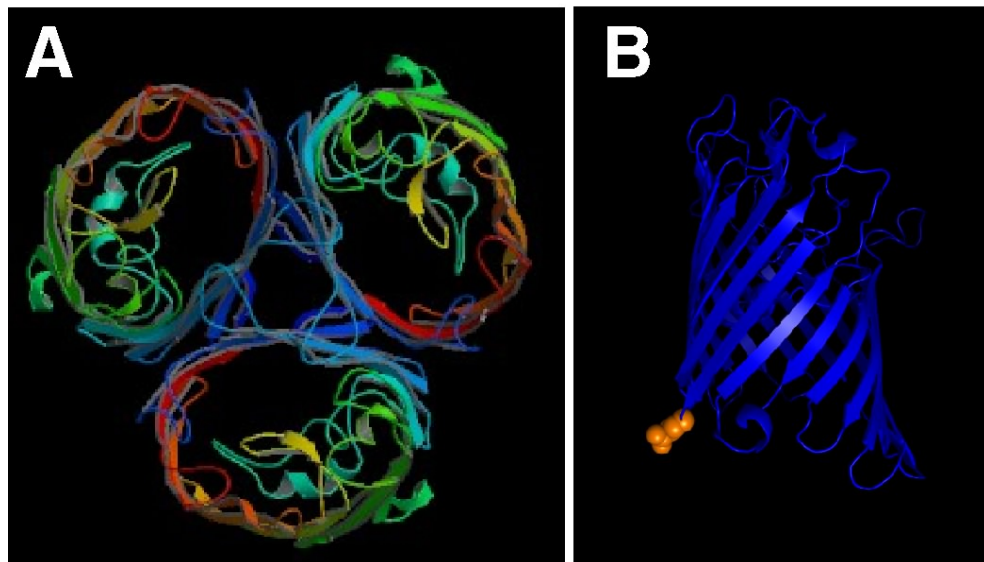


Figure 3.1. Structure of OmpF. A) OmpF porin has a homo-trimeric structure as observed from the extracellular side in the plane of the membrane. B) View from the membrane plane of OmpF trimer showing residue Glu183 (PDB code 2OMF). The structure of each monomer is composed of a 16 stranded β -barrel.

3.2. Material and methods

3.2.1. OmpF-E183C production and purification

OmpF-E183C was kindly provided by Prof. Jeremy Lakey (University of Newcastle upon Tyne, UK). The E183C mutation was introduced into OmpF using a site-directed mutagenesis commercial kit (Quickchange, Stratagene Inc.) and purified as described previously (Terrettaz et al., 2002).

3.2.2. Preparation of gold supports

Gold supports were kindly provided by Prof. Jeremy Lakey (University of Newcastle upon Tyne, UK). Evaporated gold was prepared as described (Terrettaz et al., 2002). Template-Stripped gold (TS-gold) surfaces were prepared as described (Hegner et al., 1993; Wagner et al., 1995). Briefly, gold was evaporated on freshly cleaved mica. The mica was then glued to a silicon support with Torr Seal epoxy glue (Varian), with the gold surface facing the epoxy. The mica was subsequently removed by immersing briefly the support in liquid nitrogen until it separated from the epoxy. The gold remained on the epoxy leaving a flat gold surface. The silicon support was then glued to a steel disc commonly used to mount samples for AFM.

3.2.3. Assembly of OmpF-E183C on template-stripped gold

TS-gold surfaces were treated with 10 mM β -mercaptoethanol for 20 min before washing and incubation with protein (0.25 mg/ml in 300 mM NaCl, 50 mM Tris-HCl, pH 7.5) and 1 mM tris(2-carboxyethyl)phosphine hydrochloride (TCEP). Protein incubations were for a minimum of one hour. The samples were washed with buffer with 1% (v/v) octylglucopyranoside (OG). Then, samples were incubated with buffer containing 0.5 mg/ml thiolipid (1,2Dipalmitoyl-sn-Glycero-3-Phosphothioethanol; Avanti Polar Lipids, USA) for at least 1 h at 45°C. Control TS-gold surfaces were incubated in thiolipid or alkanethiol (18-hydroxy-n-octadecylthiole) for at least two hours.

3.2.4. AFM and image analysis

The AFM (MultiMode, DI-Veeco, CA) was operated in buffer solution using a fluid cell. The piezoelectric scanner had a scan range of ~120 x 120

μm^2 . Oxide sharpened Si_3N_4 cantilevers had a nominal force constant of 0.08 N/m (OMCL TR400PS, Olympus Ltd, Tokyo). Imaging was performed in tapping mode with a drive frequency close to the resonance frequency of the cantilever (9.5 kHz) immersed in buffer solution (150 mM NaCl, 50 mM Tris-HCl, pH 7.8). The drive amplitude of the cantilever was set to a root mean square (RMS) value of 18 - 30 nm. All samples were imaged in buffer solution at room temperature (23°C). Single particles extracted from the topograph (trace and retrace) shown in Fig. 3A ($n=40$) were aligned and correlation averaged using the software Semper. The final average was three-fold symmetrized. This procedure was identical for the topographs from 2D crystals (Müller and Engel, 1999).

3.3. Results

3.3.1. Assembly strategy

OmpF can be covalently assembled on gold surfaces if a single cysteine residue is inserted into one of the intracellular loops. For this purpose a mutation (E183C) in one of the intracellular loops was introduced. When covalently bound to a gold surface through the engineered cysteine residue, the protein exposes its extracellular surface. The assembly process consists of: 1) Passivating the gold surface with a short chain thiol (Fig 3.2A), 2) adding OmpF-E183C in detergent solution (Fig 3.2B) and 3) completing the remaining surface with a layer of thiolipid in which the headgroup contains a thiol able to chemisorb to the gold surface (Fig. 3.2C). This approach has shown to maintain the native structure of OmpF-E183C (Terrettaz et al., 2002).

3.3.2. OmpF-E183C assembled on evaporated gold

As a first approach evaporated gold on a silicon surface was used as a support. The conservation of the OmpF-E183C native structure on this gold was proved by various methods including, fourier transformed infrared spectroscopy (Terrettaz et al., 2002) and neutron refraction (Holt et al., 2005). A sample at the second step of assembly on evaporated gold was observed by AFM (Fig 3.2B). As a control, evaporated gold without protein was examined. For the protein sample, the gold surface was incubated with OmpF-E183C solubilized

in OG detergent. In the topograph, trimeric particles that matched the dimensions of OmpF-E183C were observed (Fig 3.3B, circles). In contrast, the sample without protein showed no trimeric structures (Fig 3.3A). The roughness of the gold sample is clearly larger than the height of the OmpF-E183C particles. Therefore, there was no possibility to perform high-resolution imaging.

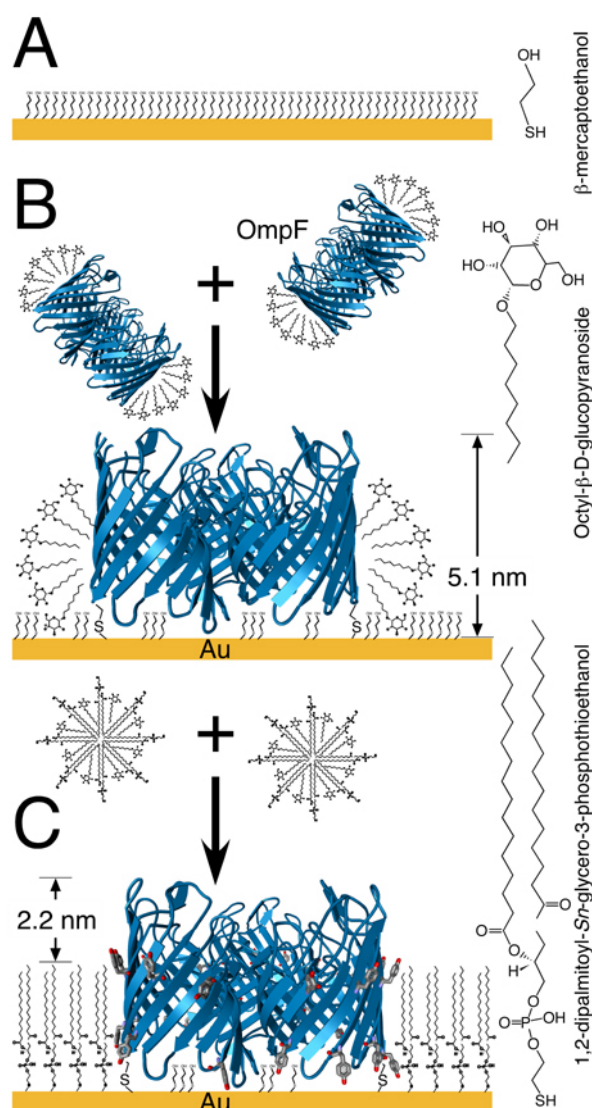


Figure 3.2. OmpF assembly strategy. A) The gold surface is passivated by β -mercaptoethanol. B) OmpF-E183C trimers in octylglucopyranoside (OG) micelles attach to gold surfaces via cysteine mutation E183C. C) Mixed OG/thiolipid micelles are added which assemble a thiolipid monolayer. Subsequent washing with OG containing and detergent-free buffer removes free lipid and detergent leaving a hydrophobic half bilayer on the gold support. Due to the relatively thin cross section of outer membrane proteins, the hydrophobic region of the OmpF-E183C protein (aromatic residues) is effectively stabilized by the 3 nm thick lipid monolayer (see text for details).

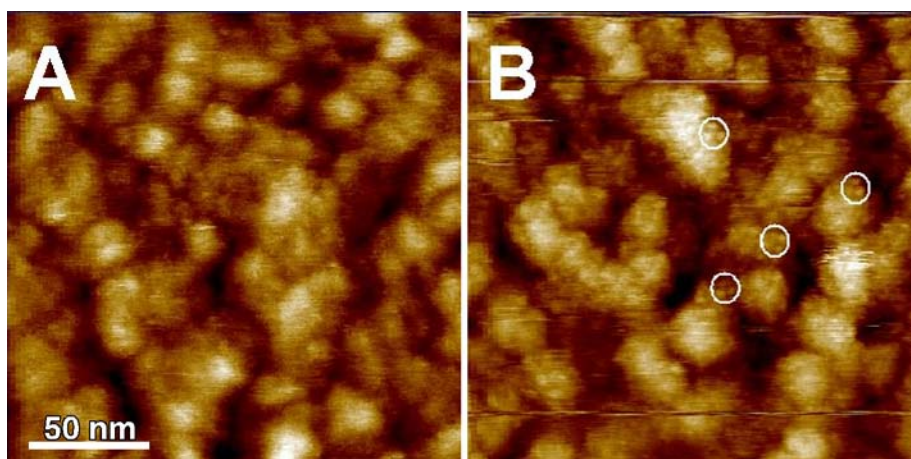


Figure 3.3. Assembly of OmpF-E183C onto evaporated gold surfaces. A) Control surface of evaporated gold. B) Gold surface incubated with protein in a detergent solution (Step 2).

3.3.3. Template-stripped gold yields a flat surface

To improve the flatness of the surface, template-stripped gold (TS-gold) was used instead of the evaporated gold. TS-gold is prepared by evaporating gold on a mica surface. Because mica is atomically flat, removing the mica is supposed to leave a flat gold surface. When observed by AFM the TS-gold supports didn't appear flatter than the evaporated gold (Fig 3.4A). The corrugations on the sample could be debris from the mica or from the cleaving process. To verify this, a small area was scanned at high force (~ 10 nN). When the area was inspected at lower magnification, it was observed that some debris was removed from the sample, and that the underlying area was indeed flat (Fig 3.4B).

3.3.4. Thiolipid assembly removes debris from TS-gold

To control that the thiolipid did not introduce any topographic feature, a TS-gold surface with thiolipids was incubated and inspected by AFM. The surface presents a clear background only with a few very high features. These however, could not be confused with OmpF-E183C trimers because they are too big and irregular (Fig 3.5). Furthermore no corrugations similar to the mica debris on the TS-gold were found. This result suggests that the covalent assembly of thiolipids on the gold removes chemically the remaining mica debris.

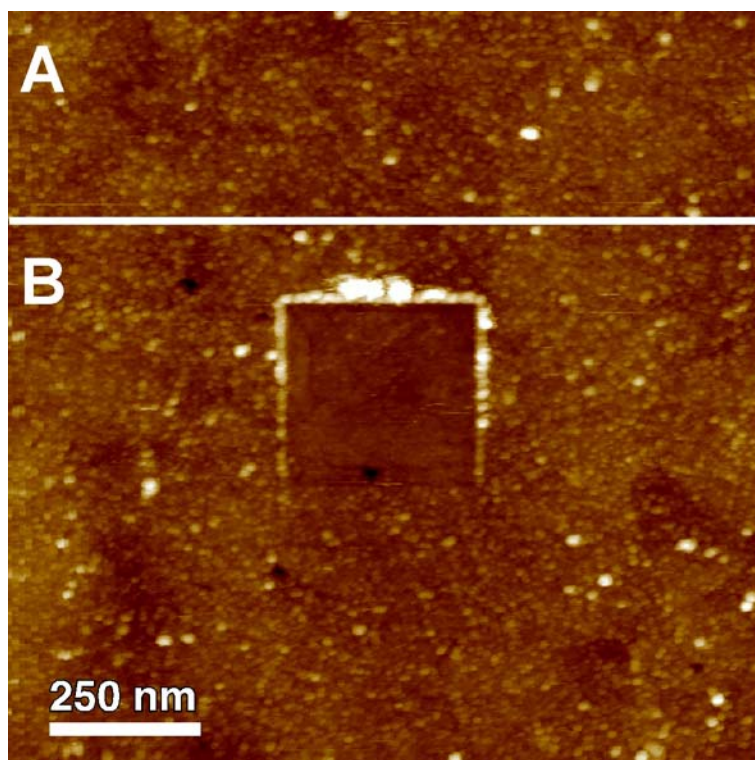


Figure 3.4. Template stripped gold surface. Two zones of the same topograph are shown A) Gold surface after cleaving the mica where the gold was deposited. B) Gold surface where the debris was removed by scraping the surface with the AFM stylus.

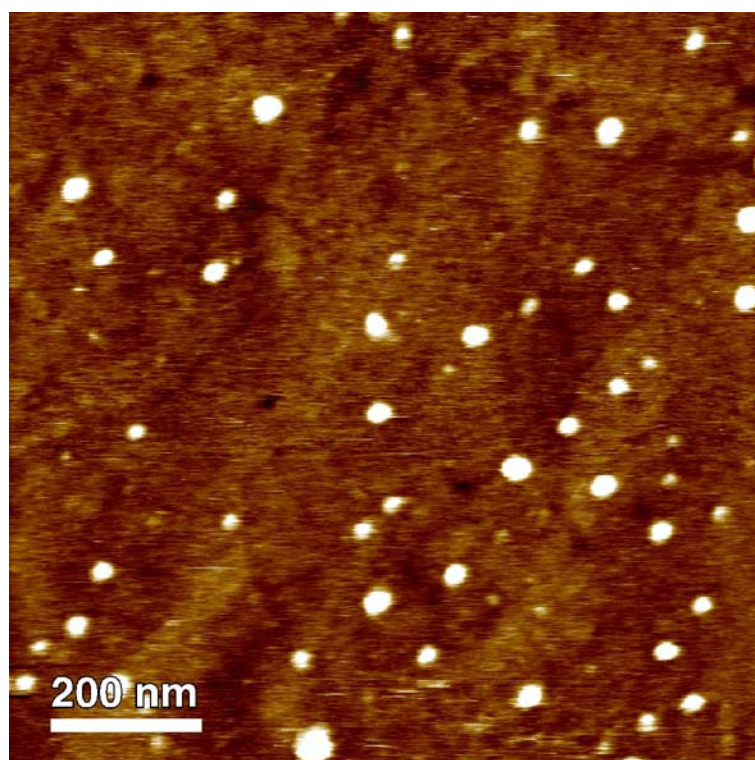


Figure 3.5. Thiolipid assembled on TS-gold. A gold support after thiolipid assembly showed an homogenous surface.

To assess the possibility that the thiolipid was chemically removing debris from the cleaving process on the surface, a self assembled monolayer (SAM) on the TS-gold was assembled. An eighteen carbon chained alkanethiol (18-hydroxy-n-octadecylthiole) was used to substitute the thiolipid. The results show an even more dramatic effect of the alkanethiol compared to the thiolipid. The surface is completely homogenous without any topographical feature (Fig 3.6). This suggests first that both the thiolipid and the alkanethiol remove debris from the gold surface, and second that the thiolipid could be assembling as a SAM.

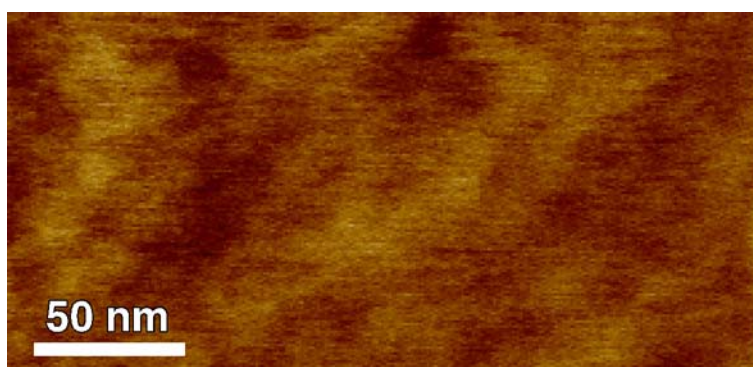


Figure 3.6. TS-gold assembled with SAM. A 20 carbon alkanethiol was assembled on the gold, the surface present no debris or contaminant.

3.3.5. OmpF-E183C assemblies on TS-gold

To test whether TS-gold would yield a support suitable for high-resolution AFM imaging, the second assembly step on TS-gold was visualized by AFM. For this purpose OmpF-E183C solubilized in OG detergent was incubated on a TS-gold surface. To our surprise, the resulting topograph showed many high features and some features with the size of OmpF trimers. Some features showed trimeric structures resembling OmpF (Fig 3.7, circles). This result suggests that at least some molecules of OmpF bound covalently exposing the extracellular surface. The other features likely represent misoriented proteins or protein aggregates.

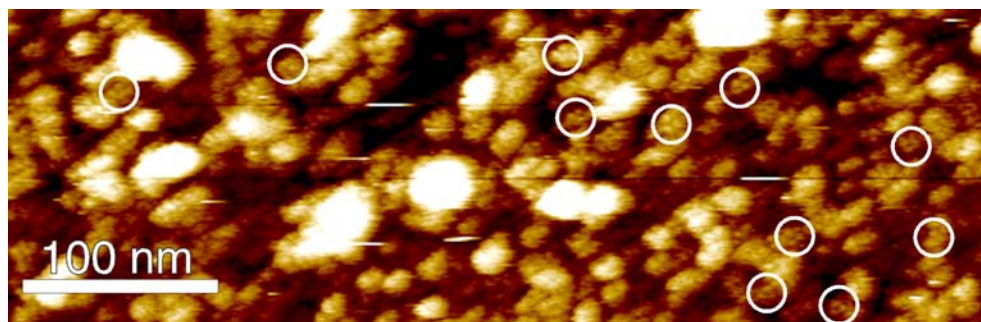


Figure 3.7. OmpF-E183C assembled on TS-gold. The white circles mark the structures that resemble OmpF-E183C trimers.

The height of the trimeric particles observed in Figure 3.7 was measured to confirm that they were OmpF trimers. A cross section of two subunits of every particle was made (Fig 3.8A). The particles protruded 5.5 ± 1.3 nm in average ($n=18$), which matches the height of OmpF covalently bound to the gold (Fig 3.8B).

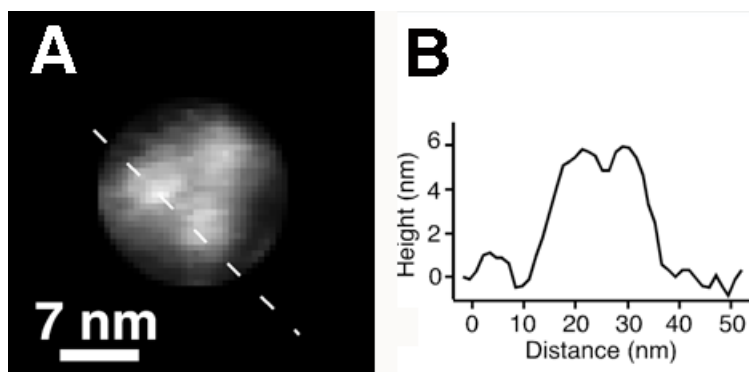


Figure 3.8. Cross section of an OmpF trimer on TS-gold. A) Image of a single particle from fig 3.7. B) Height profile of two OmpF subunits along the dotted line shown in A.

The full assembly of protein with thiolipid (3rd step) looked dramatically different (Fig 3.9). A TS-gold surface was incubated first with OmpF-E183C and then with thiolipids. The topograph shows a clear background and many trimeric features with dimensions matching those of OmpF. These results suggested that the area surrounding each trimer is flat enough to perform high-resolution imaging. Moreover, the thiolipids removed chemically almost all the features observed in the sample without thiolipids.

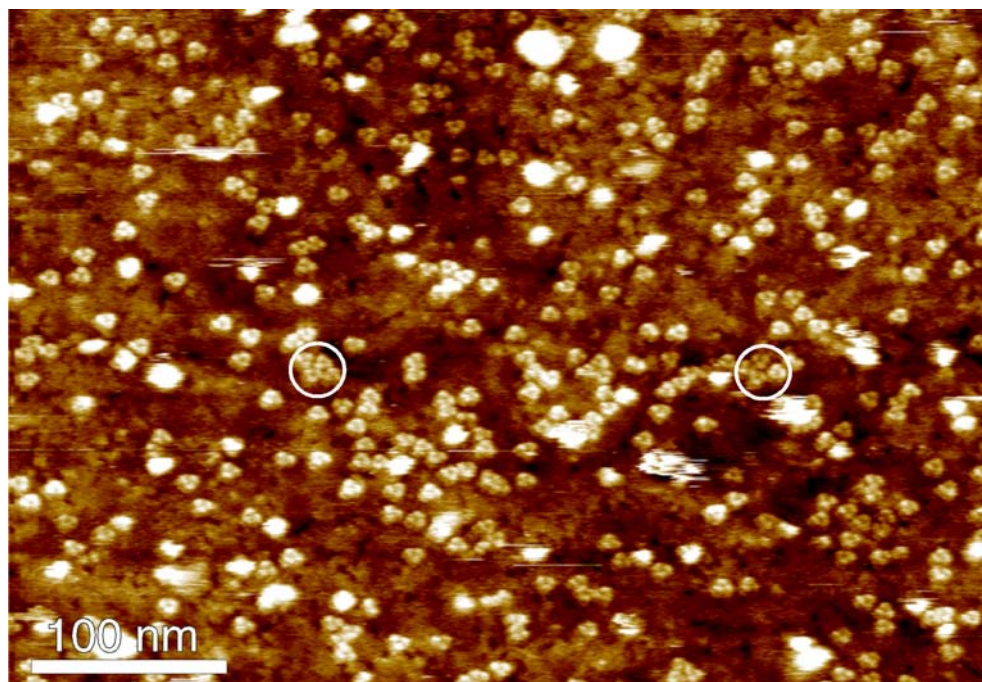


Figure 3.9. OmpF-E183C covalently bound to gold assembled with thiolipids.

To confirm that OmpF-E183C was embedded in the thiolipid, the height of all the trimeric structures was measured. A cross section of the particles was made along two monomers and the height to the surface measured (Fig 3.10A). The particles protruded 2.2 ± 0.4 nm in average (Fig 3.10B). Since the thiolipid is ~ 3 nm long, the average height correlate to OmpF trimers protruding from a thiolipid monolayer (compare to the height of the sample without thiolipids).

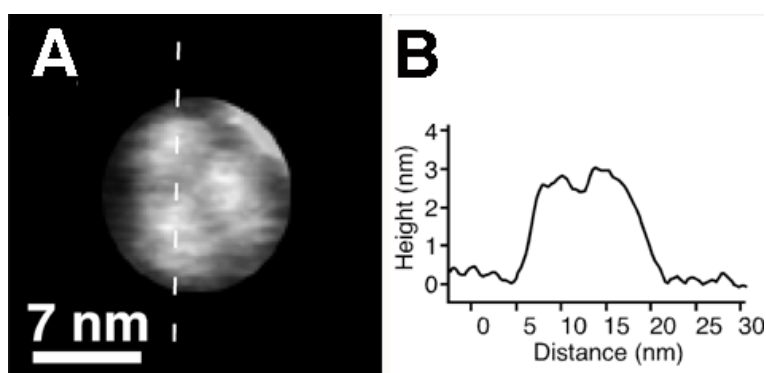


Figure 3.10. Cross section of OmpF-E183C trimer embedded in thiolipids. A) Image of a single particle from fig 3.9. B) Height profile of two OmpF subunits along the dotted line shown in A.

3.3.6 High-resolution OmpF-E183C

The protein assembly on TS-gold is flat enough to perform high-resolution imaging. When observed at higher magnification (Fig. 3.11A), the trimeric structures clearly resemble the extracellular surface of OmpF (Müller and Engel, 1999). To compare our results to previous studies (Müller and Engel, 1999), correlation averages of single OmpF trimers were made (3.11B-C). The obtained correlation averages were similar to correlation averages obtained from 2D crystal topographs (3.11D-E).

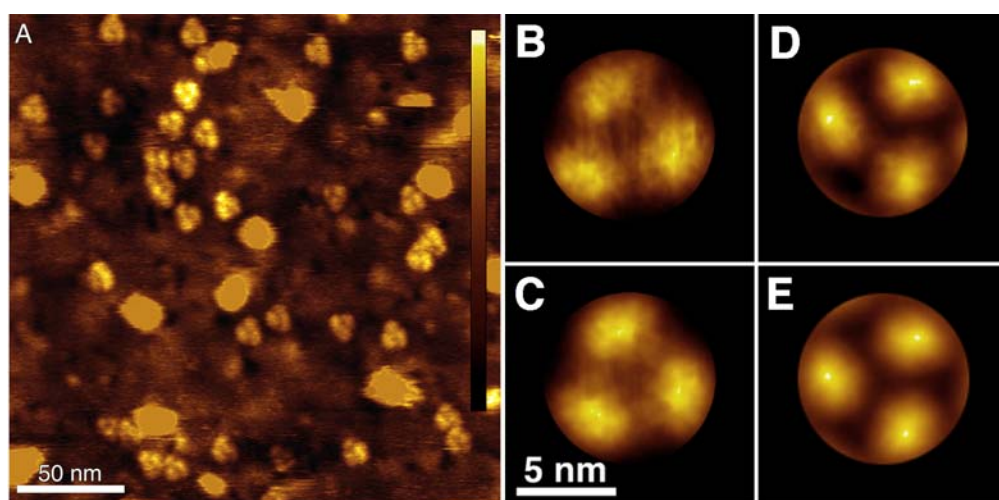


Figure 3.11 High resolution imaging of OmpF-E183C assembled on TS-gold. A) High resolution topograph of OmpF-E183C. Non-symmetrized (B) and symmetrized (C) correlation average of particles observed in A. Non-symmetrized (D) and symmetrized (E) correlation average of OmpF extracellular surface obtained from 2D crystals (Müller and Engel, 1999).

3.4. Discussion

3.4.1. TS-Gold and thiolipids make a suitable support for AFM imaging

The use of gold supports represents advancement to surface science because components can be covalently bound to it. Another major step was the invention of SAMs, which are thioalkanes able to bind covalently to gold. Their name derives from the ability to form a molecular film, which is stabilized by hydrophobic lateral interactions, similar to lipids in a biological membrane. Applications of gold with SAMs supports in biology include optical and chemical biosensors (Shin et al., 2006).

In the approach used in the present work, gold supports were used to investigate structural properties of a membrane protein. For this purpose, two types of gold supports were tested. Comparing evaporated gold (Fig. 3.3) with TS-gold (Fig. 3.4) surfaces, clearly shows that the roughness of evaporated gold is not suitable for high-resolution imaging because it contains depressions with a depth of several nanometers. In contrast, TS-gold presents a flat surface. Moreover, application of thiolipids to the TS-gold surface improves its quality by removing chemically any debris remaining from the stripping process. A similar effect could be the cause of the difference in the amount of large non-trimeric particles between the sample with and without thiolipid.

3.4.2. Imaging of membrane proteins embedded in thiolipids

TS-Au covered with a thiolipid monolayer provided a control background (Fig. 3.5). This half-bilayer of immobilised phospholipid may act like a hydrophobic SAM of methyl-terminated alkane thiols (Bain and Whitesides, 1988). Recent studies show that interaction forces of the hydrophilic Si_3N_4 tips with very hydrophobic SAM layers are very low (Subramanian and Sampath, 2005; Yang et al., 2004), thus enabling the acquisition of clear AFM topographs. Under these conditions (Fig. 3.7), poorly defined OmpF-E183C trimers were observed. Nevertheless, these trimers protruded ~ 5.5 nm above the support, corresponding to the height of their 3D structure (Fig. 3.8) (Cowan et al., 1992a). However, after incubation with thiolipid, the images were greatly improved, revealing individual trimers protruding ~ 2.2 nm above the surface (Fig. 3.9). The height difference of ~ 3.3 nm confirmed that the trimers were embedded in a thiolipid monolayer (Fig. 3.8B vs. 3.10B). From the measurements performed in this study, it is not known whether a screening layer of tightly bound detergent may have resisted the washing with detergent-free buffer solutions (Popot et al., 2003; Thomas, 2004). Such remaining detergents may shield the hydrophobic tails from the thiolipids (Fig 3.2C) that would otherwise be exposed to water. It has been shown, however, that detergents like OG dissociate from similar hydrophobic surfaces when diluted below their critical micellar concentration (Sigal et al., 1997).

The improvement of the sample background after thiolipid assembly may be due to two effects: the removal of poorly attached OmpF-E183C after

competition with thiolipid, and the reduction of possible lateral displacements by a rigid thiolipid layer. Although the protein solution used should contain non-aggregated individual trimers, small groups (25% of 393 trimers) of closely contacting trimers arranged as in 2D crystals were observed. This possibly implies a cooperative assembly of OmpF-E183C trimers at the surface (Figure 3.9, white circles). Previously, SPR, FTIR (Terrettaz et al., 2002) and NR (Holt et al., 2005) data of OmpF-E183C were collected on evaporated and therefore rougher gold surfaces. Comparable topographs from these samples are presented in figure 3.3B. Therefore, the results also show that the overall structure of OmpF is not affected when bound to rough gold. Using TS-gold gives the advantage of enabling high-resolution imaging on the sample.

3.4.3. High resolution imaging of OmpF-E183C

Images of single OmpF-E183C trimers ($n=40$) assembled on TS-AU were averaged (Fig. 3.11B-C) using the same approach as used previously on 2D crystals (Fig. 3.11D-E). The resulting images clearly resolve the three individual protrusions of the OmpF-E183C trimer (Cowan et al., 1992a). Furthermore, all the particles resemble the extracellular surface of OmpF-E183C and not the periplasmic one (Müller and Engel, 1999). Therefore, our data shows that the cysteine mutation ensures 100% orientation of the protein and that, surprisingly, the exposed hydrophobic face of the thiolipid monolayer provides a smooth non-interacting background for AFM imaging. While the method should be readily applicable to many outer membrane proteins, it could be extended to the study of other type of membrane proteins. In particular, by avoiding crystallization, the tiny quantities required make the study of complexes that are hard to purify more attractive. In this work the proteins were fixed close to the surface, using thiolipids with hydrophilic spacers could be used to stabilize proteins with water soluble domains (Lang et al., 1994). Finally, the engineering scaffold properties of the β -barrel proteins suggests that these oriented layers are capable of contributing to the development of precise nanoscale biointerfaces (Lang, 2000; Terrettaz et al., 2002).

3.5. Conclusions

In conclusion, a simple method to prepare membrane proteins for AFM imaging was developed. A membrane protein with a cysteine mutation, fixed in a defined orientation on a flat gold surface, can be used to obtain high-quality AFM images under aqueous conditions without 2D crystallization. The main benefit for AFM imaging is that lateral displacements of proteins by the AFM stylus is avoided thanks to the covalent assembly. The approach presented could be readily applied to observe membrane proteins and obtain preliminary information about their structure, such as its oligomeric state. Another advantage is that the sample could be applied without any further procedure immediately after purification and in very low quantities. Furthermore, a second layer of lipids could be fused to the first one to complete a bilayer. For this purpose, the synthesis of thiolipids of various lengths would be very useful to fulfill special requirements of other membrane proteins. Additionally, the resolution obtained is similar to the one obtained for 2D crystals. To our knowledge, this is the first time that a diluted sample of membrane proteins is visualized using AFM at such resolution.

4.0. Collective interactions determine the stability of archaeal rhodopsins

4.1. Introduction

4.1.1. Structure and function of archaeal rhodopsins

Photoactive membrane-embedded retinylidene proteins (rhodopsins) are used throughout the animal and microbial kingdoms as receptors for light (Spudich, 2006). In the case of haloarchaea, four light-activated retinal proteins are found. These are: the inwardly directed chloride pump halorhodopsin (HR), the outwardly directed proton pump bacteriorhodopsin (BR), as well as two photoreceptor sensory rhodopsins (SR) SRI and SRII. After light excitation, the phototactic receptors SRI and SRII undergo conformational changes and transfer the signal to their tightly bound cognate transducer proteins (HtrI and HtrII, respectively), thereby initiating a phosphorylation cascade that regulates the flagellar motors (Spudich, 2006). When oxygen and respiratory substrates are abundant, the negative phototaxis receptor SRII is expressed (Landau et al., 2003). Blue-light activation of SRII exerts a repellent response allowing the host to escape potential photo-oxidative damage. In unfavorable light conditions, orange-light activation of SRI elicits an attractant to illuminated areas with better growth-conditions. Under these circumstances BR and HR are co-expressed in large quantities and energy transduction proceeds via photosynthesis (Landau et al., 2003). SRI also mediates a strong repellent response when it is activated by two sequential photons (i.e. orange followed by near-UV light) (Spudich, 2006). The molecular weight of these proteins lays around 26 kD, and their polypeptides fold into seven transmembrane α -helices named from A to G. A Schiff base covalently links the photoactive retinal to the last helix G. HR represents the only light-driven anion pump known so far and is present in haloarchaea and at least in one halophilic bacterium (Sharma et al., 2006). When over-expressed in *Halobacterium salinarum*, HR forms two-dimensional (2D) crystals with a $P4_212$ symmetry (Havelka et al., 1993). In this symmetry space group, tetramers exposing their cytoplasmic and extracellular surfaces are alternated in a tetragonal lattice. Investigation of these 2D crystals by electron crystallography allowed developing a three-dimensional (3D) structural model at a resolution of ~ 5 Å (Havelka et al., 1995; Kunji et al., 2000).

The atomic model of HR, which was solved by X-ray crystallography, confirmed the extremely high structural similarity of HR with that of the light-driven proton pump BR (Kolbe et al., 2000). Moreover, several structures of SRII from *Natronobacterium pharaonis* with transducer (Gordeliy et al., 2002) and without transducer (Luecke et al., 2001), show its structural similarity to BR and HR.

4.1.2. Membrane protein folding in vivo

For the case of helix-bundled membrane proteins, cells have the challenge to insert the very hydrophobic transmembrane helices from the aqueous cytoplasmic environment. Cells overcome this by coupling translation of membrane proteins to insertion. *In vivo*, insertion occurs through the translocon machinery (for a review see White and von Heijne, 2005). The current model establishes that polypeptides arise from the ribosome tunnel exit and are recognized by a protein called the signal recognition particle (SRP). The SRP binds both to the polypeptide and to the ribosome and arrests elongation (White and von Heijne, 2004). Then, the ribosome-SRP complex docks to the membrane bound SRP-receptor at the exterior surface of the endoplasmic reticulum (ER). Both SRP and SRP-receptor are GTPases that become activated when the ribosome is docked to the ER. This process disengages SRP from the ribosome and the nascent protein is transferred to the translocon (White and von Heijne, 2004). The translocon is composed of heterotrimeric proteins called Sec61 in mammals and SecY in bacteria. The machinery of archaea resembles more the one of eukaryotes than the one of eubacteria (Albers et al., 2006). The translocon contains a hypothetical lateral gate that opens to let hydrophobic helices slide into the lipid bilayer (White and von Heijne, 2004). In such a scheme, a transmembrane helix will partitionate into the bilayer due to its hydrophobicity, whereas a more hydrophilic one will simply go through the translocon channel into the lumen of the ER (White and von Heijne, 2004). As of the folding of the polypeptide into a helix, it was suggested that the process can occur inside the ribosome prior to translocation (Woolhead et al., 2004).

In vivo folding experiments of BR have also been performed. Pulse-chase studies on the insertion of bacterioopsin (BR without retinal) showed that

the folding occurs sequentially from helix A, then helices B and C, and then F and G. Helices D and E could not be resolved (Dale et al., 2000).

4.1.3. Unfolding single membrane proteins

Single-molecule experiments provide complementary information to that obtained from bulk experiments (Zhuang and Rief, 2003). With an innovative approach, single molecule force spectroscopy (SMFS) was applied to study the iterative unfolding and re-folding of the muscle protein titin (Oberhauser et al., 2001; Oberhauser et al., 1999; Rief et al., 1997). Oesterhelt *et al.* unfolded the first membrane protein by SMFS (Oesterhelt et al., 2000). In this study, after imaging of individual BR molecules at subnanometer resolution, the AFM tip was attached to the terminal end of the protein, which was then unfolded and extracted from the membrane by applying an external pulling force. Using the same approach, unfolding and refolding was observed for the transmembrane sodium-proton antiporter NhaA from *Escherichia coli* (Kedrov et al., 2004).

4.1.4. Membrane proteins follow various unfolding pathways

Single molecule unfolding experiments in BR demonstrated that all force vs. distance traces showed the same overall profile. Nevertheless, small differences between them made them unique. This observation led to the notion that each molecule took a different pathway to unfold (Muller et al., 2002c). The probabilities of these pathways depended on temperature (Janovjak et al., 2003) and pulling speed (Janovjak et al., 2004). It was observed that slight temperature variations shifted significantly the probability of individual unfolding pathways. Accordingly, the probability of secondary structures to unfold collectively was higher at elevated temperatures while they preferentially unfolded individually at low temperatures (Janovjak et al., 2003).

4.1.5. Biological significance of mechanical membrane protein unfolding

To predict membrane protein structures, two main questions have to be solved. The first one is to decipher the mechanism in which these proteins fold *in vivo*. The second is to map the interactions that stabilize membrane proteins in the anisotropic environment of the lipid bilayer (White and von Heijne, 2004). The latter is one of the aims of SMFS on membrane proteins.

Contrary to the proposal that protein folding occurred as a chemical reaction, in 1997, a 'new view' of protein folding was proposed by Ken Dill. He suggested that the folding of a protein may occur in a multi-pathway reaction (Dill and Chan, 1997; Yon, 2002). In this respect, single-molecule force spectroscopy has given a significant contribution by observing the multiple unfolding pathways of a protein (Muller et al., 2002c). SMFS showed that unfolding of BR occurs via different pathways that involved the unfolding steps of single secondary structure elements. However, it was shown that these structural elements exhibited distinct probabilities to unfold together or separately. The probabilities of these unfolding events depended on the intrinsic roughness of the energy landscape determined by potential barriers mapping the protein structure (Janovjak et al., 2004).

To investigate the contribution of specific amino acid residues to the stability of membrane proteins, unfolding pathways of BR, HR and preliminary data obtained for unfolding of SRII were compared. As for BR, HR unfolded through intermediates determined by regions of the polypeptide that unfolded cooperatively. In an attempt to understand whether molecular interactions stabilizing these regions are determined by the secondary structure or by its polypeptide sequence, the secondary and tertiary structures of the segments were compared. The results show that in the case of archaeal rhodopsins, different amino acids (aa) can establish the same stabilizing structural segments (*i.e.* at the same locations) to resist unfolding.

4.2. Material and methods

4.2.1. Protein purification

Purified HR and BR 2D crystals were kindly provided by Prof. Dieter Oesterhelt (MPI of Biochemistry, Martinsried, Germany). BR was purified from *H. salinarum* as described (Heymann et al., 1993). 2D crystals of HR were produced by over-expressing it in a D2 *H. salinarum* strain and purified as BR (Heymann et al., 1993). Briefly, cell lysates were centrifuged and applied to a sucrose gradient (25% to 45% w/v) and fraction with the highest density was recovered. SRII was kindly provided by Dr. Johann P. Klare (MPI for Molecular Physiology, Dortmund). SRII was over-expressed as a His-tagged protein in *E.*

coli (called here only SRII for simplicity) and purified by affinity chromatography using a Ni-NTA agarose column (Qiagen, Hilden, Germany). The protein was then reconstituted into purple membrane lipids with a 1:1 (w/w) protein to lipid ratio (Hohenfeld et al., 1999).

4.2.2. AFM imaging

To obtain high-resolution AFM topographs, the 2D-crystals were adsorbed to freshly cleaved mica (Muller et al., 1997) in buffer solution (50 mM TRIS-HCl, 300 mM KCl, pH 7.8) (Muller et al., 1999a). Contact mode topographs were recorded using a commercial AFM (Nanoscope E, Veeco Instruments, Santa Barbara, CA). Images were obtained using Si₃N₄ cantilevers (OMCL TR-400-PS, Olympus, Tokyo and NP-S, Veeco Instruments, Santa Barbara, CA) with a nominal spring constant of 0.08 N/m.

4.2.3. Single-molecule unfolding

Single-molecule force spectroscopy on BR, HR and SRII was performed after high-resolution imaging (Janovjak et al., 2003; Muller et al., 2002c; Oesterhelt et al., 2000). 2D crystals (for the case of BR and HR) were adsorbed to mica and imaged by AFM. For SRII, membrane patches containing reconstituted protein were adsorbed to the mica support and visualized. After imaging, the AFM operation was changed to force mode. The AFM tip was then pushed onto the protein until the terminus adsorbed to the cantilever by unspecific interactions (Janovjak et al., 2003; Oesterhelt et al., 2000). Then, the AFM tip was retracted from the membrane surface at a velocity of ~ 90 nm/s for HR and ~300 nm/s for BR and SRII. Force vs. distance curves were obtained recording the cantilever deflection (i.e. force) over the separation length.

Si₃N₄ cantilevers (OMCL TR-400-PS, Olympus, Tokyo and NP-S, Veeco Instruments, Santa Barbara, CA) were used for both imaging and force spectroscopy. Within an accuracy of ~ 10 % all cantilevers showed a spring constant of around 0.08 N/m (Olympus) and 0.07 N/m (Veeco). The spring constant of each cantilever was calculated using the equipartition theorem (Butt et al., 1995; Florin et al., 1995).

4.2.4. Data analysis

In previous studies, the total length of the force curves has been used to discard force curves that came from attachment events of the AFM tip with regions of the polypeptide that do not belong to one of the termini (Muller et al., 2002c). This criterion was applied in the present study. However, since the 2D HR crystals showed a $P4_21_2$ symmetry, both C- and the N-terminus were exposed to the same surface of the membrane. This implied that the force curves detected pulling the N-terminus had to be distinguished from those pulling the C-terminus. Because both HR termini exhibited different lengths, it was expected that force curves obtained by pulling the N-terminal end (4 aa) would be shorter compared to those pulling the C-terminal end (19 aa). Consequently, only long force curves that came from unfolding HR by pulling its C-terminus were selected. The force curves selected showed lengths between 65 and 70 nm corresponding to a stretched polypeptide being $\sim 210 - 223$ aa long (Muller et al., 2002c). Similarly to the alignment procedure applied to BR, the force curves obtained from HR were aligned at their second main peak. Later on, these curves were compared with those observed for BR unfolding pulled from the C-terminus (Janovjak et al., 2003; Muller et al., 2002c; Oesterhelt et al., 2000).

The N-terminus of SRII is embedded in the membrane as part of helix A. Therefore, the probability of it to adsorb to the cantilever's tip is assumed to be very low. As a consequence, as for HR, force curves derived from N-terminal unfolding would be short and can be excluded by the length criteria. Therefore, only curves exhibiting a length larger than 65 nm were selected for analysis.

To analyze side peaks, every main peak was superimposed separately. Each force peak was fitted using the WLC model (Section 1.3.5). The contour length (L) of the stretched polypeptide was obtained from the fit assuming a persistence length (l_p) of 0.36 nm (Oesterhelt et al., 2000). When pulling the protein from the cytoplasmic surface, sometimes the anchor of the stretched polypeptide segment is embedded in the membrane. In this case, the lipid membrane thickness (~ 4 nm) had to be considered, and 11 aa ($11 \times 0.36 \text{ nm} \approx 4 \text{ nm}$) were added to the number of aa determined by the WLC model (Muller et al., 2002c). Alternatively, if the segments were shorter than the width of the

membrane, a fraction of the membrane thickness (11 aa) proportional to the length of the apparent stretched polypeptide was added. The polypeptide lengths derived from the WLC fits were compared with the HR structure determined by X-ray crystallography (Kolbe et al., 2000)(PDB code 1E12). For the case of SRII, lengths derived from the WLC fits were compared to structure 1JGJ (Luecke et al., 2001). WLC fits of BR unfolding were compared to structure 1BRR (Essen et al., 1998).

4.3. Results

4.3.1. High-resolution imaging of halorhodopsin

To characterize HR crystals, high-resolution AFM imaging was performed. Topographs recorded in buffer solution (Fig. 4.1) show HR tetramers arranged into a 2D lattice. Since the 2D crystal exhibit a $P4_212$ symmetry, adjacent HR tetramers exposed either their extracellular or cytoplasmic surface to the aqueous solution (Fig. 4.1B). The correlation averaged topography (Figs. 4.1C,E) enhanced common structural details among individual HR molecules. Previously, those tetramers that were protruding less from the lipid bilayer were assigned to be seen from their cytoplasmic surface, and the more protruding ones from the extracellular surface (Persike et al., 2001). The three protrusions of the cytoplasmic surface extend 1.1 ± 0.09 nm, 0.8 ± 0.12 nm and 0.6 ± 0.09 nm from the lipid bilayer. Monomers of extracellular surface type only showed one dominant protrusion of 1.2 ± 0.16 nm. The standard deviation map of the correlation average (Figs. 4.1D-E), showed two main features. Both maxima of 0.16 nm and 0.08 nm correlated to the protrusion of the extracellular surface (Figs. 4.1C-E). The perspective representation of the averaged topography (gold) mapped by the standard deviation (red) allows the precise correlation of the information.

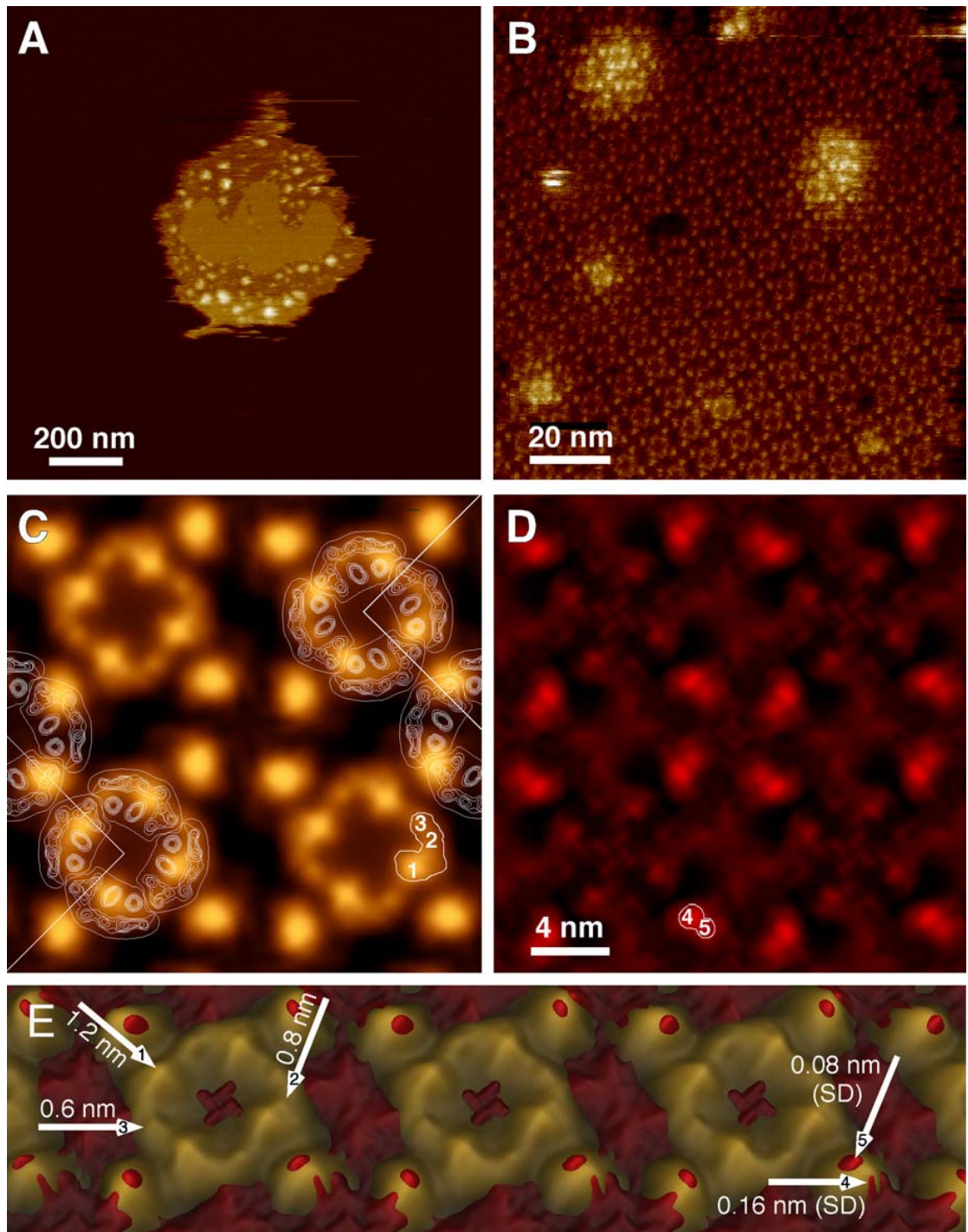


Figure 4.1. High-resolution AFM topograph of a two-dimensional halorhodopsin (HR) crystal. A) Adsorbed 2D crystal of HR on mica at low magnification. B) Unprocessed topography such as obtained by AFM imaging in buffer solution (50 mM TRIS-HCl, 300 mM KCl, pH 7.8) at high resolution. C) Correlation average of the topography shown in (B). The density map of HR revealed from Cryo-EM (Havelka et al., 1993) was outlined. The two possibilities of the outlines explain the structural features observed in the AFM data with the sidedness of the tetramers. D) Standard deviation map of the correlation averaged topograph. E) Surface map of the averaged topograph shown in a perspective view with a tilt of 20°. The standard deviation map (red) was superimposed. The vertical range is scaled in colors ranging from black to white with 15 nm (A), 1.5 nm (B), 1.2 nm (C), 0.2 nm (D) and 1.2 nm (E).

4.3.2. Halorhodopsin unfolding

To compare the unfolding pathways of HR and BR. HR and BR were force-unfolded as it was previously done for BR. HR and BR 2D crystals were adsorbed onto mica and imaged by AFM. After imaging, the AFM was changed to the force mode and extension-retraction cycles were performed over the 2D crystal. Force curves were obtained and selected to match the length of the protein pulled from the C-terminus (~70 nm), as it is described in Material and Methods. Representative curves from BR and HR are shown in Figure 4.2A and 4.2B, respectively. Spectra of BR and HR force unfolding showed three peaks that appeared with 100% frequency, called here main peaks (Fig. 4.2A-B). As shown previously (Bustamante et al., 1994; Rief et al., 1997), these peaks, which represent the stretching of a polypeptide segment, can be described using the worm-like chain (WLC) model (Bustamante et al., 1994; Rief et al., 1997). The WLC describes the entropic force-dependent stretching of a polymer (section 1.3.5).

The superimposition of the force curves enhances the common features among the force spectra (Fig. 4.2C-D). The three main peaks from each curve build up the main density. In a previous study, Müller *et al.* unfolded BR using SMFS (Muller et al., 2002c). In that study, BR unfolding force traces were obtained in correspondence to the ones shown in Figures 4.2A-B. Simulating the WLC with stretched polypeptides of ~88 aa, ~148 aa and ~219 aa describes well the density of superimposed curves as it was previously shown (Figure 4.2B, red curves). By correlating the length with the structure of BR, Müller *et al.* showed that the 88 aa, 148 aa and 220 aa peaks corresponded to the simultaneous (called pairwise) unfolding of helices D & E, B & C and to the one of helix A, respectively (Muller et al., 2002c).

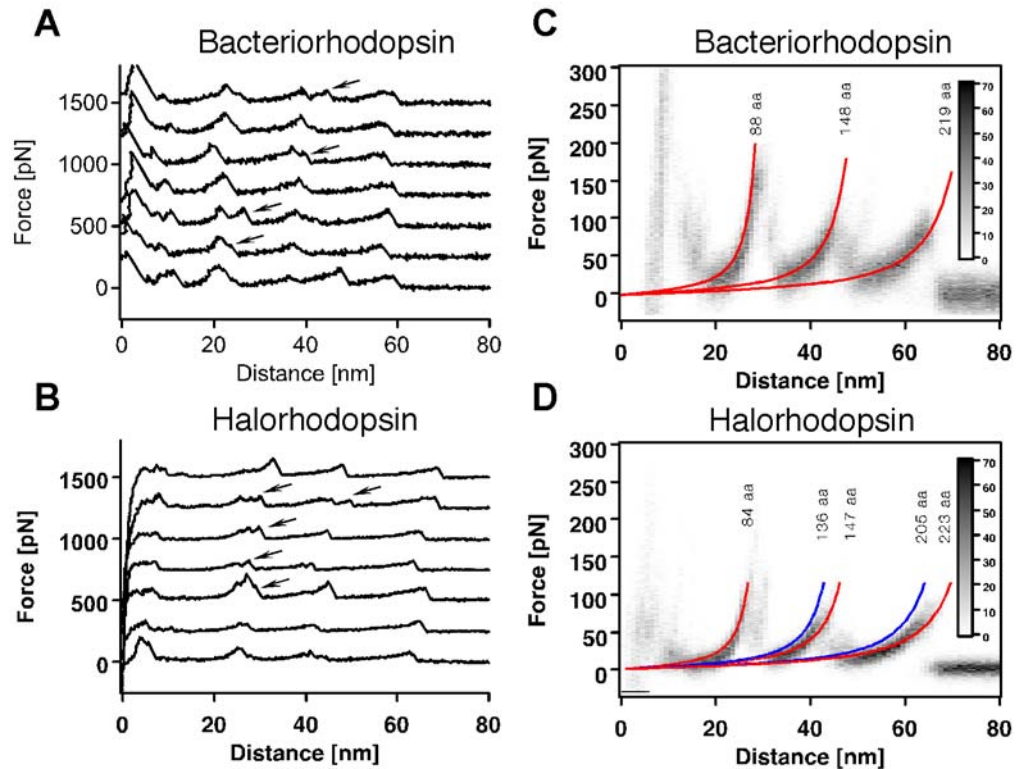


Figure 4.2. Comparison of BR and HR force-unfolding spectra. A) Representative force curves of BR unfolding. B) Representative force curves of HR unfolding. C) Superimposition of force curves of BR unfolding. D) Superimposition of force curves of HR unfolding.

To make sure that the selected force curves belonged to the C-terminus unfolding, WLC curves assuming pairwise unfolding of HR by pulling its C- and N-terminus were simulated. For C-terminal unfolding, WLC-simulated stretched polypeptides have 83 aa, 147 aa and 223 aa. These curves matched the density of the force curves obtained (Fig. 4.2D, red lines). On the contrary, N-terminal simulated pairwise (WLC simulations at 84 aa, 136 aa and 205 aa) unfolding did not match the density (Fig. 4.2D, blue lines). This approach was recently challenged by Kessler *et al.* (Kessler and Gaub, 2006). In his study of BR N-terminal pulling he found a barrier at 223 aa. This barrier would occur when the protein had already been extracted when pulled by the N-terminus (the length is almost equal to the length of the protein). Further experiments to confirm or discard this possibility are currently being performed.

At the same time, each individual trace showed different shoulder peaks next to the three main peaks, called here side peaks (Fig. 4.2A-B arrows). The WLC model was fitted to every main and side peak of force curves (Fig. 4.3).

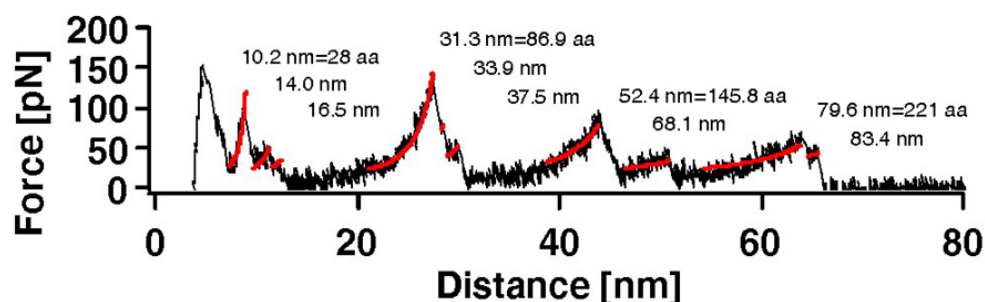


Figure 4.3. Fitting of WLC model to the force curves. All force curves from BR and HR were fitted with the WLC model. A representative curve of HR is shown with its respective WLC-fit derived lengths. The main peaks of this curve were re-scaled to length in aa.

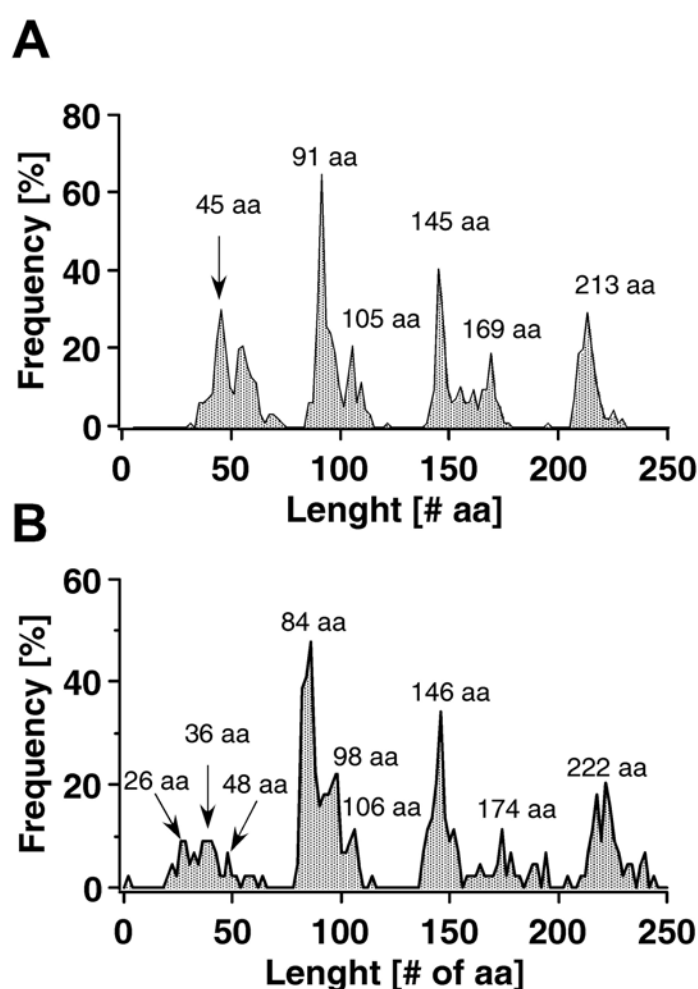


Figure 4.4. WLC-derived length histogram. The WLC model was fitted to each individual peak from each force curve. The length obtained in nm was transformed into aa assuming a length of 0.36 nm/aa. A histogram of the lengths is shown for A) BR and B) HR and the main or side visible peaks are marked.

The lengths derived from the fits were re-scaled to aa assuming a length of 0.36 nm/aa. A histogram of the WLC-derived lengths, show again the

similarities between BR and HR (Fig. 4.4A-B). Additionally, some of the side peaks are also distinguishable in this plot. For the case of BR (Fig. 4.4B), side peaks at 45 aa, 105 aa, and 169 aa are visible. Those peaks were previously assigned to the unfolding of loop F-G, helix D and the beta sheet formed by loop B-C, respectively (Muller et al., 2002c). Comparing the histograms show that for every described peak in BR a corresponding one could be found in HR unfolding. The histogram for HR unfolding show side peaks at 26 aa, 36 aa, 48 aa, 98 aa, 106 aa, 174 aa. Side peaks of HR, were analyzed individually (see below).

4.3.3. Unfolding pathways of HR

To compare the unfolding pathways of HR and BR the appearance of each peak in HR spectra was analyzed individually (Fig. 4.5). To locate the structural segments that unfold together, the lengths derived from the WLC fit (see example in Fig. 4.5A), were correlated to the structure of HR (PDB code 1E12). Peaks detected at distances below 5 nm showed a strong variation, which reflected the different attachment sites of the molecule to the tip (Muller et al., 2002c). Beyond the first 5 nm, three characteristic peaks were found (Fig. 4.5C). The first peak with an average length of ~26 aa corresponds to the stretching of the first half of helix G. As previously proposed for BR (Muller et al., 2002c), helix G unfolds in two steps probably because the retinal is covalently bounded to it. The next peak was then found after ~35 aa. This peak co-localizes to the GF loop. The peak at ~47 aa probably described the unfolding of helix F. In the separation distance between 15 and 35 nm four different force peaks were observed at average lengths of ~84 aa, ~88 aa, ~97 aa and ~103 aa (Fig. 4.5D). The 84 aa peak was established by helix E. In some cases, a short cytoplasmic segment of this helix unfolded releasing only 6 aa, which was detected at the ~88 aa peak. Both peaks of ~88 aa and ~97 aa were assigned to the unfolding of consecutive short segments of helix E, each one being ≈ 11 aa long (Table 1). At an average length of ~103 aa the rest of helix E unfolded together with helix D. Between 35 nm and 55 nm, three peaks were found (Fig. 4.5E). The peak at ~147 aa represented unfolding of helix C, while at ~160 aa the long B-C loop unfolded which forms a β -sheet in its native conformation. After this, the stretched polypeptide summed up to ~180 aa. This

peak describes unfolding of helix B. Finally, in the last part of the force trace (Fig. 4.5F), helix B was stretched then to ~223 aa and helix A unfolded in two steps described by the peaks at ~223 aa and ~237 aa. The probabilities of appearance for all peaks described above, when they represent the unfolding of single structural elements, are given in Table 1.

4.4. Discussion

4.4.1. Halorhodopsin imaging

Two-dimensional HR crystals were imaged previously in buffer solution using AFM (Persike et al., 2001). An assignment of the extracellular and cytoplasmic surface was made assuming that the largest loop (loop B-C, which includes a β -sheet) of HR would be represented by the highest protrusion of the AFM topograph (Denoted by the four single protrusions in the center of Fig 1C). The spatial resolution of our high-resolution topographs was slightly better than that previously published (Persike et al., 2001). Nevertheless, without further elucidation, it appears difficult to confirm or discard the assignment of sidedness. Both possibilities of the sidedness assignment are depicted in Fig. 4.1C, where the outline of neighboring HR tetramers (Havelka et al., 1993) was superimposed to the correlation averaged topograph.

4.4.2. Unfolding pathways of HR resemble those of BR

In previous studies, SMFS has been used to characterize unfolding events of BR (Oesterhelt et al., 2000). In these studies, the force vs. distance spectrum characterized the unfolding pathway of each individual molecule. The probability for each pathway to occur depended on physiologically relevant parameters like pH, electrolytes, and temperature (Janovjak et al., 2003; Muller et al., 2002c). Experimental conditions, like the pulling speed, affected the probability of the pathways as well. (Janovjak et al., 2004). It is interesting to note that the variation of none of the conditions mentioned above promoted the appearance of new unfolding pathways in BR. This observation suggests that the additional unfolding barrier within helix E could be intrinsic to HR.

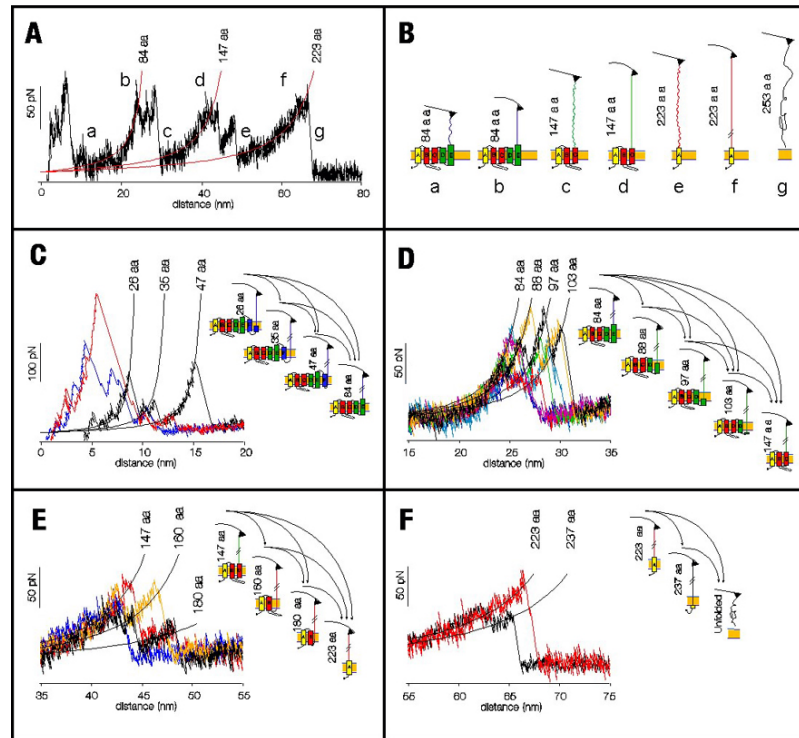


Figure 4.5. Unfolding pathways of HR. A) Representative force spectra of HR unfolding. For simplicity only three peaks were fitted and correlated to the structure-topology (B). B) Schematic drawing of HR showing single molecule unfolding processes from fits derived in A. The first force peaks detected within a separation distance between 0 and 15 nm indicated the unfolding of helices F and G, and of loops F-G and E-F. After unfolding two transmembrane helices (a), the number of unfolded aa was increased to 84 aa and the cantilever relaxed. Further separation of tip and sample stretched the polypeptide (b), thereby pulling on helix E. At a certain pulling force, the mechanical stability of helices E and D was overcome and they unfolded together with loops D-E and C-D (c). A polypeptide chain of 147 aa was now stretched (d). Helices B and C and loops B-C and A-B unfolded, thereby relaxing the cantilever (e). By further separating tip and HR, the cantilever pulled on helix A (f), until it unfolded and the polypeptide was completely extracted from the membrane (g). C-F) Unfolding events of individual secondary structures in HR. C) The peak at ~26 aa indicated the unfolding of the cytoplasmic half of helix G up to the covalently bound retinal. The peak at ~35 aa indicated the complete unfolding of helix G. At ~47 aa, helix G and the loop connecting helices G and F unfold and the force pulled directly on helix F until this helix unfolded together with loop E-F. D) The side peaks of the second main peak indicated the stepwise unfolding of helices E and D and loop D-E. The peak at ~84 aa indicated the unfolding of the first part of helix E (helix Ea). The remaining side peaks (~88 aa, ~97 aa) represented the stepwise unfolding of helix E, the peak of ~103 aa represents the unfolding of the rest of helix E and helix D. E, The third main peak and its side peaks indicated the stepwise unfolding of helix C (at ~147 aa), of loop B-C (at ~160 aa) and of helix B (at 180 aa). F) Finally, unfolding of helix A was represented by the last main peak at ~223 aa, while the following side peak (~237 aa) occurred probably due to the pulling of the N-terminal end through the membrane.

Almost all unfolding barriers and pathways observed for HR have been previously observed for BR (Janovjak et al., 2003; Muller et al., 2002c). To trace the origin of this phenomenon, structural segments establishing their own stability were co-localized to the primary and secondary structures of both proteins (Fig. 4.6, colors). It became evident that these stabilizing segments of BR and HR were located at almost the same structural positions. Apparently, the aa composition and their distribution within these segments showed no specific pattern. Thus, it may be assumed that in the case of HR and BR, different aa sequences form similar structural segments that establish very similar energetic stability. Additionally, the unfolding forces (Table 1) of these structural elements in HR do not differ significantly from those measured for BR (Janovjak et al., 2004).

4.4.3. Collective interactions of aa establish stable structural segments

At this point it appears difficult to conclude by which mechanism the aa establish an energetic barrier against unfolding. Analyzing the residues which compose the structurally stabilizing segments or domains in HR and BR showed no common patterns. Thus, non-specific interactions may dominate this process. This observation supports the idea that, *in vivo*, transmembrane helices would simply partition into the bilayer due to its overall hydrophobicity while passing through the translocon without any signal (White and von Heijne, 2004). Furthermore, after aligning sequences of BR and HR (Fig. 4.6) it became clear that the identical aa were randomly distributed within stabilizing structural segments. Additionally, no differences between the aliphatic index and the hydrophobicity index (GRAVY) were observed among stable structural elements of BR and HR.

Overcoming the critical force initiates spontaneous unfolding of the structural segment. Apparently, there is no rule on how many aa are required to build up such a stabilizing structural segment within the protein. The distance between two consecutive stabilizing segments allows estimating the maximum number of aa which establishes the first segment. From these it can be concluded that the smallest segments in HR contained only ~6 aa while the largest ones were comprised by more than 32 aa (Table 1). Structural segments establishing a cooperative unfolding barrier do not necessarily

correlate to one secondary structure element of the protein. For example, the force spectra show unfolding of a transmembrane helix together with a polypeptide loop, or of two helices establishing a cooperative unfolding barrier. The forces required to unfold a small segment are equally large as the ones necessary to unfold larger segments. This suggests some hidden complexity in the force unfolding process (Table 1).

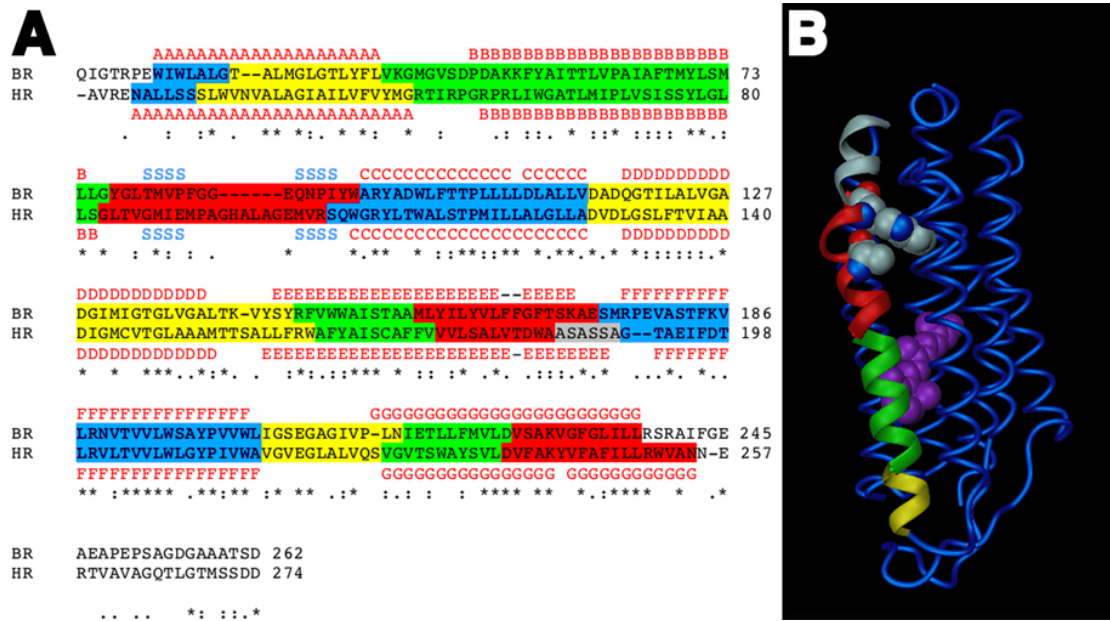


Figure 4.6. Sequence alignment of BR and HR. A) Each color indicates one segment structural of the protein that unfolded collectively. The name of each helix (A-G) is indicated on top (BR) and bottom (HR) of the sequence. S denotes the β -sheet established by the B-C loop. From this representation it becomes clear that the structural segments that established a barrier against unfolding were conserved in HR and BR. One exception, however, was found for the zone colored gray in helix E. Here, an additional unfolding barrier was present in HR. B) Helices E and Ea in the HR structure were represented as cartoon; the colors in helix E correspond to the different segments that unfolded cooperatively and correlated to the ones in panel A. Both Ala 178 and Trp 183 (colored as CPK) were represented as cpk spheres to highlight the Pi-bulk interaction that structurally and energetically disrupted helix E.

In other experiments, Faham *et al.* mutated a proline (P50A) located at the kink of BR helix B (Faham *et al.*, 2004). Since neither the structure nor the stability of the membrane protein changed significantly, it was concluded that the bend of this helix results from cumulative effects of adjacent residues. These results also strongly argue that aa of folded polypeptides interact collectively to establish stable structural modules or segments. It is furthermore assumed, that during evolution some aa replaced residues of the peptides and took over structural properties, which were previously induced by a key residue

(Faham et al., 2004). Our measurements showed that such segments establish sufficient interactions to form stable entities.

Segment unfolded	Force \pm SD (pN)	Length \pm SD (aa)	P(single) \pm SD (%)
Helix Ea*	93 \pm 23	6 \pm 2	79.5 \pm 6.0
Helix E (1 st part)*	120 \pm 45	11 \pm 4	63.3 \pm 7.3
Helix E (2 nd part)*	91 \pm 36	17 \pm 5	22.7 \pm 6.3
Helix D	79 \pm 26	32 \pm 5	36.3 \pm 7.3
Helix C*	73 \pm 14	24 \pm 10	43.2 \pm 7.5
Helix B*	71 \pm 35	30 \pm 15	52.2 \pm 7.5
Helix A	50 \pm 31	14 \pm 6	29.5 \pm 6.9
Loop B-C*	77 \pm 11	22 \pm 12	22.7 \pm 6.3

Table 1. Stability and length of single structural elements. P(single) denotes the probability of that structural element to unfold alone in a single event. *For these values it had to be considered that the elements building up the unfolding barrier was embedded in the membrane during stretching (see section 4.2.4).

4.4.4. Unfolding of Helix E

One apparent difference between the unfolding pathways of BR and HR was found in case of helix E (Fig. 4.3D). Unfolding of helices E and D in BR can occur via four different pathways, exhibiting peaks at positions ~88 aa, ~94 aa and ~105 aa, which denote the positions of three unfolding barriers (Janovjak et al., 2003). In the case of HR, helix E exhibited one additional unfolding barrier. All four barriers were fitted to segments of ~84 aa, ~88 aa, ~97 aa and ~103 aa. Together with all other unfolding intermediates it became clear that helix E exhibited a high probability to unfold in multiple steps. Seven unfolding pathways were found for helices D & E in HR, which represent the combination of all unfolding barriers (Fig. 4.5D). The additional unfolding barrier of helix E may find its origin in a Pi-bulk interaction (also known as CH/Pi)(Kobayashi and Saigo, 2005) which is located between Ala 178 and Trp 183 (Fig. 4.6) and disrupts helix E (Kolbe et al., 2000) (see remark 650 in HR pdb file, code 1E12). This interaction is not present in BR. The disruption stabilizes a kink that splits helix E into two structurally different segments (Fig. 4.6B), helix E and helix Ea. The force spectroscopy data gives experimental evidence that both helix E and helix Ea are structurally stabilized by intrinsic molecular interactions, which

allow each structural segment to act independently. The probability that helix Ea unfolds by itself was 79.5% (Table 1). In other structural papers it was further assumed that the region where the Pi-bulk interaction (Ala 178 - Trp 183) is located can act as hinge (Essen, 2002; Subramaniam and Henderson, 2000), supporting the idea of the structural independence of helical segments E and Ea. Furthermore, *in vivo* folding experiments of bacterioopsin (BR without retinal) could not resolve the insertion of Helices D and E (Dale et al., 2000), which shows that these helices show a different behavior from the rest.

4.4.5. Hierarchical unfolding within the “three stage” model

The two-stage model postulates that membrane protein folding includes a primary stage in which independent, stable helices are established across the membrane lipid bilayer. This process is followed by a second stage in which the helices interact with each other forming higher ordered structures (Engelman et al., 2003; Popot and Engelman, 1990). In a recent review, the question “what happens beyond” the two-stage model was raised and the third stage of membrane folding was introduced (Engelman et al., 2003; White, 2003). In this third stage, the loops condense the inserted secondary structure elements into the functional protein. Here, the effect of intrinsic molecular interactions that established unfolding barriers located within the membrane protein were detected. It was observed, that single helices, polypeptide loops or helical pairs can form structurally stable segments. Apparently, amino acids within these segments act collectively and unfold cooperatively. Although some structural segments were smaller (Helix Ea) than single secondary structure elements of HR, they maintained the ability to form their own energetic barriers against unfolding. Intermediate steps within the two-stage folding model may be established by this kind of interactions. However, it was observed that some structural segments could bridge two secondary structures. For example, the extracellular half of helix G and the loop connecting helices G and F established one stabilizing segment (Fig. 4.5C, 35 aa peak). It could be speculated, that this process may represent an important step of a folding intermediate bringing the secondary elements, which have been inserted into the membrane bilayer, close together into the functional arrangement. This observation would strongly support the recently suggested third stage of folding in which loops pull

transmembrane helices together into the functional conformation (Engelman et al., 2003; White, 2003).

4.5. Conclusions

One of the most remarkable results of this study is that two proteins that have ~ 30 % sequence identity and almost identical 3D structures, unfold taking almost identical pathways. This finding suggests that different amino acid compositions can establish structurally indistinguishable stabilizing segments. It is concluded that these segments may rather result from comprehensive interactions of all amino acids within a structural region than from specific interactions. Both proteins unfolded via equivalent intermediate steps independently of their amino acid sequence. The results support the view that secondary structure, to which the peptide backbone contributes significantly could play a major role in stabilizing membrane proteins. A subtle but important difference was found in the unfolding pathway of helix E of HR. Here, a Pi-bulk interaction locally disrupts helix E into two structurally and energetically different parts. This additional unfolding barrier increases the combinatorial space of possible unfolding pathways. In future it may be investigated whether this structural and energetic division of helix E is functionally significant to HR during the photocycle.

A thorough analysis of the structural segments that stabilize the membrane protein structures of HR and BR allows supporting the recently presented three-stage model of membrane protein folding. These and previous force-spectroscopy experiments showed that secondary structures can establish sufficient molecular interactions to act as independently stable units. For example it was shown, that polypeptide loops connecting transmembrane α -helices could have an intrinsic stability as well. Additionally, it was observed sometimes that two different structural elements unfolded together (pairwise unfolding). This suggests that there must be molecular interactions that keep these structures together, as well. Here, for the first time, experimental evidence in support of the postulated third stage of membrane protein folding is presented, in which independently stable structural units are brought together to form the functional protein.

4.6. Future Perspectives

4.6.1. SRII unfolding resembles that of BR and HR

To gather further information on the folding processes of archaeal rhodopsin, the question of whether SRII also unfolds in the same way as BR and HR was addressed. For that purpose, force-unfolding experiments for SRII without the transducer were performed. Preliminary data show that individual curves contain three main peaks, just as for BR and HR (Fig. 4.7A). The superimposition of the force curves into a density plot (Fig 4.7B) showed the resemblance of the main features with those of BR and HR unfolding traces (compare to Figure 4.2C-D). The results show that just as HR, SRII seems to establish the same unfolding barriers as BR. This observation supports the argumentation that no specific sequence is needed to establish unfolding barriers in structurally similar transmembrane proteins. Further analysis of the individual force traces will be performed to confirm the appearance of intrinsic segments that establish barriers against unfolding.

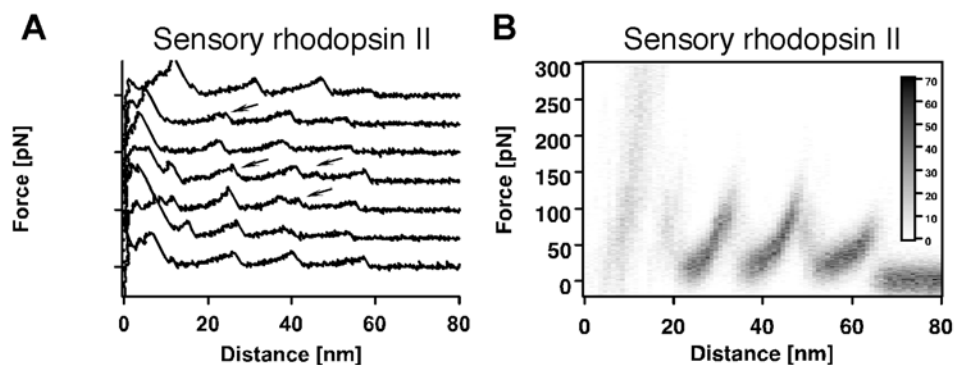


Figure 4.7. Force-unfolding spectra of SRII. A) Representative force curves of SR unfolding. B) Superimposition of force curves of SRII unfolding. Arrows indicate differences in individual traces.

5.0 General Conclusions

5.1. Structural complexity of living organisms and self-organization

Biological systems are recognized to be complex. Moreover, it is established that they consist of subsystems (levels) hierarchically arranged in a nested manner. From a general point of view, one can discuss about functional and structural levels (Heylighen, 2001). In the case of a biological system, e.g. a cell, the hierarchical assembly of molecules determines its structural complexity and the interaction between them determine its functional levels.

Many structures formed by bio-macromolecules present self-organizing or self-assembly properties at several levels of complexity. As self-organization is understood the steady state assembly and disassembly of components into transit structures. Self-assembly is simply the process by which components form stable structures through weak interactions (Kurakin, 2005; Whitesides and Boncheva, 2002). Therefore, the structural complexity at each level is ultimately determined by self-assembly processes.

For example, at the intracellular level, cytoskeleton dynamics are determined by the self-organizing properties of actin filaments and microtubules (Kurakin, 2005). Interactions with other proteins modulate the self-organization properties of these filaments, which regulate cell shape and motility. In another example, differences in the physico-chemical properties of lipids result in the self-organization of domains in biological membranes (Kahya, 2006). Clustering of the domains through the interaction with proteins could confine in the same space signaling molecules and ultimately affect cellular functions (Rajendran and Simons, 2005).

At another level of complexity, components of the extracellular matrix also present self-assembly properties. Fibronectin, a component of the ECM, forms insoluble fibrils after being secreted by connective tissue cells. Recent data indicate that mechanical stretching exerted by the cells to fibronectin exposes cryptic self-association sites in it, resulting in fibrillogenesis (Vogel et al., 2001). Collagen, another major component of the ECM, undergoes self-assembly. In section 2.0, this process was observed at high resolution for the first time using time-lapse AFM. The assembly comprises an artificial collagen type I matrix. It is proposed that collagen self-healing properties observed in

those matrices (section 2.4.5) contribute to wound healing (Grinnell, 2003). Furthermore, a two-step mechanism for the formation of fibrils was proposed. In the first step collagen molecules associate loosely, in the second step they collapse to form a microfibril (section 2.4.3). The mechanism implies that microfibrils could be the building blocks of fibrillogenesis. In tissues like cornea, the modulation of the self-assembly of collagen molecules into fibrils is controlled very precisely (Holmes and Kadler, 2005). It is supposed that the control of the fibril width depends on proteoglycans by a not so clear mechanism (Graham et al., 2000). Therefore, the assay developed to visualize collagen self-assembly into fibrils (section 2.0) could also be used to observe how other proteins regulate the process.

Protein folding remains at the intra-molecular level in the hierarchy of self-organizing processes. In pioneer experiments, Anfinsen showed that the protein ribonuclease could refold spontaneously *in vitro* (Haber and Anfinsen, 1961). The result implies that all the information is encoded in the protein itself. Hydrogen bonds, ion bridges and van der Waals interactions are the driving force. Currently, the debate is centered in whether folding is driven by backbone or side-chain interactions (Rose et al., 2006).

On the other hand, AFM unfolding experiments on membrane proteins have recently gotten attention since: 1) it was proved that membrane proteins re-fold after being force-unfolded (Kedrov et al., 2004; Kessler et al., 2006) and 2) it was shown that ATP dependent proteases extract mechanically membrane proteins from mitochondrial and ER membranes *in vivo* (Leonhard et al., 2000; Ye et al., 2001). In section 4.0, it was demonstrated that two proteins with only 30% sequence identity unfold by exactly the same mechanism. The results described in section 4.0 support the view that backbone contributions, *i.e.* secondary structure, could participate hierarchically (section 4.4.5) in the (un)folding process. How these hierarchies affect the folding mechanism in the context of the translocon it is to be determined by re-folding or *in vivo* experiments.

At the intermolecular level, some membrane proteins form multimers and interact with lipids to achieve their native structure. Clearly, the anisotropic environment of the bilayer imposes geometrical restrictions to how membrane proteins structure/function is studied. In particular, into how its structure is

determined. 2D and 3D crystals of membrane proteins embedded in lipids are difficult to obtain, but atomic resolutions is attainable. In section 3.0, the self-assembly properties of a thiolipid were used to create an interface to study membrane proteins with AFM. The results described open the possibility to obtain structural details of membrane at a resolution similar to the one obtained with 2D crystals.

Biological systems exist as a result of processes that generate complex functional structures by self-assembly (Whitesides and Boncheva, 2002). In this work, we used AFM to characterize self-assembly processes. Besides, SMFS was used to characterize interactions stabilizing/driving membrane protein self-assembly into membranes. Ultimately, mimicking natural self-assembly processes allowed studying macromolecular structures.

Abbreviations and symbols

Abbreviations

2D	Two-dimensional
3D	Three-dimensional
Å	Angstrom
aa	Amino acid
AFM	Atomic force microscopy
BR	Bacteriorhodopsin
CM-AFM	Contact mode AFM
Cryo-EM	Cryo-electron microscopy
ECM	Extracellular matrix
EM	Electron microscopy
FJC	Freely-Jointed-Chain
FnIII	Fibronectin domain III
HR	Halorhodopsin
I27	Titin immunoglobulin domain 27
Ig	Immunoglobulin
kcal	Kilo-calorie
kDa	Kilo-dalton
kHz	Kilo-Hertz
min	minute
N	Protein native state
NMR	Nuclear magnetic resonance
OG	octylglucopyranoside
OmpF	Outer membrane protein F
PDB	Protein Data Bank
RMS	Root mean square
s	Seconds
SAM	Self-assembled monolayer
SD	Standard deviation
SEM	Standard error of the mean
SMFS	Single molecule force spectroscopy
SNOM	Scanning near-field optical microscope

SPM	Scanning probe microscopy
SRP	Signal recognition particle
SRI	Sensory rhodopsin I
SRII	Sensory rhodopsin II
STM	Scanning tunneling microscopy
TEM	Transmission electron microscopy
TM-AFM	Tapping mode AFM
TS-gold	Template-stripped gold
U	Protein unfolded state
WLC	Worm-Like-Chain

Symbols

σ	Surface charge density [C/m ²]
ε_0	Vacuum dielectric constant
ε_e	Solvent dielectric constant
b	Monomer length [m]
e_c	Ion concentration [C/L]
E_{TS}	Activation energy [kcal/mol]
F	Force [N]
f^*	Most probable rupture force [N]
F_{el}	Electrostatic forces [N]
F_{vdW}	Van der Waals forces [N]
H_a	Hamaker constant [J]
k	Cantilever spring constant [N/m]
k_0	Unfolding rate [s ⁻¹]
k_b	Boltzman constant (1.38*10 ⁻²³ J/K)
k_U	Unfolding rate under force [s ⁻¹]
k_u	Natural off-rate of a bond
L	Langevin function
L	Polymer contour length [m]
l_p	Persistence length [m]
pI	Isoelectric point
T	Temperature [K]

z_b	Projected potential barrier width [m]
z_{TS}	Potential barrier width [m]
Δz	Cantilever's deflection

Acknowledgments

Daniel, thanks for letting me work in such a great place and for teaching me many things. I seriously learned a lot from you.

To my TAC committee: **Joe Howard** and **Michael Brand** for putting up with my TAC meetings.

To my collaborators,

Jeremy Lakey, thanks for giving me a different view of science and for all the hard work.

Mira Tula, thanks for your patience and work, I also learned a lot from you.

To the Müller lab:

Ada, for being a true inspiring story.

Alexej, thanks for teaching many things, but mainly for being so real.

Angela, thanks for all the hard work and for your patience.

Anna, Ya po', gracias por ser la alemana mas buena onda que he conocido y por enseñarme tantas cosas.

Barbara, thanks for all your help.

Christian, thanks for getting me out of trouble many times. Keep on being so precise. You rock!

Clemens, thanks for watching over my shoulder many times and for being a good friend.

Jonne, thanks for all the good scientific discussion, which is one of our favorite hobbies. It is incredible the amount of things that I've learned from you.

Pierre, thanks for teaching me how a scientist solves problems.

Susanne, thanks for teaching me how to enjoy what one does.

Tanuj, thanks for being a good friend and for teaching me how to come back and win the game.

The rest of the Müller lab: **Dirk, Harald, Isabel, Jens, Michael, Natalya**. Thanks for providing an inspiring work environment.

To my flatmates, **Jennifer** and **Christer**, for the hard work (of living with me).

To my friends in Dresden: **Alvaro, Amani, Daniela, Fernando, Fugarte, Jakob, Joao, Lara, Marta, Nicola, Robin, Susi, Thomas, Vinciane, Violeta**. Thanks for making my life happier here in good and in bad times.

To **Andrea**, for bringing love and happiness to my life.

List of publications

1. Perez-Armendariz, E. M., Lamoyi, E., Mason, J. I., **Cisneros-Armas, D.**, Luu-The, V. & Bravo Moreno, J. F. (2001). Developmental regulation of connexin 43 expression in fetal mouse testicular cells. *Anat Rec* 264, 237-46.
2. **Cisneros, D. A.**, Montero-Moran, G. M., Lara-Gonzalez, S. & Calcagno, M. L. (2004). Inversion of the allosteric response of *Escherichia coli* glucosamine-6-P deaminase to N-acetylglucosamine 6-P, by single amino acid replacements. *Arch Biochem Biophys* 421, 77-84.
3. **Cisneros, D. A.**, Oesterhelt, D. & Muller, D. J. (2005). Probing origins of molecular interactions stabilizing the membrane proteins halorhodopsin and bacteriorhodopsin. *Structure* 13, 235-42.
Commented in: Chin G.J. 2005. Editor's Choice "Deconstructing membrane proteins". *Science* 307, 1172
4. Poole, K., Khairy, K., Friedrichs, J., Franz, C., **Cisneros, D. A.**, Howard, J. & Mueller, D. (2005). Molecular-scale topographic cues induce the orientation and directional movement of fibroblasts on two-dimensional collagen surfaces. *J Mol Biol* 349, 380-6.
5. **Cisneros, D. A.**, Hung, C., Franz, C. M. & Muller, D. J. (2006). Observing growth steps of collagen self-assembly by time-lapse high-resolution atomic force microscopy. *J Struct Biol* 154, 232-45.
6. **Cisneros, D. A.**, Muller, D. J., Daud, S. M. & Lakey, J. H. (2006). An approach to prepare membrane proteins for single-molecule imaging. *Angew Chem Int Ed Engl* 45, 3252-6.
7. Janovjak, H., Kedrov, A., **Cisneros, D. A.**, Sapra, K. T., Struckmeier, J. & Muller, D. J. (2006). Imaging and detecting molecular interactions of single transmembrane proteins. *Neurobiol Aging* 27, 546-61.
8. Preiner, J., Janovjak, H., Knaus, H., **Cisneros, D.A.**, Kedrov, A., Kienberger, F., Muller, D. J. & Hinterdorfer, P. (2006). Insertion and folding energy of membrane proteins derived from single-molecule force measurements. *Submitted to Biophys J*.
9. Taubenberger, A., **Cisneros, D. A.**, Friedrichs, J., Puech, P. H., Muller, D. J. & Franz, C. (2006). Revealing early steps of $\alpha 2\beta 1$ integrin-mediated adhesion to collagen type I using single-cell force spectroscopy. *Mol Biol Cell (In press)*.
10. **Cisneros, D.A.**, Friedrichs, J., Taubenberger, A. and Muller, D.J. (2006) Development of Nanoscopic collagen matrices for biological and biotechnological applications. *SMALL (In press)*.

Bibliography

- Abramoff, M.D., Magelhaes, P.J. and Ram, S.J. (2004) Image processing with ImageJ. *Biophotonics Int*, **11**, 36-42.
- Agarwal, G., Kovac, L., Radziejewski, C. and Samuelsson, S.J. (2002) Binding of discoidin domain receptor 2 to collagen I: An atomic force microscopy investigation. *Biochemistry*, **41**, 11091-11098.
- Albers, S.V., Szabo, Z. and Driessen, A.J. (2006) Protein secretion in the Archaea: multiple paths towards a unique cell surface. *Nat Rev Microbiol*, **4**, 537-547.
- Allen, D.B. and Goldberg, B.D. (1992) Stimulation of collagen synthesis and linear growth by growth hormone in glucocorticoid-treated children. *Pediatrics*, **89**, 416-421.
- Ando, T., Kodera, N., Naito, Y., Kinoshita, T., Furuta, K. and Toyoshima, Y.Y. (2003) A high-speed atomic force microscope for studying biological macromolecules in action. *Chemphyschem*, **4**, 1196-1202.
- Ando, T., Kodera, N., Takai, E., Maruyama, D., Saito, K. and Toda, A. (2001) A high-speed atomic force microscope for studying biological macromolecules. *Proc Natl Acad Sci U S A*, **98**, 12468-12472.
- Annunen, S., Paassilta, P., Lohiniva, J., Perala, M., Pihlajamaa, T., Karppinen, J., Tervonen, O., Kroger, H., Lahde, S., Vanharanta, H., Ryhanen, L., Goring, H.H., Ott, J., Prockop, D.J. and Ala-Kokko, L. (1999) An allele of COL9A2 associated with intervertebral disc disease. *Science*, **285**, 409-412.
- Bain, C.D. and Whitesides, G.M. (1988) Molecular-Level Control over Surface Order in Self-Assembled Monolayer Films of Thiols on Gold. *Science*, **240**, 62-63.
- Barret, S.D. (2004) Image SXM, <http://www.ImageSXM.org.uk>.
- Bernengo, J.C., Herbage, D., Marion, C. and Roux, B. (1978) Intermolecular interaction studies on native and enzyme-treated acid-soluble collagen. *Biochim Biophys Acta*, **532**, 305-314.
- Bigi, A., Gandolfi, M., Roveri, N. and Valdre, G. (1997) In vitro calcified tendon collagen: An atomic force and scanning electron microscopy investigation. *Biomaterials*, **18**, 657-665.
- Binnig, G., Quate, C.F. and Gerber, C. (1986) Atomic force microscope. *Physical Review Letters*, **56**, 930-933.
- Binnig, G. and Rohrer, H. (1983) Scanning tunneling microscopy. *Surface Science*, **126**, 236-244.

- Binnig, G. and Rohrer, H. (1999) In touch with atoms. *Reviews of Modern Physics*, **71**, S324-S330.
- Brandl, F., Sommer, F. and Goepferich, A. (2007) Rational design of hydrogels for tissue engineering: impact of physical factors on cell behavior. *Biomaterials*, **28**, 134-146.
- Bustamante, C., Marko, J.F., Siggia, E.D. and Smith, S. (1994) Entropic elasticity of lambda-phage DNA. *Science*, **265**, 1599-1600.
- Butt, H.J., Jaschke, M. and Ducker, W. (1995) Measuring Surface Forces in Aqueous-Electrolyte Solution with the Atomic-Force Microscope. *Bioelectrochemistry and Bioenergetics*, **38**, 191-201.
- Carrion-Vazquez, M., Oberhauser, A.F., Fisher, T.E., Marszalek, P.E., Li, H. and Fernandez, J.M. (2000) Mechanical design of proteins studied by single-molecule force spectroscopy and protein engineering. *Prog Biophys Mol Biol*, **74**, 63-91.
- Carrion-Vazquez, M., Oberhauser, A.F., Fowler, S.B., Marszalek, P.E., Broedel, S.E., Clarke, J. and Fernandez, J.M. (1999) Mechanical and chemical unfolding of a single protein: a comparison. *Proc Natl Acad Sci U S A*, **96**, 3694-3699.
- Cavalcanti-Adam, E.A., Micoulet, A., Blummel, J., Auernheimer, J., Kessler, H. and Spatz, J.P. (2006) Lateral spacing of integrin ligands influences cell spreading and focal adhesion assembly. *Eur J Cell Biol*, **85**, 219-224.
- Chapman, J.A., Tzaphlidou, M., Meek, K.M. and Kadler, K.E. (1990) The collagen fibril--a model system for studying the staining and fixation of a protein. *Electron Microsc Rev*, **3**, 143-182.
- Chen, C.H. and Hansma, H.G. (2000) Basement membrane macromolecules: Insights from atomic force microscopy. *J. Struct. Biol.*, **131**, 44-55.
- Chernoff, E.A.G. and Chernoff, D.A. (1992) Atomic force microscope images of collagen-fibers. *J. Vac. Sci. Tech.*, **10**, 596-599.
- Christiansen, D.L., Huang, E.K. and Silver, F.H. (2000) Assembly of type I collagen: fusion of fibril subunits and the influence of fibril diameter on mechanical properties. *Matrix Biol*, **19**, 409-420.
- Cisneros, D.A., Hung, C., Franz, C.M. and Muller, D.J. (2006) Observing growth steps of collagen self-assembly by time-lapse high-resolution atomic force microscopy. *J Struct Biol*, **154**, 232-245.
- Cowan, S.W., Schirmer, T., Rummel, G., Steiert, M., Ghosh, R., Paupit, R.A., Jansonius, J.N. and Rosenbush, J.P. (1992a) Crystal structures explain functional properties of two *E. coli* porins. *Nature*, **358**, 727-733.
- Cowan, S.W., Schirmer, T., Rummel, G., Steiert, M., Ghosh, R., Pauptit, R.A., Jansonius, J.N. and Rosenbusch, J.P. (1992b) Crystal structures explain functional properties of two *E. coli* porins. *Nature*, **358**, 727-733.

- Dale, H., Angevine, C.M. and Krebs, M.P. (2000) Ordered membrane insertion of an archaeal opsin in vivo. *Proc Natl Acad Sci U S A*, **97**, 7847-7852.
- Demers, L.M., Ginger, D.S., Park, S.J., Li, Z., Chung, S.W. and Mirkin, C.A. (2002) Direct patterning of modified oligonucleotides on metals and insulators by dip-pen nanolithography. *Science*, **296**, 1836-1838.
- Dill, K.A. and Chan, H.S. (1997) From Levinthal to pathways to funnels. *Nat Struct Biol*, **4**, 10-19.
- Engel, A. and Müller, D.J. (2000) Observing single biomolecules at work with the atomic force microscope. *Nat. Struct. Biol.*, **7**, 715-718.
- Engel, J. and Prockop, D.J. (1998) Does bound water contribute to the stability of collagen? *Matrix Biol*, **17**, 679-680.
- Engelman, D.M., Chen, Y., Chin, C.N., Curran, A.R., Dixon, A.M., Dupuy, A.D., Lee, A.S., Lehnert, U., Matthews, E.E., Reshetnyak, Y.K., Senes, A. and Popot, J.L. (2003) Membrane protein folding: beyond the two stage model. *FEBS Lett*, **555**, 122-125.
- Essen, L., Siegert, R., Lehmann, W.D. and Oesterhelt, D. (1998) Lipid patches in membrane protein oligomers: crystal structure of the bacteriorhodopsin-lipid complex. *Proc Natl Acad Sci U S A*, **95**, 11673-11678.
- Essen, L.O. (2002) Halorhodopsin: light-driven ion pumping made simple? *Curr Opin Struct Biol*, **12**, 516-522.
- Evans, E. (2001) Probing the relation between force--lifetime--and chemistry in single molecular bonds. *Annu Rev Biophys Biomol Struct*, **30**, 105-128.
- Evans, E. and Williams, P. (2002) Dynamic force spectroscopy: 1. Single bonds. In Flyvbjerg, F., Julicher, F., Ormos, P. and David, F. (eds.), *Physics of bio-molecules and cells*. Springer-Verlag, pp. 145-185.
- Faham, S., Yang, D., Bare, E., Yohannan, S., Whitelegge, J.P. and Bowie, J.U. (2004) Side-chain contributions to membrane protein structure and stability. *J Mol Biol*, **335**, 297-305.
- Fantner, G.E., Birkedal, H., Kindt, J.H., Hassenkam, T., Weaver, J.C., Cutroni, J.A., Bosma, B.L., Bawazer, L., Finch, M.M., Cidade, G.A., Morse, D.E., Stucky, G.D. and Hansma, P.K. (2004) Influence of the degradation of the organic matrix on the microscopic fracture behavior of trabecular bone. *Bone*, **35**, 1013-1022.
- Florin, E.L., Rief, M., Lehmann, H., Ludwig, M., Dornmair, C., Moy, V.T. and Gaub, H.E. (1995) Sensing Specific Molecular-Interactions with the Atomic-Force Microscope. *Biosensors & Bioelectronics*, **10**, 895-901.
- Franz, C.M. and Muller, D.J. (2005) Analyzing focal adhesion structure by atomic force microscopy. *J Cell Sci*, **118**, 5315-5323.

- Gale, M., Pollanen, M.S., Markiewicz, P. and Goh, M.C. (1995) Sequential assembly of collagen revealed by atomic force microscopy. *Biophys J*, **68**, 2124-2128.
- Gallant, N.D., Michael, K.E. and Garcia, A.J. (2005) Cell adhesion strengthening: contributions of adhesive area, integrin binding, and focal adhesion assembly. *Mol Biol Cell*, **16**, 4329-4340.
- Garcia, R. and Perez, R. (2002) Dynamic atomic force microscopy methods. *Surface Science Reports*, **47**, 197-301.
- Gayatri, R., Sharma, A.K., Rajaram, R. and Ramasami, T. (2001) Chromium(III)-induced structural changes and self-assembly of collagen. *Biochem Biophys Res Commun*, **283**, 229-235.
- Gordeliy, V.I., Labahn, J., Moukhametzianov, R., Efremov, R., Granzin, J., Schlesinger, R., Buldt, G., Savopol, T., Scheidig, A.J., Klare, J.P. and Engelhard, M. (2002) Molecular basis of transmembrane signalling by sensory rhodopsin II-transducer complex. *Nature*, **419**, 484-487.
- Graham, H.K., Holmes, D.F., Watson, R.B. and Kadler, K.E. (2000) Identification of collagen fibril fusion during vertebrate tendon morphogenesis. The process relies on unipolar fibrils and is regulated by collagen-proteoglycan interaction. *J Mol Biol*, **295**, 891-902.
- Grandbois, M., Beyer, M., Rief, M., Clausen-Schaumann, H. and Gaub, H.E. (1999) How strong is a covalent bond? *Science*, **283**, 1727-1730.
- Grinnell, F. (2000) Fibroblast-collagen-matrix contraction: growth-factor signalling and mechanical loading. *Trends Cell Biol*, **10**, 362-365.
- Grinnell, F. (2003) Fibroblast biology in three-dimensional collagen matrices. *Trends Cell Biol*, **13**, 264-269.
- Gutsmann, T., Fantner, G.E., Venturoni, M., Ekani-Nkodo, A., Thompson, J.B., Kindt, J.H., Morse, D.E., Fygenson, D.K. and Hansma, P.K. (2003) Evidence that collagen fibrils in tendons are inhomogeneously structured in a tubelike manner. *Biophys J*, **84**, 2593-2598.
- Gutsmann, T., Hassenkam, T., Cutroni, J.A. and Hansma, P.K. (2005) Sacrificial bonds in polymer brushes from rat tail tendon functioning as nanoscale velcro. *Biophys J*, **89**, 536-542.
- Habelitz, S., Balooch, M., Marshall, S.J., Balooch, G. and Marshall, G.W., Jr. (2002) In situ atomic force microscopy of partially demineralized human dentin collagen fibrils. *J Struct Biol*, **138**, 227-236.
- Haber, E. and Anfinsen, C.B. (1961) Regeneration of enzyme activity by air oxidation of reduced subtilisin-modified ribonuclease. *J Biol Chem*, **236**, 422-424.
- Hansma, H.G., Vesenska, J., Siegerist, C., Kelderman, G., Morrett, H., Sinsheimer, R.L., Elings, V., Bustamante, C. and Hansma, P.K. (1992)

- Reproducible imaging and dissection of plasmid DNA under liquid with the atomic force microscope. *Science*, **256**, 1180-1184.
- Hassenkam, T., Fantner, G.E., Cutroni, J.A., Weaver, J.C., Morse, D.E. and Hansma, P.K. (2004) High-resolution AFM imaging of intact and fractured trabecular bone. *Bone*, **35**, 4-10.
- Hattori, S., Adachi, E., Ebihara, T., Shirai, T., Someki, I. and Irie, S. (1999) Alkali-treated collagen retained the triple helical conformation and the ligand activity for the cell adhesion via $\alpha 2\beta 1$ integrin. *J Biochem (Tokyo)*, **125**, 676-684.
- Havelka, W.A., Henderson, R., Heymann, J.A. and Oesterhelt, D. (1993) Projection structure of halorhodopsin from *Halobacterium halobium* at 6 Å resolution obtained by electron cryo-microscopy. *J Mol Biol*, **234**, 837-846.
- Havelka, W.A., Henderson, R. and Oesterhelt, D. (1995) Three-dimensional structure of halorhodopsin at 7 Å resolution. *J Mol Biol*, **247**, 726-738.
- Hegner, M., Wagner, P. and Semenza, G. (1993) Ultralarge Atomically Flat Template-Stripped Au Surfaces for Scanning Probe Microscopy. *Surface Science*, **291**, 39-46.
- Heise, H., Hoyer, W., Becker, S., Andronesi, O.C., Riedel, D. and Baldus, M. (2005) Molecular-level secondary structure, polymorphism, and dynamics of full-length α -synuclein fibrils studied by solid-state NMR. *Proc Natl Acad Sci U S A*, **102**, 15871-15876.
- Heylighen, F. (2001) Complexity and evolution, by Max Pettersson, The major transitions in evolution, by John Maynard Smith and Eörs Szathmáry, The origins of life from the birth of life to the origin of language, by John Maynard Smith and Eörs Szathmáry. *Complexity*, **6**, 53-57.
- Heymann, J.A., Havelka, W.A. and Oesterhelt, D. (1993) Homologous overexpression of a light-driven anion pump in an archaebacterium. *Mol Microbiol*, **7**, 623-630.
- Heymann, J.B., Moller, C. and Muller, D.J. (2002) Sampling effects influence heights measured with atomic force microscopy. *J Microsc*, **207**, 43-51.
- Hinterdorfer, P. and Dufrene, Y.F. (2006) Detection and localization of single molecular recognition events using atomic force microscopy. *Nat Methods*, **3**, 347-355.
- Ho, S.P., Sulyanto, R.M., Marshall, S.J. and Marshall, G.W. (2005) The cementum-dentin junction also contains glycosaminoglycans and collagen fibrils. *J Struct Biol*, **151**, 69-78.
- Hofmann, H., Voss, T., Kuhn, K. and Engel, J. (1984) Localization of flexible sites in thread-like molecules from electron micrographs. Comparison of interstitial, basement membrane and intima collagens. *J Mol Biol*, **172**, 325-343.

- Hoh, J.H., Sosinsky, G.E., Revel, J.P. and Hansma, P.K. (1993) Structure of the extracellular surface of the gap junction by atomic force microscopy. *Biophys J*, **65**, 149-163.
- Hohenester, E. and Engel, J. (2002) Domain structure and organisation in extracellular matrix proteins. *Matrix Biol*, **21**, 115-128.
- Hohenfeld, I.P., Wegener, A.A. and Engelhard, M. (1999) Purification of histidine tagged bacteriorhodopsin, pharaonis halorhodopsin and pharaonis sensory rhodopsin II functionally expressed in Escherichia coli. *FEBS Lett*, **442**, 198-202.
- Holmes, D.F., Gilpin, C.J., Baldock, C., Ziese, U., Koster, A.J. and Kadler, K.E. (2001) Corneal collagen fibril structure in three dimensions: Structural insights into fibril assembly, mechanical properties, and tissue organization. *Proc Natl Acad Sci U S A*, **98**, 7307-7312.
- Holmes, D.F. and Kadler, K.E. (2005) The precision of lateral size control in the assembly of corneal collagen fibrils. *J Mol Biol*, **345**, 773-784.
- Holt, S.A., Lakey, J.H., Daud, S.M. and Keegan, N. (2005) Neutron reflectometry of membrane protein assemblies at the solid/liquid interface. *Australian Journal of Chemistry*, **58**, 674-677.
- Howard, J. (2001) Polymer mechanics. In *Mechanics of motor proteins and the cytoskeleton*. Sinauer Associates, Sunderland, MA, pp. 99-116.
- Hulmes, D.J. (2002) Building collagen molecules, fibrils, and suprafibrillar structures. *J Struct Biol*, **137**, 2-10.
- Janovjak, H., Kessler, M., Oesterhelt, D., Gaub, H. and Muller, D.J. (2003) Unfolding pathways of native bacteriorhodopsin depend on temperature. *Embo J*, **22**, 5220-5229.
- Janovjak, H., Struckmeier, J., Hubain, M., Kedrov, A., Kessler, M. and Muller, D.J. (2004) Probing the energy landscape of the membrane protein bacteriorhodopsin. *Structure (Camb)*, **12**, 871-879.
- Janshoff, A., Neitzert, M., Oberdorfer, Y. and Fuchs, H. (2000) Force Spectroscopy of Molecular Systems-Single Molecule Spectroscopy of Polymers and Biomolecules. *Angew Chem Int Ed Engl*, **39**, 3212-3237.
- Jiang, F., Horber, H., Howard, J. and Muller, D.J. (2004a) Assembly of collagen into microribbons: effects of pH and electrolytes. *J Struct Biol*, **148**, 268-278.
- Jiang, F., Khairy, K., Poole, K., Howard, J. and Muller, D.J. (2004b) Creating nanoscopic collagen matrices using atomic force microscopy. *Microsc Res Tech*, **64**, 435-440.
- Jurvelin, J.S., Müller, D.J., Wong, M., Studer, D., Engel, A. and Hunziker, E.B. (1996) Surface and sub-surface morphology of bovine humeral articular

cartilage as assessed by atomic force- and transmission electron microscopy. *J. Struct. Biol.*, **117**, 45-54.

Kadler, K.E. (1993) Learning how mutations in type I collagen genes cause connective tissue disease. *Int J Exp Pathol*, **74**, 319-323.

Kadler, K.E., Hojima, Y. and Prockop, D.J. (1987) Assembly of collagen fibrils de novo by cleavage of the type I pC-collagen with procollagen C-proteinase. Assay of critical concentration demonstrates that collagen self-assembly is a classical example of an entropy-driven process. *J Biol Chem*, **262**, 15696-15701.

Kadler, K.E., Holmes, D.F., Graham, H. and Starborg, T. (2000) Tip-mediated fusion involving unipolar collagen fibrils accounts for rapid fibril elongation, the occurrence of fibrillar branched networks in skin and the paucity of collagen fibril ends in vertebrates. *Matrix Biol*, **19**, 359-365.

Kadler, K.E., Holmes, D.F., Trotter, J.A. and Chapman, J.A. (1996) Collagen fibril formation. *Biochem J*, **316 (Pt 1)**, 1-11.

Kahya, N. (2006) Targeting membrane proteins to liquid-ordered phases: molecular self-organization explored by fluorescence correlation spectroscopy. *Chemistry and Physics of Lipids*, **141**, 158-168.

Karrasch, S., Hegerl, R., Hoh, J.H., Baumeister, W. and Engel, A. (1994) Atomic force microscopy produces faithful high-resolution images of protein surfaces in an aqueous environment. *Proc Natl Acad Sci U S A*, **91**, 836-838.

Kedrov, A., Ziegler, C., Janovjak, H., Kuhlbrandt, W. and Muller, D.J. (2004) Controlled unfolding and refolding of a single sodium-proton antiporter using atomic force microscopy. *J Mol Biol*, **340**, 1143-1152.

Kessler, M. and Gaub, H.E. (2006) Unfolding barriers in bacteriorhodopsin probed from the cytoplasmic and the extracellular side by AFM. *Structure*, **14**, 521-527.

Kessler, M., Gottschalk, K.E., Janovjak, H., Muller, D.J. and Gaub, H.E. (2006) Bacteriorhodopsin folds into the membrane against an external force. *J Mol Biol*, **357**, 644-654.

Kobayashi, K., Ito, T. and Hoshino, T. (1985) Electron microscopic demonstration of acid-labile, 4D-staggered intermolecular association of collagen formed in vitro. *Coll Relat Res*, **5**, 253-260.

Kobayashi, Y. and Saigo, K. (2005) Periodic ab initio approach for the cooperative effect of CH/pi interaction in crystals: relative energy of CH/pi and hydrogen-bonding interactions. *J Am Chem Soc*, **127**, 15054-15060.

Koebnik, R., Locher, K.P. and Van Gelder, P. (2000) Structure and function of bacterial outer membrane proteins: barrels in a nutshell. *Mol Microbiol*, **37**, 239-253.

- Kolbe, M., Besir, H., Essen, L.O. and Oesterhelt, D. (2000) Structure of the light-driven chloride pump halorhodopsin at 1.8 Å resolution. *Science*, **288**, 1390-1396.
- Kunicki, T.J. (2002) The influence of platelet collagen receptor polymorphisms in hemostasis and thrombotic disease. *Arterioscler Thromb Vasc Biol*, **22**, 14-20.
- Kunji, E.R., von Gronau, S., Oesterhelt, D. and Henderson, R. (2000) The three-dimensional structure of halorhodopsin to 5 Å by electron crystallography: A new unbending procedure for two-dimensional crystals by using a global reference structure. *Proc Natl Acad Sci U S A*, **97**, 4637-4642.
- Kurakin, A. (2005) Self-organization versus Watchmaker: stochastic dynamics of cellular organization. *Biol Chem*, **386**, 247-254.
- Landau, E.M., Pebay-Peyroula, E. and Neutze, R. (2003) Structural and mechanistic insight from high resolution structures of archaeal rhodopsins. *FEBS Lett*, **555**, 51-56.
- Lang, H. (2000) Outer membrane proteins as surface display systems. *International Journal of Medical Microbiology*, **290**, 579-585.
- Lang, H., Duschl, C. and Vogel, H. (1994) A new class of thiolipids for the attachment of lipid bilayers on gold surfaces. *Langmuir*, **10**, 197-210.
- Lee, K.B., Park, S.J., Mirkin, C.A., Smith, J.C. and Mrksich, M. (2002) Protein nanoarrays generated by dip-pen nanolithography. *Science*, **295**, 1702-1705.
- Leggett, G.J. (2003) Friction force microscopy of self-assembled monolayers: probing molecular organisation at the nanometre scale. *Analytica Chimica Acta*, **479**, 17-38.
- Leonhard, K., Guiard, B., Pellecchia, G., Tzagoloff, A., Neupert, W. and Langer, T. (2000) Membrane protein degradation by AAA proteases in mitochondria: extraction of substrates from either membrane surface. *Mol Cell*, **5**, 629-638.
- Love, J.C., Estroff, L.A., Kriebel, J.K., Nuzzo, R.G. and Whitesides, G.M. (2005) Self-assembled monolayers of thiolates on metals as a form of nanotechnology. *Chemical Reviews*, **105**, 1103-1169.
- Luecke, H., Schobert, B., Lanyi, J.K., Spudich, E.N. and Spudich, J.L. (2001) Crystal structure of sensory rhodopsin II at 2.4 angstroms: insights into color tuning and transducer interaction. *Science*, **293**, 1499-1503.
- Marshall, G.W., Yucel, N., Balooch, M., Kinney, J.H., Habelitz, S. and Marshall, S.J. (2001) Sodium hypochlorite alterations of dentin and dentin collagen. *Surf. Sci.*, **491**, 444-455.

- McBride, D.J., Jr., Kadler, K.E., Hojima, Y. and Prockop, D.J. (1992) Self-assembly into fibrils of a homotrimer of type I collagen. *Matrix*, **12**, 256-263.
- Meek, K.M., Chapman, J.A. and Hardcastle, R.A. (1979) The staining pattern of collagen fibrils. Improved correlation with sequence data. *J Biol Chem*, **254**, 10710-10714.
- Meller, D., Peters, K. and Meller, K. (1997) Human cornea and sclera studied by atomic force microscopy. *Cell and Tissue Research*, **288**, 111-118.
- Meyer, E., Hug, H.J. and Bennewitz, R. (2004) *Scanning probe microscopy. The lab on a tip*. Springer-verlag.
- Milhiet, P.E., Gubellini, F., Berquand, A., Dosset, P., Rigaud, J.L., Le Grimmelc, C. and Levy, D. (2006) High-resolution AFM of membrane proteins directly incorporated at high density in planar lipid bilayer. *Biophys J*, **91**, 3268-3275.
- Moller, C., Allen, M., Elings, V., Engel, A. and Muller, D.J. (1999) Tapping-mode atomic force microscopy produces faithful high-resolution images of protein surfaces. *Biophys J*, **77**, 1150-1158.
- Muller, D.J., Amrein, M. and Engel, A. (1997) Adsorption of biological molecules to a solid support for scanning probe microscopy. *J Struct Biol*, **119**, 172-188.
- Muller, D.J. and Engel, A. (1997) The height of biomolecules measured with the atomic force microscope depends on electrostatic interactions. *Biophys J*, **73**, 1633-1644.
- Müller, D.J. and Engel, A. (1999) Voltage and pH-induced channel closure of porin OmpF visualized by atomic force microscopy. *J. Mol. Biol.*, **285**, 1347-1351.
- Muller, D.J., Fotiadis, D., Scheuring, S., Muller, S.A. and Engel, A. (1999a) Electrostatically balanced subnanometer imaging of biological specimens by atomic force microscope. *Biophys J*, **76**, 1101-1111.
- Muller, D.J., Hand, G.M., Engel, A. and Sosinsky, G.E. (2002a) Conformational changes in surface structures of isolated connexin 26 gap junctions. *Embo J*, **21**, 3598-3607.
- Muller, D.J., Janovjak, H., Lehto, T., Kuerschner, L. and Anderson, K. (2002b) Observing structure, function and assembly of single proteins by AFM. *Prog Biophys Mol Biol*, **79**, 1-43.
- Müller, D.J., Janovjak, H., Lehto, T., Kuerschner, L. and Anderson, K. (2002) Observing structure, function and assembly of single proteins by AFM. *Prog. Biophys. Mol. Biol.*, **79**, 1-43.

- Muller, D.J., Kessler, M., Oesterhelt, F., Moller, C., Oesterhelt, D. and Gaub, H. (2002c) Stability of bacteriorhodopsin alpha-helices and loops analyzed by single-molecule force spectroscopy. *Biophys J*, **83**, 3578-3588.
- Muller, D.J., Sass, H.J., Muller, S.A., Buldt, G. and Engel, A. (1999b) Surface structures of native bacteriorhodopsin depend on the molecular packing arrangement in the membrane. *J Mol Biol*, **285**, 1903-1909.
- Myllyharju, J. and Kivirikko, K.I. (2001) Collagens and collagen-related diseases. *Ann Med*, **33**, 7-21.
- Myllyharju, J. and Kivirikko, K.I. (2004) Collagens, modifying enzymes and their mutations in humans, flies and worms. *Trends Genet*, **20**, 33-43.
- Naumann, R., Schiller, S.M., Giess, F., Grohe, B., Hartman, K.B., Karcher, I., Koper, I., Lubben, J., Vasilev, K. and Knoll, W. (2003) Tethered lipid Bilayers on ultraflat gold surfaces. *Langmuir*, **19**, 5435-5443.
- Norman, J.J. and Desai, T.A. (2006) Methods for fabrication of nanoscale topography for tissue engineering scaffolds. *Ann Biomed Eng*, **34**, 89-101.
- Oberhauser, A.F., Hansma, P.K., Carrion-Vazquez, M. and Fernandez, J.M. (2001) Stepwise unfolding of titin under force-clamp atomic force microscopy. *Proc Natl Acad Sci U S A*, **98**, 468-472.
- Oberhauser, A.F., Marszalek, P.E., Carrion-Vazquez, M. and Fernandez, J.M. (1999) Single protein misfolding events captured by atomic force microscopy. *Nat Struct Biol*, **6**, 1025-1028.
- Oesterhelt, F., Oesterhelt, D., Pfeiffer, M., Engel, A., Gaub, H.E. and Muller, D.J. (2000) Unfolding pathways of individual bacteriorhodopsins. *Science*, **288**, 143-146.
- Ohnesorge, F. and Binnig, G. (1993) True atomic resolution by atomic force microscopy through repulsive and attractive forces. *Science*, **262**, 1451 - 1456.
- Orgel, J.P., Irving, T.C., Miller, A. and Wess, T.J. (2006) Microfibrillar structure of type I collagen in situ. *Proc Natl Acad Sci U S A*, **103**, 9001-9005.
- Orgel, J.P., Miller, A., Irving, T.C., Fischetti, R.F., Hammersley, A.P. and Wess, T.J. (2001) The in situ supermolecular structure of type I collagen. *Structure (Camb)*, **9**, 1061-1069.
- Ortiz-Urda, S., Garcia, J., Green, C.L., Chen, L., Lin, Q., Veitch, D.P., Sakai, L.Y., Lee, H., Marinkovich, M.P. and Khavari, P.A. (2005) Type VII collagen is required for Ras-driven human epidermal tumorigenesis. *Science*, **307**, 1773-1776.
- Paige, M.F. and Goh, M.C. (2001) Ultrastructure and assembly of segmental long spacing collagen studied by atomic force microscopy. *Micron*, **32**, 355-361.

- Paterlini, M.G., Nemethy, G. and Scheraga, H.A. (1995) The energy of formation of internal loops in triple-helical collagen polypeptides. *Biopolymers*, **35**, 607-619.
- Persike, N., Pfeiffer, M., Guckenberger, R., Radmacher, M. and Fritz, M. (2001) Direct observation of different surface structures on high-resolution images of native halorhodopsin. *J Mol Biol*, **310**, 773-780.
- Petruska, J.A. and Hodge, A.J. (1964) A Subunit Model for the Tropocollagen Macromolecule. *Proc Natl Acad Sci U S A*, **51**, 871-876.
- Philippson, A., Im, W., Engel, A., Schirmer, T., Roux, B. and Muller, D.J. (2002) Imaging the electrostatic potential of transmembrane channels: atomic probe microscopy of OmpF porin. *Biophys J*, **82**, 1667-1676.
- Poole, K., Khairy, K., Friedrichs, J., Franz, C., Cisneros, D.A., Howard, J. and Mueller, D. (2005) Molecular-scale Topographic Cues Induce the Orientation and Directional Movement of Fibroblasts on Two-dimensional Collagen Surfaces. *J Mol Biol*, **349**, 380-386.
- Poole, K., Meder, D., Simons, K. and Muller, D. (2004) The effect of raft lipid depletion on microvilli formation in MDCK cells, visualized by atomic force microscopy. *FEBS Lett*, **565**, 53-58.
- Poole, K. and Muller, D. (2005) Flexible, actin-based ridges colocalise with the beta1 integrin on the surface of melanoma cells. *Br J Cancer*, **92**, 1499-1505.
- Popot, J.L., Berry, E.A., Charvolin, D., Creuzenet, C., Ebel, C., Engelman, D.M., Flotenmeyer, M., Giusti, F., Gohon, Y., Herve, P., Hong, Q., Lakey, J.H., Leonard, K., Shuman, H.A., Timmins, P., Warschawski, D.E., Zito, F., Zoonens, M., Pucci, B. and Tribet, C. (2003) Amphipols: polymeric surfactants for membrane biology research. *Cellular and Molecular Life Sciences*, **60**, 1559-1574.
- Popot, J.L. and Engelman, D.M. (1990) Membrane protein folding and oligomerization: the two-stage model. *Biochemistry*, **29**, 4031-4037.
- Prockop, D.J. (1998) What holds us together? Why do some of us fall apart? What can we do about it? *Matrix Biol*, **16**, 519-528.
- Prockop, D.J. (1999) Hopkins Memorial Medal lecture. Pleasant surprises en route from the biochemistry of collagen to attempts at gene therapy. *Biochem Soc Trans*, **27**, 15-31.
- Prockop, D.J. and Fertala, A. (1998) The collagen fibril: the almost crystalline structure. *J Struct Biol*, **122**, 111-118.
- Rajendran, L. and Simons, K. (2005) Lipid rafts and membrane dynamics. *J Cell Sci*, **118**, 1099-1102.

- Raspanti, M., Alessandrini, A., Ottani, V. and Ruggeri, A. (1997) Direct visualization of collagen-bound proteoglycans by tapping-mode atomic force microscopy. *J Struct Biol*, **119**, 118-122.
- Raspanti, M., Binaghi, E., Gallo, I. and Manelli, A. (2005) A vision-based, 3D reconstruction technique for scanning electron microscopy: direct comparison with atomic force microscopy. *Microsc Res Tech*, **67**, 1-7.
- Raspanti, M., Congiu, T. and Guizzardi, S. (2001) Tapping-mode atomic force microscopy in fluid of hydrated extracellular matrix. *Matrix Biol.*, **20**, 601-604.
- Raspanti, M., Congiu, T. and Guizzardi, S. (2002) Structural aspects of the extracellular matrix of the tendon: an atomic force and scanning electron microscopy study. *Arch Histol Cytol*, **65**, 37-43.
- Raspanti, M., Ottani, V. and Ruggeri, A. (1989) Different architectures of the collagen fibril: morphological aspects and functional implications. *Int J Biol Macromol*, **11**, 367-371.
- Revenko, I., Sommer, F., Minh, D.T., Garrone, R. and Franc, J.M. (1994) Atomic force microscopy study of the collagen fibre structure. *Biol Cell*, **80**, 67-69.
- Rief, M., Fernandez, J.M. and Gaub, H.E. (1998) Elastically coupled two-level systems as a model for biopolymer extensibility. *Physical Review Letters*, **81**, 4764-4767.
- Rief, M., Gautel, M., Oesterhelt, F., Fernandez, J.M. and Gaub, H.E. (1997) Reversible unfolding of individual titin immunoglobulin domains by AFM. *Science*, **276**, 1109-1112.
- Rose, G.D., Fleming, P.J., Banavar, J.R. and Maritan, A. (2006) A backbone-based theory of protein folding. *Proc Natl Acad Sci U S A*, **103**, 16623-16633.
- Schabert, F.A., Henn, C. and Engel, A. (1995) Native Escherichia coli OmpF porin surfaces probed by atomic force microscopy. *Science*, **268**, 92-94.
- Scheuring, S., Müller, D.J., Stahlberg, H., Engel, H.A. and Engel, A. (2002) Sampling the conformational space of membrane protein surfaces with the AFM. *Eur. Biophys. J.*, **31**, 172-178.
- Schwarz, U.D., Haefke, H., Reimann, P. and Guntherodt, H.J. (1994) Tip artefacts in scanning force microscopy. *J. Microsc.*, **173**, 183-197.
- Sharma, A.K., Spudich, J.L. and Doolittle, W.F. (2006) Microbial rhodopsins: functional versatility and genetic mobility. *Trends Microbiol*, **14**, 463-469.
- Shin, S.K., Yoon, H.J., Jung, Y.J. and Park, J.W. (2006) Nanoscale controlled self-assembled monolayers and quantum dots. *Curr Opin Chem Biol*, **10**, 423-429.

- Sigal, G.B., Mrksich, M. and Whitesides, G.M. (1997) Using surface plasmon resonance spectroscopy to measure the association of detergents with self-assembled monolayers of hexadecanethiolate on gold. *Langmuir*, **13**, 2749-2755.
- Silver, F.H., Ebrahimi, A. and Snowhill, P.B. (2002) Viscoelastic properties of self-assembled type I collagen fibers: molecular basis of elastic and viscous behaviors. *Connect Tissue Res*, **43**, 569-580.
- Silver, F.H., Freeman, J.W. and Seehra, G.P. (2003) Collagen self-assembly and the development of tendon mechanical properties. *J Biomech*, **36**, 1529-1553.
- Silver, F.H., Langley, K.H. and Trelstad, R.L. (1979) Type I collagen fibrillogenesis: initiation via reversible linear and lateral growth steps. *Biopolymers*, **18**, 2523-2535.
- Spudich, J.L. (2006) The multitasking microbial sensory rhodopsins. *Trends Microbiol*, **14**, 480-487.
- Stora, T., Lakey, J.H. and Vogel, H. (1999) Ion-channel gating in transmembrane receptor proteins: Functional activity in tethered lipid membranes. *Angew. Chem. Int. Ed.*, **38**, 389-392.
- Stroh, C.M., Ebner, A., Geretschlager, M., Freudenthaler, G., Kienberger, F., Kamruzzahan, A.S., Smith-Gill, S.J., Gruber, H.J. and Hinterdorfer, P. (2004) Simultaneous topography and recognition imaging using force microscopy. *Biophys J*, **87**, 1981-1990.
- Subramaniam, S. and Henderson, R. (2000) Molecular mechanism of vectorial proton translocation by bacteriorhodopsin. *Nature*, **406**, 653-657.
- Subramaniam, S. and Sampath, S. (2005) Effect of chain length on the adhesion behaviour of n-alkanethiol self-assembled monolayers on Au(111): An atomic force microscopy study. *Pramana-Journal of Physics*, **65**, 753-761.
- Sun, H.B., Smith, G.N., Hasty, K.A. and Yokota, H. (2000) Atomic force microscopy-based detection of binding and cleavage site of matrix metalloproteinase on individual type II collagen helices. *Analytical Biochemistry*, **283**, 153-158.
- Tamada, K., Hara, M., Sasabe, H. and Knoll, W. (1997) Surface phase behavior of n-alkanethiol self-assembled monolayers adsorbed on Au(111): An atomic force microscope study. *Langmuir*, **13**, 1558-1566.
- Terrettaz, S., Stora, T., Duschl, C. and Vogel, H. (1993) Protein binding to supported lipid membranes; Investigation of the Cholera Toxin-Ganglioside interaction by simultaneous impedance spectroscopy and surface plasmon resonance. *Langmuir*, **9**, 1361-1369.

- Terrettaz, S., Ulrich, W.-P., Vogel, H., Hong, Q., Dover, L.G. and Lakey, J.H. (2002) Stable self-assembly of a protein engineering scaffold on gold surfaces. *Protein Science*, **11**, 1917-1925.
- Thalhammer, S., Heckl, W.M., Zink, A. and Nerlich, A.G. (2001) Atomic force microscopy for high resolution imaging of collagen fibrils - A new technique to investigate collagen structure in historic bone tissues. *J. Arch. Sci.*, **28**, 1061-1068.
- Thomas, R.K. (2004) Neutron reflection from liquid interfaces. *Annual Review of Physical Chemistry*, **55**, 391-426.
- Tinazli, A., Tang, J., Valiokas, R., Picuric, S., Lata, S., Piehler, J., Liedberg, B. and Tampe, R. (2005) High-affinity chelator thiols for switchable and oriented immobilization of histidine-tagged proteins: a generic platform for protein chip technologies. *Chemistry*, **11**, 5249-5259.
- Vogel, V., Thomas, W.E., Craig, D.W., Krammer, A. and Baneyx, G. (2001) Structural insights into the mechanical regulation of molecular recognition sites. *Trends Biotechnol*, **19**, 416-423.
- Wagner, P., Hegner, M., Guntherodt, H.J. and Semenza, G. (1995) Formation and in-Situ Modification of Monolayers Chemisorbed on Ultraflat Template-Stripped Gold Surfaces. *Langmuir*, **11**, 3867-3875.
- Wagner, P., Kernén, P., Hegner, M., Ungewickell, E. and Semenza, G. (1994) Covalent Anchoring of Proteins onto Gold-Directed Nhs-Terminated Self-Assembled Monolayers in Aqueous Buffers - Sfm Images of Clathrin Cages and Triskelia. *Febs Letters*, **356**, 267-271.
- Wagner, P., Zaugg, F., Kernén, P., Hegner, M. and Semenza, G. (1996) omega-Functionalized self-assembled monolayers chemisorbed on ultraflat Au(111) surfaces for biological scanning probe microscopy in aqueous buffers. *Journal of Vacuum Science & Technology B*, **14**, 1466-1471.
- Ward, N.P., Hulmes, D.J. and Chapman, J.A. (1986) Collagen self-assembly in vitro: electron microscopy of initial aggregates formed during the lag phase. *J Mol Biol*, **190**, 107-112.
- Wess, T.J. (2005) Collagen fibril form and function. *Adv Protein Chem*, **70**, 341-374.
- Wess, T.J., Hammersley, A.P., Wess, L. and Miller, A. (1998) Molecular packing of type I collagen in tendon. *J Mol Biol*, **275**, 255-267.
- White, S.H. (2003) Translocons, thermodynamics, and the folding of membrane proteins. *FEBS Lett*, **555**, 116-121.
- White, S.H. (2004) The progress of membrane protein structure determination. *Protein Sci*, **13**, 1948-1949.

- White, S.H. and von Heijne, G. (2004) The machinery of membrane protein assembly. *Curr Opin Struct Biol*, **14**, 397-404.
- White, S.H. and von Heijne, G. (2005) Transmembrane helices before, during, and after insertion. *Curr Opin Struct Biol*, **15**, 378-386.
- Whitesides, G.M. and Boncheva, M. (2002) Beyond molecules: self-assembly of mesoscopic and macroscopic components. *Proc Natl Acad Sci U S A*, **99**, 4769-4774.
- Woolhead, C.A., McCormick, P.J. and Johnson, A.E. (2004) Nascent membrane and secretory proteins differ in FRET-detected folding far inside the ribosome and in their exposure to ribosomal proteins. *Cell*, **116**, 725-736.
- Yang, G., Amro, N.A., Starkewolfe, Z.B. and Liu, G.Y. (2004) Molecular-level approach to inhibit degradations of alkanethiol self-assembled monolayers in aqueous media. *Langmuir*, **20**, 3995-4003.
- Yang, W., Lu, Y., Kalajzic, I., Guo, D., Harris, M.A., Gluhak-Heinrich, J., Kotha, S., Bonewald, L.F., Feng, J.Q., Rowe, D.W., Turner, C.H., Robling, A.G. and Harris, S.E. (2005) Dentin matrix protein 1 gene cis-regulation: use in osteocytes to characterize local responses to mechanical loading in vitro and in vivo. *J Biol Chem*, **280**, 20680-20690.
- Ye, Y., Meyer, H.H. and Rapoport, T.A. (2001) The AAA ATPase Cdc48/p97 and its partners transport proteins from the ER into the cytosol. *Nature*, **414**, 652-656.
- Yon, J.M. (2002) Protein folding in the post-genomic era. *J Cell Mol Med*, **6**, 307-327.
- Yu, J., Bippes, C.A., Hand, G.M., Muller, D.J. and Sosinsky, G.E. (2007) Aminosulfonate modulated pH induced conformational changes in connexin26 hemichannels. *J Biol Chem*.
- Yuspa, S.H. and Epstein, E.H., Jr. (2005) Cancer. An anchor for tumor cell invasion. *Science*, **307**, 1727-1728.
- Zhong, Q., Inniss, D., Kjoller, K. and Elings, V.B. (1993) Fractured Polymer Silica Fiber Surface Studied by Tapping Mode Atomic-Force Microscopy. *Surface Science*, **290**, L688-L692.
- Zhuang, X. and Rief, M. (2003) Single-molecule folding. *Curr Opin Struct Biol*, **13**, 88-97.

Erklärung und Versicherung

Erklärung

Diese Dissertation wurde am Max-Planck-Institut fuer molekulare Zellbiologie und Genetik, Dresden und Biotechnologisches Zentrum der TU-Dresden unter der wissenschaftlichen Betreuung von Prof. Dr. Daniel J. Müller angefertigt.

Versicherung

Hiermit versichere ich, dass die vorliegende Arbeit ohne unzulässige Hilfe Dritter und ohne Benutzung anderer als der angegebenen Hilfsmittel angefertigt habe. Die aus fremden Quellen direkt oder indirekt übernommenen Gedanken sind als solche gekennzeichnet. Die Arbeit wurde weder im Inland noch im Ausland in gleicher oder ähnlicher Form einer anderen Prüfungsbehörde vorgelegt.

Dresden, den 27.02.2007

David Alejandro Cisneros Armas